# Flow Control through Surface Suction for Small Wind Turbines

A thesis submitted in partial fulfillment of
the requirements for the degree of

**Doctor of Philosophy**

of the
Indian Institute of Technology Bombay, India
and
Monash University, Australia
by

**Jasvipul S Chawla**

Supervisors:
**Prof. Shashikanth Suryanarayanan (IIT Bombay)**
and
**Prof. John Sheridan (Monash University)**

*The course of study for this award was developed jointly by the Indian Institute of Technology Bombay, India and Monash University, Australia and given academic recognition by each of them. The programme was administered by The IITB-Monash Research Academy.*

**2016**

To SARVNIPUN S CHAWLA

# Approval Sheet

The thesis entitled "*Flow Control through Surface Suction for Small Wind Turbines*" by *Jasvipul S Chawla* is approved for the degree of **Doctor of Philosophy**.

---

(Dr. Sanjay Bharadwaj)

**External Examiner**

---

(Prof. Bhalchandra Puranik)

**Internal Examiner**

---

(Prof. Shashikanth Suryanarayanan)

**IITB Supervisor**

---

(Prof. John Sheridan)

**Monash Supervisor**

---

(Prof. Urjit Yajnik)

**Chairman**

**Date:** 27 October 2016

**Place:** Powai

# Declaration

I declare that this written submission represents my ideas in my own words and where others' ideas or words have been included, I have adequately cited and referenced the original sources. I also declare that I have adhered to all principles of academic honesty and integrity and have not misrepresented or fabricated or falsified any idea/data/fact/source in my submission. I understand that any violation of the above will be cause for disciplinary action by the Institute and can also evoke penal action from the sources which have thus not been properly cited or from whom proper permission has not been taken when needed.

## Notice 1

Under the Copyright Act 1968, this thesis must be used only under the normal conditions of scholarly fair dealing. In particular no results or conclusions should be extracted from it, nor should it be copied or closely paraphrased in whole or in part without the written consent of the author. Proper written acknowledgement should be made for any assistance obtained from this thesis.

## Notice 2

I certify that I have made all reasonable efforts to secure copyright permissions for third-party content included in this thesis and have not knowingly added copyright content to my work without the owners permission.

**Jasvipul Singh Chawla**
IITB ID: 09410402
Monash ID: 22362616

# Abstract

This thesis seeks to arrive at estimates of improvement in blade aerodynamic efficiency and reduction in structural loads in small wind turbines through surface suction-based active flow control at low Reynolds numbers ($Re$). Improved aerodynamic efficiency and reduced fatigue loads help achieve lower Cost-of-Energy.

Small wind turbines typically operate off-grid, providing power at the point of consumption. Consequently, such turbines often operate in locations with poor wind speed regimes. Low wind speeds coupled with small chord length of the blades result in low operating $Re$ that often lie between $10^4$ - $10^5$. It is well-known that such operating $Re$ imposes significant challenges in realising good aerodynamic efficiency due to the propensity for flow separation to occur.

It has been established that flow separation can be avoided or delayed using active flow control. However, much of such work on active flow control has focused on high $Re$ applications. This thesis focuses on the application of surface suction, a popular active flow control methodology, in low $Re$ regimes seen in small wind turbines.

The approach adopted towards arriving at the aforementioned estimates of improvement in blade aerodynamic efficiency and reduction in structural loads in small wind turbines is as follows:

1. Experimental characterisation of the improvement in the aerodynamic characteristics of two aerofoil profiles, NACA0012 and S814, commonly used in small wind turbine applications, in low $Re$ regimes is performed. Specifically, this characterisation captures both the steady-state characteristics as well as identification of the temporal dynamics between change in the coefficient of lift ($\Delta C_L$) and change in the coefficient of drag ($\Delta C_D$) with the non-dimensional parameter, $C_\mu$ (defined as the ratio of the momentum of air drawn through suction and the momentum of the air flowing over the aerofoil, that is, $\rho\, A_{slit}\, u_s^2 / \rho\, A_{aerofoil}\, U_\infty^2$, where $\rho$ is air density,

$A_{slit}$ area of the slit, $A_{aerofoil}$ area of the aerofoil, $u_s$ suction velocity and $U_\infty$ the free stream velocity):

(a) $\Delta C_L$, $\Delta C_D = f(C_\mu)$

(b) $\Delta C_L$, $\Delta C_D = f(C_\mu, t)$

2. Posing a similitude argument that as long as the dimensionless parameters $C_\mu$ and $Re$ remain comparable to the regimes for which the aforesaid experimental characterisation was done, the steady-state and temporal relationships between $\Delta C_L$, $\Delta C_D$ and $C_\mu$ established could be directly used in numerical simulations for predicting the behaviour of small wind turbines.

3. Using the relation $\Delta C_L$, $\Delta C_D = f(C_\mu)$ and steady Blade Element Momentum (BEM) theory to estimate increase in Coefficient of Power, $C_P$ of a small wind turbine employing surface suction on its blades working in the same $C_\mu, Re$ regime.

4. Incorporating the dynamic map, $\Delta C_L$, $\Delta C_D = f(C_\mu, t)$ into the dynamics of the aero-elastic simulator, FAST to formulate extended turbine dynamics.

5. Utilising, appropriately, $C_\mu$ as an additional control input towards reducing fore-aft oscillations of the tower top while compensating for the said extended turbine dynamics.

6. Demonstrating, through rain-flow analysis, that the reduced oscillations result in mitigation of fatigue loads on the turbine tower structure.

The thesis documents that the approach indicated for increasing $C_P$, when applied to a small wind turbine in sub $1kW$ power output range, with $2m$ radius, NACA0012-blades, operating in steady wind speed of $7.5\,m/s$, increased the expected power output from $764W$ to $1511W$ by expending $106W$ of suction power.

Further, compensating for the extended dynamics of the turbine in the aero-elastic simulator, tower-top oscillations reduced for a $\sim 10kW$ turbine of $2.9m$ radius, S814 blades, hub height $24m$. Thus, for the turbine operating over 20 years in turbulent IEC III-A wind conditions, the structural damage equivalent reduced from $\sim 10$ to $< 1$.

# Contents

**Abstract** i

**List of Tables** vii

**List of Figures** viii

**Nomenclature** xi

**Acronyms** xii

**1 Introduction** 1

1.1 Background . . . . . 1

1.2 Problem definition . . . . . 2

1.2.1 Prior work . . . . . 2

1.2.2 Approach towards the solution . . . . . 3

1.3 Whom will this research benefit . . . . . 5

1.4 Organisation of the report . . . . . 5

**2 Preliminaries and prior work** 6

2.1 Wind turbines, power capture . . . . . 7

2.2 Blade aerodynamics . . . . . 9

2.2.1 Blade Element Momentum (BEM theory) . . . . . 10

2.3 Wind turbine control strategies . . . . . 13

2.3.1 Torque control (control action below rated speed) . . . . . 14

2.3.2 Pitch control (control action above rated speed) . . . . . 15

2.3.3 Control action over full range of wind speeds: . . . . . 16

2.4 Small versus large wind turbines . . . . . 17

2.4.1 Low Reynolds number flows . . . 18
2.4.2 Boundary layer and its separation at low $Re$ . . . 19
2.5 Suction-based flow-control for boundary layer separation . . . 20
2.6 System theoretic view . . . 22
2.6.1 Linear Time Invariant (LTI) system . . . 22
2.6.2 Transient and steady state response . . . 23
2.6.3 Transfer function . . . 24
2.6.4 Closed-loop control system . . . 25
2.7 System identification . . . 26
2.7.1 AutoRegressive eXogenous model (ARX) . . . 26
2.7.2 Piecewise linearization of a parameter varying model . . . 27
2.7.3 Validation . . . 28
2.8 Aerodynamic tests in a wind tunnel . . . 28
2.8.1 Similitude and dimensionless analysis . . . 29
2.9 Wind turbine simulators . . . 30
2.10 Turbine classification based on wind conditions . . . 31
2.11 Fatigue life and rain-flow count of stresses . . . 32
2.12 Prior work . . . 34
2.12.1 Low Reynolds number experiments . . . 34
2.12.2 Flow control at high and low Reynolds numbers . . . 35
2.12.3 Utilisation of flow control in wind turbines . . . 37

**3 Low Reynolds number experiments** **39**
3.1 Introduction . . . 39
3.2 Experimental set-up . . . 40
3.2.1 Reynolds number regime . . . 40
3.2.2 Aerofoils . . . 41
3.2.3 End-plates for two-dimensionality of flow . . . 44
3.2.4 Suction pumps . . . 45
3.2.5 Instrumentation . . . 47
3.2.6 Wind tunnel . . . 50
3.2.7 Data processing . . . 52

3.3 Steady state tests . . . 54
3.3.1 Visulalisations . . . 55
3.3.2 Preliminary tests at IITB 220kW tunnel . . . 57
3.3.3 Final tests at Monash 450kW wind tunnel tests . . . 63
3.3.4 Coefficient of pressure . . . 64
3.3.5 Coefficient of lift . . . 69
3.3.6 Coefficient of drag . . . 71
3.3.7 Effect of varying suction . . . 73
3.3.8 Validation of the experimental set-up . . . 75
3.4 Dynamic tests . . . 77
3.4.1 Choice of variables . . . 78
3.4.2 Tests conducted . . . 80
3.4.3 System identification . . . 83
3.4.4 Validation of the models and prediction of output . . . 86
3.5 Summary . . . 88

**4 Application of surface suction to small wind turbines 90**
4.1 Using wind tunnel results for simulation in wind turbine simulations . . . 90
4.2 BEM simulations for power capture . . . 92
4.2.1 Turbine characteristics . . . 92
4.2.2 BEM Simulations . . . 92
4.2.3 Aerodynamic power output . . . 93
4.2.4 Power input for flow control . . . 94
4.3 Aero-elastic simulations for load mitigation . . . 95
4.3.1 Description of the control problem . . . 97
4.3.2 Simulations . . . 98
4.3.3 Case I - baseline . . . 99
4.3.4 Case II - collective pitch control . . . 100
4.3.5 Case III - flow control through surface suction . . . 101
4.4 Aero-elastic simulation results . . . 102
4.4.1 Response to wind gust . . . 103
4.4.2 Long term response to turbulent winds . . . 106

4.5 Summary . . . . . 113

**5 Conclusions and future work** **114**

5.1 Summary . . . . . 114

5.2 Conclusions . . . . . 115

5.3 Future Work . . . . . 116

**A Cost of Energy** **118**

**B Stress cycles** **119**

**C Publications** **130**

# List of Tables


2.1 Turbine classification based on wind conditions . . . . . 32

3.1 Reynolds numbers for the experiments . . . . . 40
3.2 Pressure tap positions on aerofoil surfaces . . . . . 44
3.3 Steady-state tests conducted for surface pressure . . . . . 54
3.4 Static Tests Conducted for Wake Pressures . . . . . 55
3.5 Comparison of suction effects on NACA0012 aerofoil . . . . . 60
3.6 Comparison of suction effects on S814 aerofoil . . . . . 62
3.7 Tests for Identification . . . . . 82
3.8 Identified Parameters . . . . . 85

4.1 Small wind turbine parameters for BEM based power capture study . . . . 92
4.2 Small wind turbine parameters for aeroelastic simulations . . . . . 99
4.3 Control cases . . . . . 102
4.4 Load mitigation calculations . . . . . 106
4.5 Predicted Hourly Stresses . . . . . 112

A.1 Cost of energy estimates . . . . . 118

# List of Figures


2.1 Large, three bladed, upwind Horizontal Axis Wind Turbine (HAWT) . . . 7
2.2 $C_P$ vs $\lambda$ for a typical three bladed turbine [BSJB01] . . . 8
2.3 Wind turbine control regions . . . 8
2.4 Aerofoil characteristics . . . 9
2.5 Blade element and annular ring [BSJB01] . . . 11
2.6 Resultant forces and velocities for blade elements [BSJB01] . . . 12
2.7 Turbine power as a function of the rotor speed for varying wind speed [AYTS12] . . . 14
2.8 $C_P$ and $\lambda$ vs $\beta$ . . . 15
2.9 Control schematic for variable speed operation [Bos00] . . . 16
2.10 Low $Re$ effects . . . 18
2.11 Boundary layer properties [Sch00] . . . 20
2.12 Control of boundary layer separation by employing surface-suction . . . 20
2.13 Velocity distribution and boundary layer for surface suction starting a finite distance downstream of leading edge of plate . . . 21
2.14 A plant with output $y$, input $u$, measured disturbance $w$, and unmeasured disturbance $v$ . . . 23
2.15 Transient and steady state response to a step input . . . 24
2.16 Response of a dynamic system to single frequency input . . . 25
2.17 An example of a Bode plot . . . 25
2.18 Closed loop control system . . . 26
2.19 System identification of a dynamic system . . . 26
2.20 Schematic of model validation . . . 28
2.21 Representation of wind distribution . . . 31

2.22 Constant amplitude S-N curve for a metal [Col93] . . . 33
2.23 Schematic of rain-flow counting [WPO95] . . . 33

3.1 Aerofoil profiles showing suction through the slits . . . 41
3.2 Aerofoil profiles showing dimensions and positions of suction slits and pressure taps . . . 42
3.3 Aerofoil test set-up inside wind tunnel . . . 45
3.4 Schematic of the test set-up inside Monash $450kW$ tunnel . . . 46
3.5 Surface pressures with and without end-plates for low $\alpha$ for NACA0012 aerofoil profile . . . 47
3.6 Surface pressures with and without end-plates for high $\alpha$ for NACA0012 aerofoil profile . . . 47
3.7 Suction Schematic . . . 48
3.8 Errors in surface pressure measurement at $Re = 1.6 \times 10^5$ . . . 49
3.9 Wind Tunnels . . . 50
3.10 $220kW$ wind tunnel at IIT Bombay . . . 51
3.11 Smoke visualisation, NACA0012 aerofoil, $Re = 3.3 \times 10^4$ . . . 55
3.12 Wool tuft visualisations, S814, $U_\infty = 10m/s$, $Re = 1.6 \times 10^5$ , $\alpha = 20°$ . . . 56
3.13 Surface pressures, NACA0012, $\alpha = 9°$, $Re = 4.1 \times 10^4$ . . . 58
3.14 Suction at $x/c = 0.36$, $Re = 4.9 \times 10^4$, NACA0012 . . . 59
3.15 Surface pressures, $\alpha = 9°$, $3.3 \times 10^4$, S814 profile . . . 61
3.16 $C_L$ for different slit positions, $Re = 4.9 \times 10^4$, S814 . . . 61
3.17 $C_D$ for different slit positions, $Re = 4.1 \times 10^4$ ,S814 . . . 61
3.18 $C_L/C_D$ for different slit positions,$5.7 \times 10^4$, S814 . . . 62
3.19 Optimised efficiency curve using active control . . . 63
3.20 $C_{Pressure}$ for NACA0012 $x/c = 0.36$, $U_\infty = 5m/s$, $Re = 8.2 \times 10^4$ . . . 65
3.21 $C_{Pressure}$ for NACA0012, $x/c = 0.36$, $U_\infty = 20m/s$, $Re = 3.3 \times 10^5$ . . . 66
3.22 $C_{Pressure}$ for S814, $x/c = 0.24$, $U_\infty = 10m/s$, $Re = 1.6 \times 10^5$ . . . 67
3.23 $C_{Pressure}$ for S814, $x/c = 0.24$, $U_\infty = 30m/s$, $Re = 4.9 \times 10^5$ . . . 68
3.24 Change in $C_L$ for NACA0012, constant suction . . . 69
3.25 Change in $C_L$ for S814, constant suction . . . 70
3.26 Wake velocities and $C_D$ for constant suction . . . 72
3.27 $C_L$ improvement, varying suction ($C_\mu$), $Re = 3.3 \times 10^5$ . . . 73

3.28 Wake velocities and $C_D$ for varying $C_\mu$, $Re = 1.6 \times 10^5$, $\alpha = 9°$ . . . . . 75
3.29 Lift curves for NACA0012 . . . . . 76
3.30 System identification of a dynamic system . . . . . 77
3.31 Experimentation schematic for system identification . . . . . 78
3.32 System identification schematic . . . . . 79
3.33 Identification test types . . . . . 81
3.34 Validation test . . . . . 82
3.35 Properties of the LTI models identified through small-step tests . . . . . 84
3.36 Validation Process . . . . . 86
3.37 Measured inputs, measured outputs of the plant overlayed with predictions of the LPV model . . . . . 87

4.1 Reynolds Numbers for the Turbine Blade . . . . . 93
4.2 $C_p$ enhancement for small wind turbines using constant surface suction . . 94
4.3 Power output vs suction power . . . . . 95
4.4 Fore-aft DoF of the tower . . . . . 96
4.5 Actuation effects on $C_L$ . . . . . 97
4.6 Schematic of control structure . . . . . 97
4.7 Sample wind input at hub height, mean speed 13m/s . . . . . 99
4.8 Schematic of control algorithm for pitch control . . . . . 101
4.9 Schematic of control algorithm for suction control . . . . . 102
4.10 Wind gust, class IEC III A, intensity $8m/s$ . . . . . 103
4.11 Tower top fore-aft movement in wind gust . . . . . 104
4.12 Tower fore-aft movement mean position and variance . . . . . 104
4.13 Actuator outputs to simulator . . . . . 105
4.14 Stress cycles for wind speed $7m/s$ . . . . . 108
4.15 Stress cycles for wind speed $13m/s$ . . . . . 109
4.16 Stress cycles for wind speed $17m/s$ . . . . . 110
4.17 Predicted Hourly Stresses . . . . . 111
4.18 Predicted Damage Equivalent for 20 Years Operation . . . . . 113

5.1 Benefits of surface suction for small wind turbines . . . . . 115

B.1 Rainflow count of bending moments for various wind speeds . . . . . 119

# Nomenclature

| | | | |
|---|---|---|---|
| $C_L$ | Coefficient of Lift | $Re$ | Reynolds Number |
| $C_D$ | Coefficient of Drag | $\nu$ | Kinematic Viscosity $m^2/s$ |
| $C_P$ | Coefficient of Power | $N_f$ | Number of Cycles to Failure |
| $\rho$ | Density of Fluid (air) $(kg/m^3)$ | $S$ | Stress $(MPa)$ |
| $A$ | Area $(m^2)$ | $D$ | Damage Equivalent |
| $V$ | Free Stream Velocity $(m/s)$ | $C_{Pressure}$ | Coefficient of Pressure |
| $\lambda$ | Tip Speed Ratio (TSR) | $C_\mu$ | Coefficient of Momentum |
| $\lambda_{opt}$ | Optimum Tip Speed Ratio | $P$ | Pressure $(Pa)$ |
| $V_{cut-in}$ | Cut in Wind Speed $(m/s)$ | $C_N$ | Coefficient of Normal Force |
| $V_{rated}$ | Rated Wind Speed $(m/s)$ | $C_T$ | Coefficient of Tangential Force |
| $V_{cut-out}$ | Cut Out Wind Speed $(m/s)$ | $u_s$ | Suction Velocity $(m/s)$ |
| $L$ | Lift Force $(N)$ | $u$, $\Delta u$ | Suction Pressure (input) $(Pa)$ |
| $D$ | Drag Force $(N)$ | $y$, $\Delta y$ | Suface Pressure (output) $(Pa)$ |
| $\alpha$ | Angle of Attack $(^\circ)$ | $z$ | Forward Shift Operator |
| $r$ | Radius $(m)$ | $K_P$ | Proportional Constant |
| $a$ | Axial Flow Factor | $K_D$ | Derivative Constant |
| $a'$ | Tangential Flow Factor | $s$ | Laplace Complex Argument |
| $c$ | Chord Length $(m)$ | $J$ | Rotor Moment of Inertia $(N.m^2)$ |
| $\Omega$ | Rotational Speed $(rad/s)$ | $R_m$ | Resistance of Motor $(Ohm)$ |
| $U_\infty$ | Free Stream Wind Speed $(m/s)$ | $H$ | Inductance of Motor $(H)$ |
| $U_{rotor}$ | Wind Speed at Rotor $(m/s)$ | $\alpha_w$ | Shape Factor (Weibull Distribution) |
| $W$ | Resultant Velocity at Blade $(m/s)$ | $\beta_w$ | Scale Factor (Weibull Distribution) |
| $N$ | Number of Blades | $x_{ns}$ | x-direction for Navier-Stokes $(m)$ |
| $\sigma$ | Blade Solidity | $y_{ns}$ | y-direction for Navier-Stokes $(m)$ |
| $Q$ | Torque $(N.m)$ | $u_{ns}$ | Velocity in x-direction $(m/s)$ |
| $P$ | Power $(W)$ | $y_{ns}$ | Velocity in y-direction $(m/s)$ |
| $\beta$ | Blade Seting Angle $(^\circ)$ | $\rho_{ns}$ | Density for Navier-Stokes $(kg/m^3)$ |
| $\phi$ | Angle Between $\Omega r$ and $W$ $(^\circ)$ | $p_{ns}$ | Pressure for Navier-Stokes $(Pa)$ |
| $l$ | Characteristic Length $(m)$ | $x_{critical}$ | Point of transition of boundary layer |
| $\mu$ | Dynamic Viscosity $kg/(m.s)$ | | from laminar to turbulent |

# Acronyms

| | |
|---|---|
| CoE | Cost of Energy |
| BEM | Blade Element Momentum (theory) |
| HIP | High Impact Polyesterene |
| LTI | Linear Time Invariant |
| LPV | Linear Parameter Varying |
| ARX | AutoRegressive eXogenous |
| FAST | Fatigue, Aerodynamics, Structures, and Turbulence |
| NREL | National Renewable Energies Laboratory |
| ASTM | American Society for Testing and Materials |
| IEC | International Electrotechnical Commission |

# Chapter 1

# Introduction

## 1.1 Background

Wind is one of the most popular renewable energy sources around the world. The installed capacity at the end of 2012 was over 280 GW, representing an annual cumulative market growth rate of more than 19% over the previous year [FSSQ13]. Improved efficiency, coupled with the longer life of large wind turbines, has helped reduce the cost of energy (CoE) of electricity produced by large wind turbines. CoE from large wind turbines is now comparable to that from conventional sources of energy, that is, INR $3.5 - 6/kWh$. Small wind turbines, however, still have a CoE significantly higher than the conventional sources of energy, that is, close to INR $7.5 - 20/kWh$ (see A.1). Small wind turbines can help provide energy to locations where other sources of energy are not available. In India, where currently more than 33% of the villages do not have access to grid electricity, small-scale renewable energy sources like small wind turbines and photo-voltaics are already becoming increasingly popular. Even in regions with grid connectivity, such sources are gaining popularity because of the unreliability of the supply of grid electricity. Reducing costs would help small turbines gain more acceptance in both, the regions connected to the grid as well as those that are off-grid.

In the last few decades, research has focused mainly on the development of large, commercial wind turbines, which has helped reduce their CoE. Small turbines, however have not seen such a research and development focus. Further, small wind turbines, are usually installed at the point of consumption of energy. More often than not, these locations have a much poorer wind potential as compared to large wind turbine sites.

Consequently, small wind turbines operate in low wind speeds. Coupled with the small size (and chord length) of the turbine blades, the Reynolds numbers ($Re$) for the small wind turbines are an order of magnitude lesser (in the range $10^4$ - $10^5$) than those of the large wind turbines ($> 10^6$). [BSJB01, Woo11]

It is well known that turbine blades are prone to boundary layer separation in low operating $Re$ [Sch00, PK08, Mue02, MH80], which poses significant challenges in realising good aerodynamic efficiency. It is also established that such boundary layer separation may be delayed, or completely avoided, by using active flow-control techniques that include surface suction, use of pulsating jets, suction-blowing, air-jet vortices, among others ([Sch00, SSK+95, Gaz00, PN98, SNAG05, HHLH04, LDCH10, Epp99, Bra99, RM08, GPY+06, DV06, SJL+08, NB94, Mae86, FK88]). In this thesis, the use of surface suction-based flow-control is explored as a method of mitigation of boundary layer separation. Further, the benefits of applying surface-suction over blades of small wind turbines are presented. Formally, the purpose of this thesis is stated below:

## 1.2 Problem definition

This thesis addresses the problem of estimating improvement in blade aerodynamic efficiency and reduction in structural loads in small wind turbines through surface suction-based active flow control at low $Re$. More specifically, the problems addressed are:

i Identification of non-dimensional steady-state and dynamic relations between surface suction, and aerodynamic characteristics of aerofoils at low $Re$.

ii Utilisation of surface-suction, through its identified relations with the aerodynamic characteristics, in a small wind turbine operating in low $Re$, to arrive at estimates of increased power output and mitigated structural loads on the turbine.

### 1.2.1 Prior work

The literature is abundant in aerofoil data for high $Re$ flows, as most of the aerodynamic applications are at higher $Re$. For instance, aeroplanes operate at $Re > 10^7$ and large wind turbines at $Re > 10^6$. Low $Re$ flows have been explored, but the experiments are challenging as it is difficult to achieve repeat-ability and reliability [BRP99, NY12,

ZAY+11] and there is a general the lack of applications for such $Re$. Further, in the past, most techniques of mitigating boundary layer through flow control, too, have focused on higher Reynolds number applications.

Efforts involving the study of low $Re$ applications have largely been directed towards characterising lift and drag data, and for a few aerofoils. To date, there appears to be a dearth of validated experimental data involving the use of active flow control, that may be used for designs relating to low $Re$ applications, including small wind turbines. Further, there also seems to be a lack of studies on flow control applications for wind turbines in general, and for small wind turbines in particular. This thesis aims to address these gaps through flow-control experimentation at low $Re$ and simulations of use of such flow-control for small wind turbines.

### 1.2.2 Approach towards the solution

The approach adopted towards arriving at the aforementioned estimates of improvement in blade aerodynamic efficiency and reduction in structural loads in small wind turbines is as follows.

First, characterisation of improvement in the aerodynamic characteristics of two aerofoil profiles, NACA0012 and S814 in low $Re$ regimes is performed through wind tunnel experiments. NACA0012 is a symmetric aerofoil, for which abundant data is available in the literature. S814 is a cambered aerofoil, which is commonly used in small wind turbine applications. This characterisation captures the steady-state characteristics as well as identifies the temporal dynamics.

Steady-state experiments provide the relation between change in the coefficient of lift ($\Delta C_L$) and change in the coefficient of drag ($\Delta C_D$) with a non-dimensional parameter $C_\mu$, called momentum coefficient. $C_\mu$ is defined as the ratio of the momentum of air drawn through suction and the momentum of the air flowing over the aerofoil. $C_L$ and $C_D$ with suction are expected to be better (that is, positive $\Delta C_L$ and negative $\Delta C_D$). This is because boundary layer separation gets mitigated on applying surface-suction, and this improves the surface pressures over aerofoils.

The temporal experiments characterise how fast $C_\mu$ changes $C_L$ and $C_D$. To obtain this dynamic model between $C_\mu$ and $\Delta C_L$, $\Delta C_D$, a system identification technique is used on empirically obtained input-output data ($C_\mu$ as input, $C_L$, $C_D$ as outputs) The dynamic

model giving a good fit to the empirical data is an over-damped second-order system.

Thus, the steady-state experiments and system identification provide with the following two relations:

1. $\Delta C_L$, $\Delta C_D = f(C_\mu)$

2. $\Delta C_L$, $\Delta C_D = f(C_\mu, t)$

Next, a similitude argument is posed – as long as the dimensionless parameters $C_\mu$ and $Re$ remain comparable to the regimes for which the aforesaid experimental characterisation was done, the steady-state and temporal relationships between $\Delta C_L$, $\Delta C_D$ and $C_\mu$ established can be directly used in numerical simulations for predicting the behaviour of small wind turbines.

Further, the relation $\Delta C_L$, $\Delta C_D = f(C_\mu)$ is used in simulators employing steady Blade Element Momentum (BEM) theory to estimate increase in Coefficient of Power, $C_P$ of a small wind turbine employing surface suction on its blades working in the same $C_\mu$, $Re$ regime.

Finally, The dynamic map, $\Delta C_L$, $\Delta C_D = f(C_\mu, t)$ is incorporated into the dynamics of the aero-elastic simulator, FAST to formulate extended turbine dynamics. $C_\mu$ is utilised, appropriately, as an additional control input towards reducing fore-aft oscillations of the tower top while compensating for the said extended turbine dynamics. Using rain-flow analysis, it was demonstrated that the reduced oscillations resulted in mitigation of fatigue loads on the turbine tower structure, thereby increasing its expected lifetime.

**Main results**

By applying the approach indicated above for increasing $C_P$ to a small wind turbine in sub $1kW$ power output range, with $2m$ radius, NACA0012-blades, operating in steady wind speed of $7.5\,m/s$, increased the expected power output from $764W$ to $1511W$ by expending $106W$ of suction power.

Further, compensating for the extended dynamics of the turbine in the aero-elastic simulator, tower-top oscillations reduced for a $\sim 10kW$ turbine of $2.9m$ radius, S814 blades, hub height $24m$. Thus, for the turbine operating over 20 years in turbulent IEC III-A wind conditions, the structural damage equivalent reduced from $\sim 10$ to $< 1$.

These results establish substantial promise for the use of surface suction for improving aerodynamic efficiency and improving fatigue life of structure of small wind turbines.

## 1.3 Whom will this research benefit

The primary audience for this thesis is the wind energy community. Only recently has flow control been looked at as a means of increasing power output [GBHMV14, GSBH12, SG11]. Further, using flow control for mitigating loads may prove to be a novel alternative to the traditional method of using pitch control, which engineers could explore. This technique may also be used in conjunction with pitch control to increase the combined performance and reduce fatigue further. The findings of this thesis are not limited to small wind turbines only, as the portions of blades of large wind turbines close to the root also operate in low $Re$ and high angles of attack. Fatigue load mitigation through flow control can be extended to large wind turbines if applied to these areas.

Besides wind turbines, experimental results at low $Re$ will be of interest to applications like micro air vehicles (MAVs), unmanned air vehicles (UAVs), and high-altitude long-endurance (HALE) flying vehicles, which also operate in these $Re$. A better understanding of flow control will be beneficial to all such applications. Further, the technique used here for system identification, as well as the identified model will be of interest to applications where an understanding of system dynamics of fluids is required.

## 1.4 Organisation of the report

The report is organised into multiple chapters. Chapter 2 describes a few preliminaries which are required to comprehend the work described in this report and the prior work done in the related fields. Chapter 3 describes the experimental set-up for characterising the effects and dynamics of flow-control using surface suction at the appropriate $Re$. Chapter 4 presents simulation results for increasing power output and mitigating fatigue loads, based on the experimental results. Chapter 5 summarises the report and discusses future work.

# Chapter 2

# Preliminaries and prior work

This chapter details the background required for the reader to appreciate the rest of the thesis. The final results presented in the thesis deal with power output and fatigue of the wind turbine. Thus, the first section discusses the concepts relating to wind turbines, which includes – architecture of turbines, aerodynamics of blades, mathematical framework (through BEM theory) of predicting torque and thrust produced by the rotor, control strategies commonly utilised to control torque and thrust, and how these relate to power output and the fatigue on the structure.

The next section highlights the differences between the operation of small and large wind turbines, particularly low $Re$ that small wind turbines operate, in and the aerodynamic challenges this imposes. The use of surface-suction is proposed as a means to overcome these challenges.

In the next section, the tools necessary for the analysis are presented, starting with a discussion on system theoretic view and system identification. Next, experimentation in a controlled environment, that is, wind tunnel is described. It is followed by a discussion on the use of similitude analysis, which is essential for extending the wind tunnel experimental results to prototype wind turbines. Next, numerical simulators for wind turbine analysis are discussed, followed by a description of wind classification, followed by the formal aspects of fatigue life calculation are discussed.

The preliminaries are followed by a discussion on the relevant prior-work, and gaps in the literature in there areas of research.

## 2.1 Wind turbines, power capture

Wind turbines extract energy by converting the kinetic energy of wind to mechanical work. Most of the contemporary wind turbines belong to the 'Danish' wind turbine concept which consists of an upwind (rotor is ahead of the tower), horizontal axis (rotation is around the horizontal axis), three-bladed, stall-regulated rotor, yaw-enabled (rotor can be turned (yawed) into the direction of the wind), variable speed (rotor and generator speed not coupled to the grid frequency) and a doubly-fed induction machine drive train. Such a turbine is shown in Figure 2.1.

Figure 2.1: Large, three bladed, upwind Horizontal Axis Wind Turbine (HAWT)

The wind power flowing through the wind turbine rotor area is the product of mass flow rate ($\rho AV$) and the energy per unit mass, ($1/2V^2$). The ratio of the power extracted from the wind to the power of the wind flowing through the area swept by the rotor is called Coefficient of Power ($C_P$):

$$C_P = \frac{P}{\frac{1}{2}\rho A V^3} \tag{2.1}$$

where $P$, $\rho$, $A$ and $V$ are the mechanical power captured, density of air, rotor area and free stream wind velocity. Theoretically, wind turbines are limited to a maximum $C_P$ of $16/27 \sim 0.593$, which is known as the Betz coefficient. This limit was derived

by Betz using the principles of conservation of mass and momentum of the air stream flowing through an idealised 'actuator disc' [Bet66]. Large wind turbines have been able to achieve up to 75% to 80% of the Betz limit.

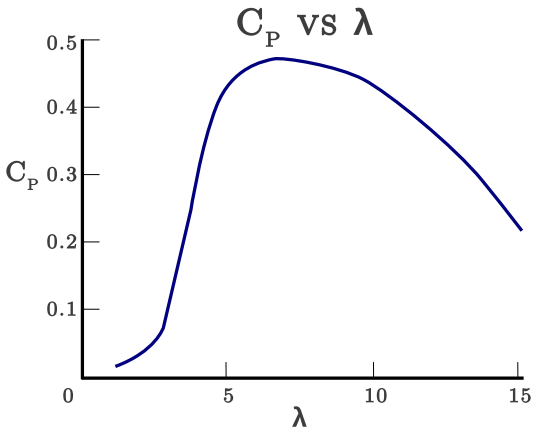


Figure 2.2: $C_P$ vs $\lambda$ for a typical three bladed turbine [BSJB01]

It is well known that $C_P$ is a function of the tip speed ratio ($\lambda$), that is, the ratio of linear velocity of the blade tip to the free stream wind velocity. A typical variation of $C_P$ with $\lambda$ is shown in Figure 2.2. All other variables, including pitch, are assumed constant. It can be seen that maximum $C_P$ occurs for a optimum value of $\lambda_{opt}$ of the tip speed ratio. Thus, to maximise $C_P$ at variable wind speed, the speed of the rotor ($\Omega$) has to be varied to keep $\lambda$ at $\lambda_{opt}$.

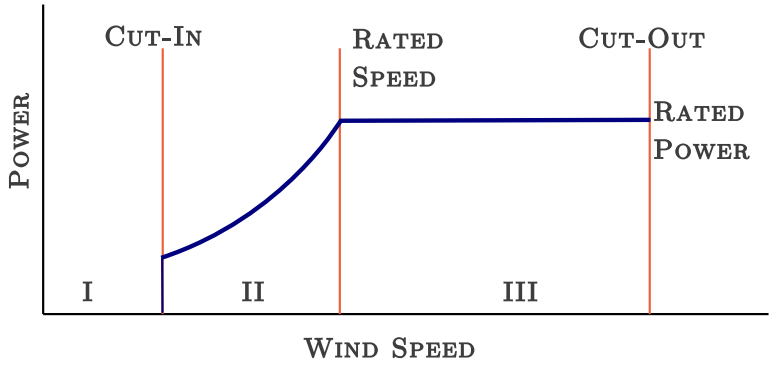


Figure 2.3: Wind turbine control regions

Wind turbines are unable to produce useful power at very low wind speeds. The smallest wind speed above which useful power capture becomes possible is called the 'cut in' speed. The operating region below this speed is called 'Region I'. The blades are pitched out to produce least torque and rotor is left 'idle' to freely rotate in this

region. Once the wind speed rises above 'cut in' speed, the pitch is decreased and the rotor is slowly accelerated. From the 'cut in' speed to the rated speed ($V_{rated}$), the power captured by the wind turbine increases with the wind speed. This region of operation is called 'Region II'. The operating objective is to maximise power capture in this region. Above the rated wind speed, the power captured by the turbine is limited to the rated power, in order to maintain the loads on the generator, turbine and the tower within the design limits. This region of operation is called 'Region III'. Due to safety considerations, the turbine is shut down for wind speeds exceeding the 'cut-out' speed. The blades are pitched out, and the rotor may be mechanically braked to prevent runaway rotation of the rotor. Figure 2.3 shows these regions of operation.

## 2.2 Blade aerodynamics

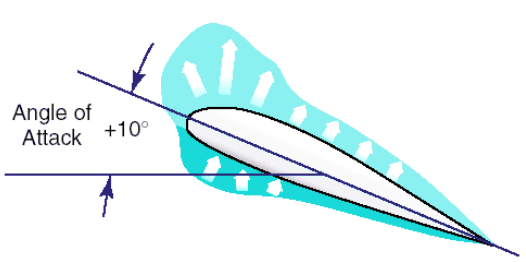


(a) Pressure distribution over an aerofoil [Aer06]

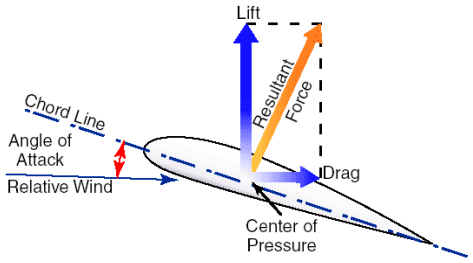


(b) Resultant forces on an aerofoil [Aer06]

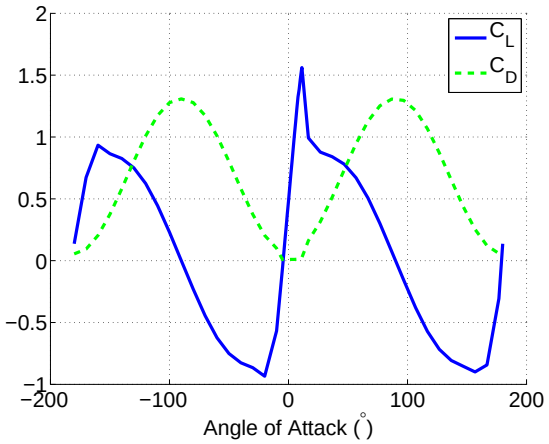


(c) $C_L$ and $C_D$ curves [CM05] for S814 aerofoil

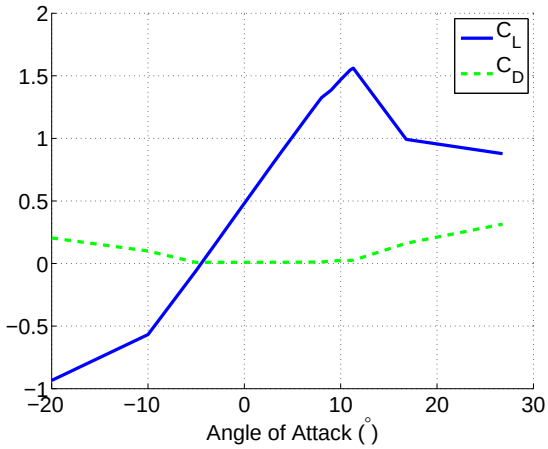


(d) $C_L$ and $C_D$ for S814 close to 0°

Figure 2.4: Aerofoil characteristics

The cross-section of a typical turbine blade has an aerofoil profile. On moving

through air, aerofoils induce higher wind speed over the upper surface (known as suction surface), lower wind speed at the lower surface (known as the pressure surface), and an overall circulation in the wind. Consequently, a pressure differential is created on the suction and pressure surfaces, particularly a large low pressure region occurs close to the leading edge on the upper surface. The pressure differential thus created results in an 'upwards' force, called Lift ($L$) and a 'horizontal' force called Drag ($D$). Figure 2.4 shows typical pressure distribution and the resultant forces on an horizontal aerofoil. These forces are a function of the aerofoil profile, free stream velocity ($V$), air density ($\rho$), angle of attack ($\alpha$) and the area of the aerofoil ($A$). It is useful to define Coefficient of Lift ($C_L$) and Coefficient of Drag ($C_D$) as dimensionless coefficients that relate the lift and drag generated by an aerofoil to these factors as:

$$C_L = \frac{L}{\frac{1}{2}\rho V^2 A}$$
$$C_D = \frac{D}{\frac{1}{2}\rho V^2 A} \tag{2.2}$$

**Aerofoil profiles**

Two aerofoil profiles have been used in the experiments for this thesis, NACA0012 and S814. NACA0012 is a basic aerofoil profile, and has abundant experimental data in literature for validation. S814 is a popular aerofoil profile for small wind turbines, and for near-root regions of large wind turbine blades. The $C_L$ and $C_D$ of S814 are shown in Figures 2.4(c) and 2.4(d).

### 2.2.1 Blade Element Momentum (BEM theory)

The Blade Element Momentum (BEM) theory [BSJB01, PAWLC11] is a well known mathematical method for modelling the aerodynamics and torque production of a wind turbine. The blade element theory divides the blades into multiple span-wise elements at a distance $r$ and of span $\delta r$ for the purpose of analysis (Figure 2.5(a)). It is assumed that each annular ring thus formed is independent of other rings and the aerodynamic forces on the elements in the ring are responsible for the change in momentum of the air which passes through the annulus swept by the blade elements. It is further assumed that the aerodynamic forces at a section of the blade are a function of blade geometry; the forces on a radial blade element can be calculated using two-dimensional aerodynamic

characteristics of the aerofoil. The velocity component in the span-wise direction and three-dimensional effects are ignored.

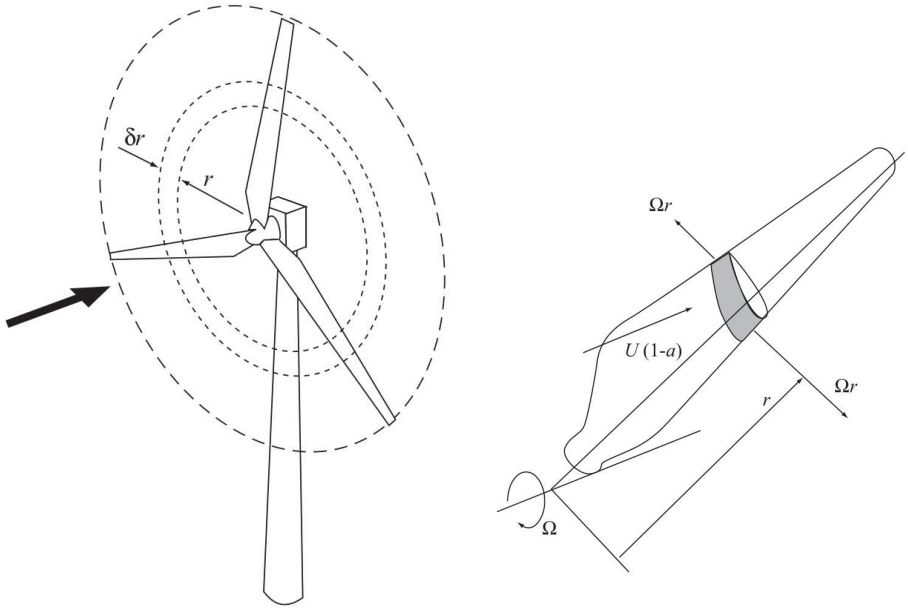


(a) Annular ring (b) Blade element

Figure 2.5: Blade element and annular ring [BSJB01]

Figure 2.5(b) shows a blade element and its component velocities. The chord length of the element is denoted as $c$ and the blade setting angle as $\beta$. The angular velocity of the rotor is denoted as $\Omega$. The axial flow factor, $a$, characterises change in velocity across the rotor. The tangential flow factor $a'$, tip loss factor etc have been approximated for the steady state analysis. Their combined loss is taken as 10% of the power produced by the rotor. If the axial flow factor does not vary radially, it can be assumed that there is no interaction between the rings. Though the axial flow factor is found to vary, the experimental examination by Lock [Loc24] shows that the radial independence assumption is valid [BSJB01].

$$a = \frac{U_\infty - U_{rotor}}{U_\infty} \tag{2.3}$$

Figure 2.6(a) shows the resultant velocities at the blade:

$$W = \sqrt{U_\infty^2(1-a)^2 + \Omega^2 r^2} \tag{2.4}$$

$W$ acts at an angle of $\phi$ to the plane of rotation, such that:

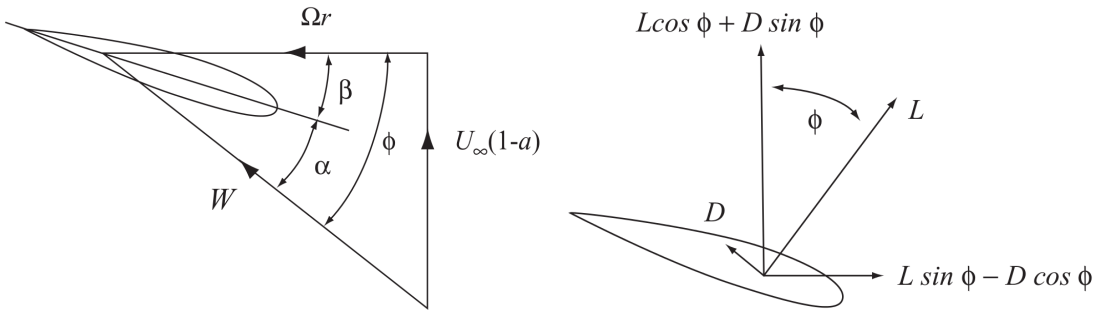


(a) Resultant velocities (b) Resultant forces

Figure 2.6: Resultant forces and velocities for blade elements [BSJB01]

$$\sin(\phi) = \frac{U_\infty(1-a)}{W} \cos(\phi) = \frac{\Omega r}{W} \tag{2.5}$$

The radial component of velocity ($\omega \times r$) increases with $r$. Thus, the blade is twisted over the length, in order to have a favourable angle of attack. The local setting angle is $\beta$, hence, the angle of attack, $\alpha = \phi - \beta$. The lift and drag on the blade element are given by:

$$\delta L = \frac{1}{2}\rho W^2 c C_L \delta r \tag{2.6}$$

$$\delta D = \frac{1}{2}\rho W^2 c C_D \delta r \tag{2.7}$$

The BEM theory assumes that the change in momentum of the air passing through the annular ring is caused solely by the forces of the blade. The rate of change of axial momentum of the air passing through an annular ring is given by:

$$4\pi U_\infty^2 a(1-a) r \delta r \tag{2.8}$$

The axial component of the aerodynamic forces acting on the N blades in the annular ring is

$$\delta L \cos\phi + \delta D \sin\phi = \frac{1}{2}\rho W^2 N c (C_L \cos\phi + C_D \sin\phi)\delta r \tag{2.9}$$

This force is responsible for the change in momentum, thus:

$$\frac{1}{2}\rho W^2 N c (C_L \cos\phi + C_D \sin\phi)\delta r = 4\pi U_\infty^2 a(1-a) r \delta r \tag{2.10}$$

The axial flow factor is obtained by iteratively solving the previous equation. A convenient way of representing this relation is:

$$\frac{a}{1-a} = \frac{\sigma_r}{4\sin\phi^2}\left(C_L\cos\phi + C_D\sin\phi - \frac{\sigma_r}{4\sin\phi^2}(C_L\sin\phi - C_D\cos\phi)^2\right) \tag{2.11}$$

where $\sigma$ is the blade solidity, that is, the ratio of the blade area and the disc area. Chord solidity, $\sigma_r$ is the ratio of the total blade chord length and the circumference of the annular ring:

$$\sigma_r = \frac{Nc}{2\pi r} \tag{2.12}$$

After obtaining the axial factor, the previously defined calculations are repeated to find the updated parameters. Using the updated values of the parameters, the torque produced by each annular ring is calculated as:

$$\delta Q = N\delta r(\delta L\cos\phi - \delta D\sin\phi)r \tag{2.13}$$

The power produced by each ring is $\Omega \times \delta Q$. The total power generated by the rotor is:

$$P = \int_R \Omega\delta Q \tag{2.14}$$

The power coefficient, defined as ratio power produced and power available, is thus:

$$C_P = \frac{P}{\frac{1}{2}\rho U_\infty^3 \pi R^2} \tag{2.15}$$

## 2.3 Wind turbine control strategies

For large wind turbines, microprocessor based controllers function at three broad levels – supervisory control, closed loop control and safety control [BSJB01]. Supervisory control may be considered as the means to change the operational state of the turbine, for example, from standby to power production. Closed loop control automatically adjusts the operational state of the turbine, for example, for control of the generator torque to regulate rotational speed, control of blade pitch and others. Safety control typically works

distinctly from the main control system of the turbine and its function is to bring the turbine to a safe state in a problematic event.

The closed loop control objectives relating to wind turbines can be classified depending on operating conditions. In 'Region II' (see Figure 2.3), that is, below rated wind speed, the primary objective is to maximise capture of power. Above the rated wind speed, that is, 'Region III', the generator speed and torque are maintained at a constant value, to keep the loads on the generator and structure within design limits [BSJB01, Bos00, SD05]. The two most popular methods to realise these control objectives are 'Torque Control' and 'Pitch Control':

### 2.3.1 Torque control (control action below rated speed)

The turbines, almost always support variable speed operation. In order to support variable speed, the generator speed is not rigidly coupled to the grid frequency. The most popular generators have a wound rotor induction generator with its stator connected directly to the network, and with its rotor connected to the network through slip rings and a frequency converter [BSJB01]. This is called a Doubly Fed Induction Generator (DFIG), and enables active control of both, speed and torque on the generator.

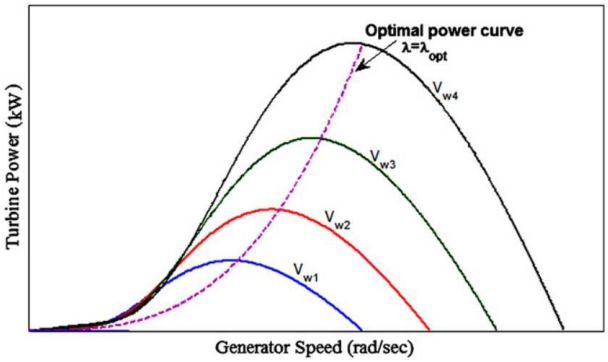


Figure 2.7: Turbine power as a function of the rotor speed for varying wind speed [AYTS12]

Between the cut-in speed and rated speed, the control objective is to maximise power capture. Maximum $C_P$ occurs at $\lambda_{opt}$, thus, rotor speed is proportional to $V$ (see Figure 2.7). The power generated is a function of $V^3$, and torque is proportional to $V^2$. Using these relations, it can be calculated that the torque demand, $Q_G$ should be proportional to $\Omega^2$ [Bos00]:

$$Q_G = \frac{\pi \rho R^5 C_P}{2\lambda_{opt}^3 G^3} \Omega^2 \tag{2.16}$$

The rotational speed and torque, both are controlled by the generator to respond to the incoming wind disturbance. This method is used below rated speed (Region I) and is called 'torque control' method.

### 2.3.2 Pitch control (control action above rated speed)

Most of the wind turbines support blade pitch action, that is, the blade can be pitched along its longitudinal axis. The pitching action enables the variation of the operating angle of attack, $\alpha$ by regulating pitch angle $\beta$. From the BEM analysis, it can be seen that $C_P$ and $\lambda_{opt}$ depend upon the operating $\beta$. For every mean wind speed, $\lambda_{opt}$ and thus, max $C_P$ occurs at an optimal pitch angle, $\beta_{opt}$. It follows that either increasing or decreasing the pitch would lead to a reduction in torque and thrust. Figure 2.8 shows the relation of $C_P$ and $\lambda$ with $\beta$.

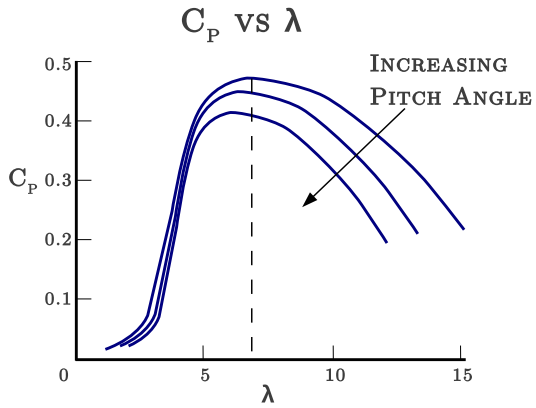


Figure 2.8: $C_P$ and $\lambda$ vs $\beta$

An increase in pitch reduces the angle of attack ($\alpha = \phi - \beta$) thus reducing the lift, hence, torque and thrust. This is known as 'pitching towards feather' [BSJB01]. A decrease in pitch increases the angle of attack towards stall, which pushes some part of the blade over the stall angle, reducing lift and increasing drag, thus reducing torque and thrust. This is known as 'pitching towards stall'. Pitching towards stall requires lesser dynamic pitching activity than pitching to feather. Once a substantial part of the blade is in stall, very small pitch movements increase or decrease the part of the blade under stall, where the rate of change of lift and drag is significantly higher.

Between the rated speed and cut-out speed (Region III), the control objective is to keep the power output and the loads within pre-determined design loads. In order to achieve this, the generator torque and speed are desired to be kept constant. Thus, with increase in wind speed, the demanded rotor speed and torque remain constant. The blades are continuously pitched in response to wind disturbances to maintain the rotor speed within the slip-range of the generator. A turbine employing this method of control, called 'pitch control', does not operate at $\lambda_{opt}$ and $\beta_{opt}$, and thus, $C_{P,max}$. If the turbine were to operate at $C_{P,max}$ even at higher wind speeds, the generator and the structure would have to be able to withstand far higher loads, thus increasing costs.

### 2.3.3 Control action over full range of wind speeds:

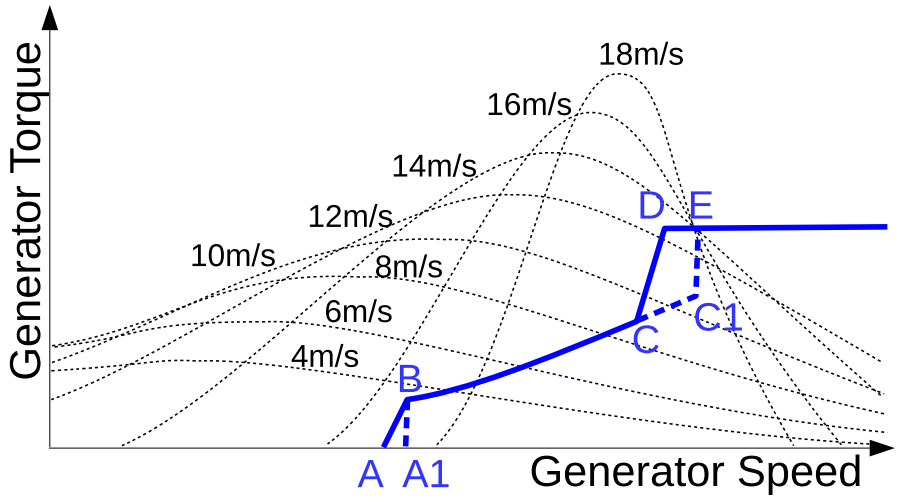


Figure 2.9: Control schematic for variable speed operation [Bos00]

The control schematic for the whole range of wind speeds is shown in Figure 2.9. The path 'BC' represents the desired control above the 'cut-in' speed and below the rated speed. Above the rated wind speed, that is, right of D, the generator torque is kept constant and the generator speed is varied. If the torque-speed trajectory follows A1-B-C1-E instead of A-B-C-D-E, the turbine stays closer to optimum $C_P$, giving slightly higher energy capture [Bos94]. However, the control deviates from either of the two trajectories in turbulent winds, specially for heavy rotors [BSJB01]. Thus for optimised variable speed operation, along with maximising $C_P$, it is important to ensure that the $C_P - \lambda$ curve does not have a sharp peak.

## 2.4 Small versus large wind turbines

International Electrotechnical Commission (IEC) defines small wind turbines in terms of swept area of the rotor. The IEC standard 61400 [Int08a] covers large wind turbines. IEC standard 61400-2 [Int08b] describes small wind turbines having swept area less than $200m^2$, or roughly $200kW$ of rated power. The standard covers Horizontal Axis Wind Turbines (HAWTs), which are the most popular design of turbines. This thesis also deals with HAWTs.

Large wind turbines typically have active yaw control to orient the rotor into the wind as well as have active pitch controlled blades to tap optimum power. Small wind turbines may or may not have these capabilities. Many small wind turbines use a tail fin to orient the turbine with the wind direction. This is referred to as 'free-yaw'. The power produced is controlled by stall controlled blades, or by yawing out (using a mechanical drive as opposed to free-yawing) of the wind direction in high wind speeds. A few small turbines have both active yaw and active pitch control. This thesis analyses two turbines as described in Tables 4.1 and 4.2. The first turbine does not have either yaw control or pitch control. The second turbine employs pitch control.

The most important distinction between large and small wind turbines, however is the relative wind speeds seen by the blade elements. Large scale wind turbines are predominantly used for commercial energy production. They are usually connected to a power grid and are installed at high wind potential locations, which are far from human settlements. Small wind turbines, however, are usually installed at the point of consumption of energy. More often than not, these locations have poor wind potential. Consequently, small wind turbines have to operate in low wind speeds. Coupled with the small size (and thus, chord length) of the turbine blades, the Reynolds numbers for the small wind turbines are an order of magnitude lesser than those of the large wind turbines.

Reynolds number ($Re$) is a dimensionless quantity that is used to help predict similar flow patterns in different fluid flow situations. $Re$ is defined as the order-of-magnitude of the ratio of inertial forces to viscous forces $\left(Re = O\left[\frac{\rho V l}{\mu}\right]\right)$, where $\rho$ is the density of the fluid, $V$ is the mean free stream velocity, $l$ is the characteristic linear dimension and $\mu$ is the dynamic viscosity of the fluid. Small wind turbines typically operate in

*Re* ranging from $10^4$ - $10^5$, as compared to $10^6$ and higher, for the large wind turbines. [BSJB01, Woo11]

The most important factor of difference in operating conditions of Small Wind Turbines is the Reynolds number range. The main focus of this thesis is to to improve the performance of small wind turbines in low Reynolds number regimes. Further discussions will cater to this objective.

### 2.4.1 Low Reynolds number flows

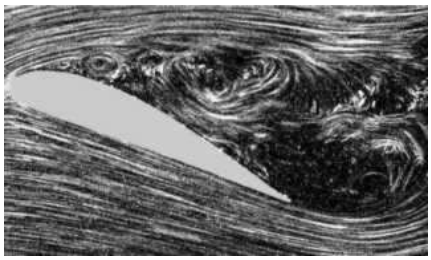

(a) Fully separated flow [Sch00]

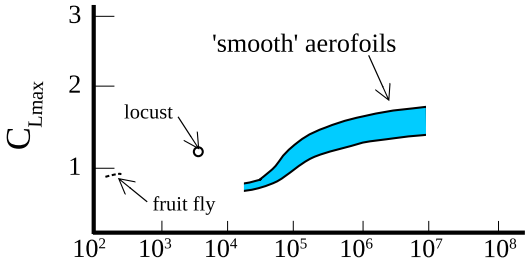


(b) Max section $C_L$ for low Reynolds numbers[MH80]

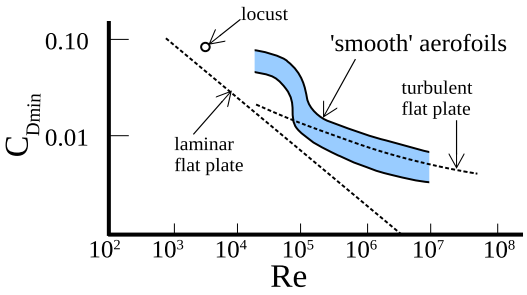


(c) Min section $C_D$ for low Reynolds numbers[MH80]

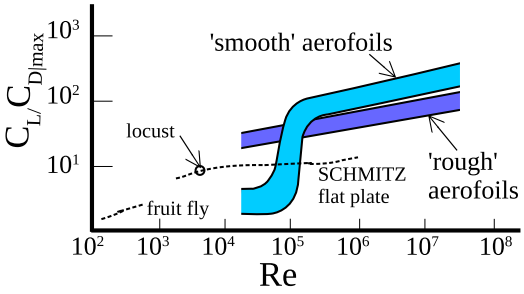


(d) Aerodynamic efficiency for low Reynolds numbers[MH80]

Figure 2.10: Low *Re* effects

Low Reynolds Number flows are characterised by dominant viscous effects, which cause the boundary layer to separate even at low angles of attack[Sch00, PK08, Mue02, MH80]. Figure 2.10(a) shows a fully separated flow over an aerofoil. Although such separation occurs only at the stall angle, the boundary layer separates close to the trailing edge even for low angles of attack for aerofoils operating at low *Re*. This point of separation steadily moves towards the leading edge with the increase in the angle of attack, leading to stall at lower angles of attack as compared to high *Re* flows. The aerofoils, due to this

separation, have lower coefficients of lift ($C_L$) and higher coefficients of drag($C_D$) at low $Re$ (Figures 2.10(b) and 2.10(c)). The efficiency of the aerofoils ($C_L/C_D$), thus, decreases significantly for low Reynolds number flows. Figure 2.10(d) highlights the drop in efficiency of aerofoils at low $Re$. It is worth noting that the drop in efficiency is particularly severe close to $10^5$, which is the operating regime of small wind turbines.

### 2.4.2 Boundary layer and its separation at low $Re$

Air flow around an aerofoil can by analysed by dividing the flow into two regions: an outer region of inviscid flow, and a small flow region near the aerofoil where viscous effects dominate [PK08]. The region near the aerofoil surface consists of slow moving air and is prone to viscous effects. This part of the flow is known as the boundary layer. The thickness of this layer is generally considered to be the distance from the surface of the aerofoil to the point along the normal to the surface where the viscous flow velocity is 99% of the free-stream velocity. Majority of the drag experienced by a body in a fluid is created inside the boundary layer. The outer inviscid flow is faster moving air and determines the pressure distribution around the aerofoil. The outer flow thus determines the Lift force on the aerofoil.

At the leading edge, the boundary layer is laminar. Downstream along the surface of the aerofoil, the flow inside the boundary layer transitions to turbulent flow (Figure 2.11(a)). At high $Re$, this transition is quick and the turbulent flow inside the layer is able to effectively overcome the adverse pressure gradient downstream of the minimum pressure. However, for low Reynolds number flows, the boundary layer on an aerofoil often remains laminar in the adverse pressure gradient region. When the boundary layer travels far enough against the adverse pressure gradient, the speed of the boundary layer may drop to zero, or in extreme cases, even reverse the direction (Figure 2.11(b)). This detaches the flow from the surface of the aerofoil and results in the formation of eddies and vortices downstream of the point of detachment. This detachment of the flow from the surface is called *boundary layer separation*. This often results in increased drag, reduced lift and thus highly reduced efficiency, as seen in Figures 2.10(b), 2.10(c) and 2.10(d).

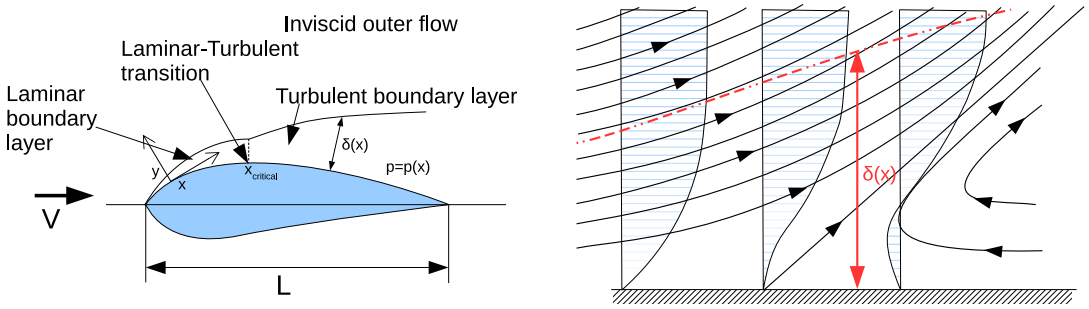


(a) Boundary layer transition over an aerofoil (b) Velocity distribution inside a boundary layer

Figure 2.11: Boundary layer properties [Sch00]

## 2.5 Suction-based flow-control for boundary layer separation

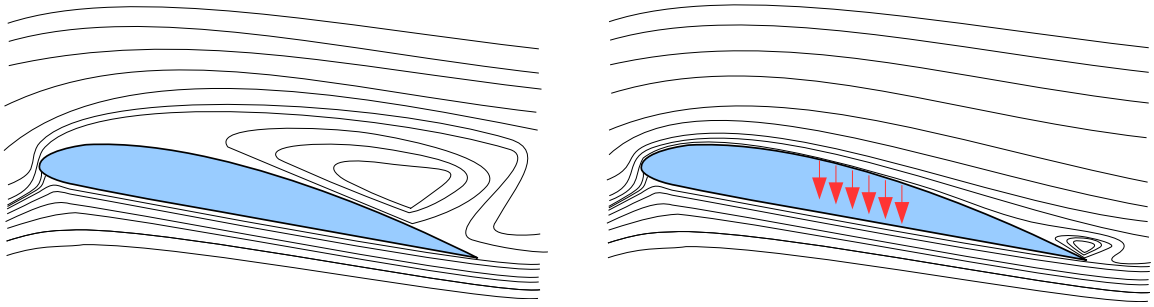

(a) Separation over aerofoil

(b) Separation control over aerofoil using surface suction

Figure 2.12: Control of boundary layer separation by employing surface-suction

It is well-known that boundary layer separation may be delayed by applying active flow control techniques that include surface suction , use of pulsating jets, suction-blowing, air-jet vortices , among others ([Sch00, SSK+95, Gaz00, PN98, SNAG05, HHLH04, LDCH10, Epp99, Bra99, RM08, GPY+06, DV06, SJL+08, NB94, Mae86, FK88]). In this thesis, surface suction has been employed for flow control.

Navier-Stokes equations are used to analyse the flow of viscous fluids. Boundary layer suction, too can be modelled using Navier-Stokes equations. The exact solution for homogeneous suction over an infinite plate is [Lac14, Wue61] :

$$u_{ns}(y_{ns}) = U_{\infty}\left(1 - e^{u_s y_{ns}/\nu}\right) \tag{2.17}$$

where $u_{ns}$ is the velocity in the boundary layer, $y_{ns}$ is the normal distance from the surface of the plate, $u_s$ is the suction velocity at the plate and $\nu$ is the kinematic viscosity. A two dimensional flow with suction through permeable walls can be modelled using the equations of non-permeable walls and changing the boundary conditions [Wue61]:

$$u_{ns}\frac{\partial u_{ns}}{\partial x} + v_{ns}\frac{\partial u_{ns}}{\partial y_{ns}} = -\frac{1}{\rho}\frac{\partial p_{ns}}{\partial x} + \nu\frac{\partial^2 u_{ns}}{\partial y_{ns}^2} \tag{2.18}$$

$$\frac{\partial u_{ns}}{\partial x_{ns}} + \frac{\partial v_{ns}}{\partial y_{ns}} = 0 \tag{2.19}$$

with boundary conditions:

$$u_{ns}(x_{ns}, 0) = 0 \tag{2.20}$$

$$v_{ns}(x_{ns}, 0) = v_{0,ns}(x_{ns}) \tag{2.21}$$

$$\lim_{y_{ns}\to\infty} u_{ns}(x_{ns}, y_{ns}) = U_\infty(x_{ns}) \tag{2.22}$$

$$\tag{2.23}$$

and initial condition

$$u_{ns}(0, y_{ns}) = U_\infty(0) \tag{2.24}$$

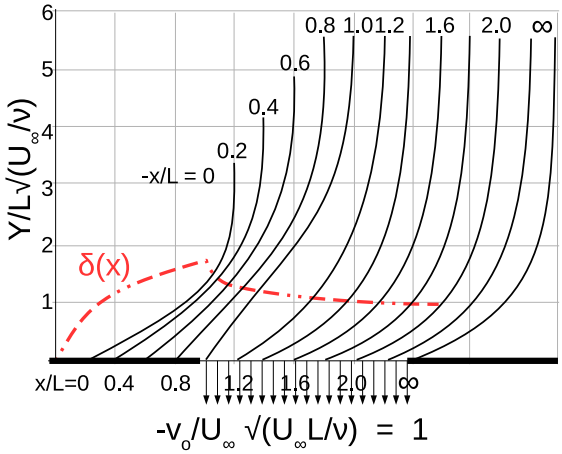


Figure 2.13: Velocity distribution and boundary layer for surface suction starting a finite distance downstream of leading edge of plate

For a further discussion on exact solution, the text by [Wue61] can be referred to. For constant suction applied on a plate, starting a finite distance downstream of start of flow, an approximate solution has been presented by [Wue61] using 'finite difference

method'. Figure 2.13 shows the velocity distribution and boundary layer estimated by the approximate model.

Wind turbines predominantly use cambered aerofoils. The flow across a cambered aerofoil profile is more complex than a flat plate. Hence, experimental data was preferred in this thesis over approximated analytical models. In the past, most of experimental efforts aimed at realising delayed boundary layer separation through flow control have focused on higher Reynolds number applications. Efforts involving study of low Reynolds number applications have largely been directed only towards characterising lift and drag data for a few aerofoils. To date, there appears to be a dearth of validated experimental data involving the use of active flow control that may be used for designs relating to low $Re$ applications, including small wind turbines.

The experimental part of this thesis (Chapter 3) aims to address this lack, specifically, aerodynamic characteristics relating to two aerofoils, namely NACA0012 and S814 which operate in low $Re$ regimes, with suction control (Figure 2.12) incorporated, is reported. The Reynolds numbers of the experiments ranges from $8 \times 10^4$ to $4.8 \times 10^5$, which correspond to the range of operation of small wind turbines. The two relevant quantifiable results of the experiments are:

i change in $C_L$ and $C_D$ (that is, $\Delta C_L$ and $\Delta C_D$) with $C_\mu$

ii identification of dynamics between $\Delta C_L$ and $\Delta C_D$ with $C_\mu$

## 2.6 System theoretic view

System dynamics is defined as an approach to understanding the behaviour of complex systems over time. A system or a "plant" is regarded as an object in which variables of different kinds interact and produce observable signals [Lju98]. The observable signals of interest are called outputs. The variables associated with the system may be both, internal and external. The external stimuli that can be manipulated by the user are called inputs. Other variables which cannot be influenced by the user are called disturbances.

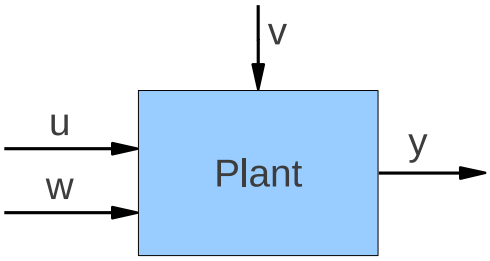


Figure 2.14: A plant with output $y$, input $u$, measured disturbance $w$, and unmeasured disturbance $v$

### 2.6.1 Linear Time Invariant (LTI) system

Consider a plant with a scalar input signal $u(t)$ and a scalar output signal $y(t)$. The system is said to be time invariant if its response to a certain input does not depend on absolute time (Equation 2.25) [Lju98]. It is said to be linear if its output response to a linear combination of inputs is the same linear combination of the output responses of those individual inputs (Equation 2.26). The plant is said to be Linear Time Invariant (LTI), if it satisfies both criteria of time-invariance and linearity.

$$\begin{aligned} y(t) &= H\{x(t)\} \\ y(t+\delta) &= H\{x(t+\delta)\} \end{aligned} \tag{2.25}$$

$$\begin{aligned} y_1(t) &= H\{x_1(t)\} \\ y_2(t) &= H\{x_2(t)\} \\ \alpha y_1(t) + \beta y_2(t) &= H\{\alpha x_1(t) + \beta x_2(t)\} \end{aligned} \tag{2.26}$$

### 2.6.2 Transient and steady state response

Consider the output of a second order linear time invariant system (Figure 2.15) to a step input. (The order of the system is defined by the number of independent energy storage elements in the system, and intuitively by the highest degree of the linear differential equation that describes the system.) Initially, the output changes rapidly, and slows down as it approaches its final value. The response between the two equilibrium states is known as transient response. The steady-state response of the system is the response after the transient response has ended. The amount of time it takes for the system output to reach the desired value (before the transient response has ended, typically) is known

as the rise time. The amount of time it takes for the transient response to end and the steady-state response to begin is known as the settling time [OY70].

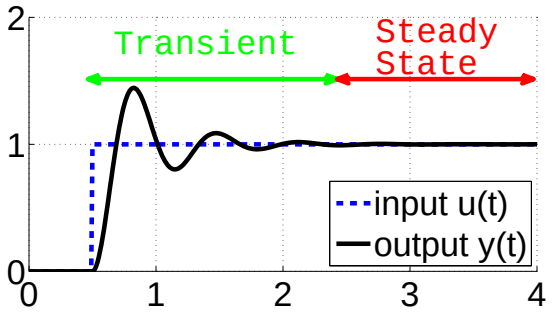


Figure 2.15: Transient and steady state response to a step input

### 2.6.3 Transfer function

A Transfer Function is the ratio of the output of a system to the input of a system, in the Laplace domain considering its initial conditions and equilibrium point to be zero [OY70]. For an input function of $X(s)$, and an output function $Y(s)$, the transfer function $H(s)$ is defined as:

$$H(s) = \frac{Y(s)}{X(s)} \tag{2.27}$$

#### Poles and zeros

Poles and Zeros of a transfer function are the values of the complex variable $s$, for which the denominator and numerator of transfer function become zero, respectively. The values of the poles and the zeros of a system determine whether the system is stable, and how well the system performs.

#### Frequency response and Bode plot

Dynamic systems respond differently to inputs of different frequencies. A system may amplify or attenuate components of a particular frequency (Figure 2.16). The way that the system output is related to the system input for different frequencies is called the frequency response of the system. A Bode plot (Figure 2.17) is a useful tool that shows the gain and phase response of a given LTI system for different frequencies.

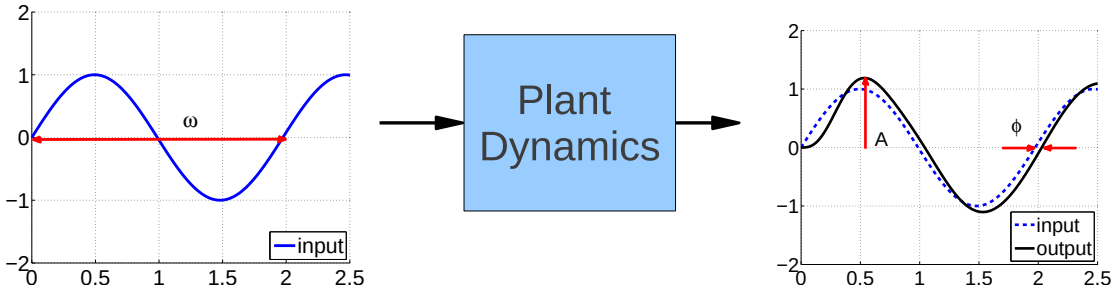


Figure 2.16: Response of a dynamic system to single frequency input

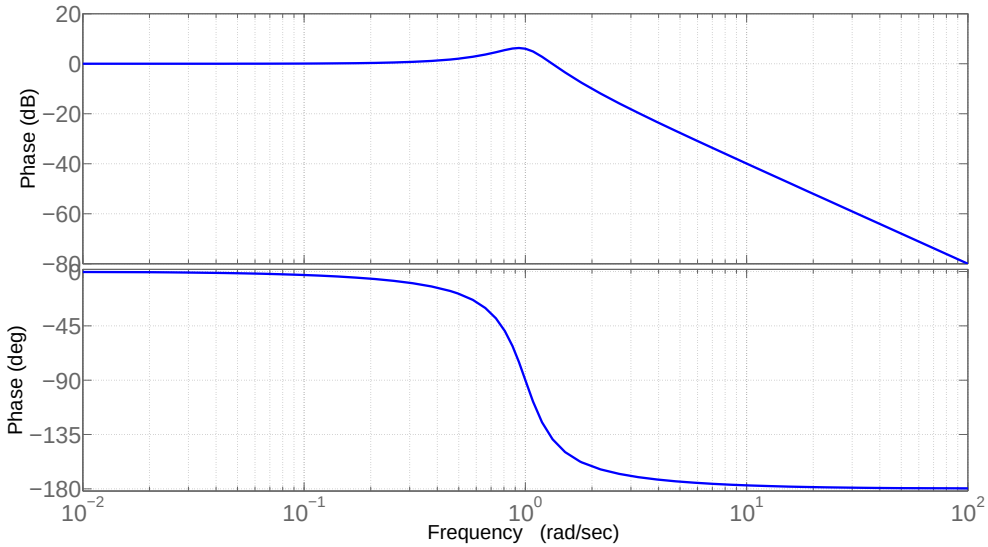


Figure 2.17: An example of a Bode plot

### 2.6.4 Closed-loop control system

In a closed loop controller aims at maintaining output of a system ($y$) at desired reference input ($r$) using feedback (see Figure 2.18). Feedback here refers to sensing of the current value of $y$ , subtracting from $r$ to obtain $e$, which is given as input to the controller. Thus, the value of $y$ is fed back into the control loop. The controller calculates the appropriate input to the plant, $u$ according to the chosen 'control algorithm'.

Proportional-Derivative (PD) control algorithm is used for closed-loop control in this thesis. This implies that $u$ is a sum of two correcting terms, one is proportional to $e$, and the other is proportional to derivative of $e$. thus, the input to the plant is of the form:

$$u(t) = K_p e(t) + K_d \frac{\mathrm{d}}{\mathrm{dt}} e(t) \tag{2.28}$$

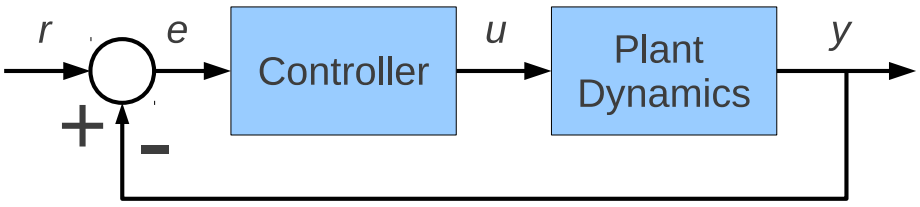


Figure 2.18: Closed loop control system

where $K_p$ and $K_d$ are known as proportionality and derivative constants, respectively. These constants can be chosen appropriately, using control theory, to get a stable control system which aims to keep $y$ close to $r$.

## 2.7 System identification

System Identification deals with inferring mathematical models of dynamic systems, using statistical tools on experimental data from the system. More often than not, special experiments are designed to gather relevant data for use with specific statistical methods.In the discussion in 2.6, the mathematical model of the dynamic system is known, and the output is predicted for a given input. System Identification, on the other hand consists of conducting experiments, recording data, and inferring the mathematical model of the dynamic system using statistical tools (Figure 2.19).

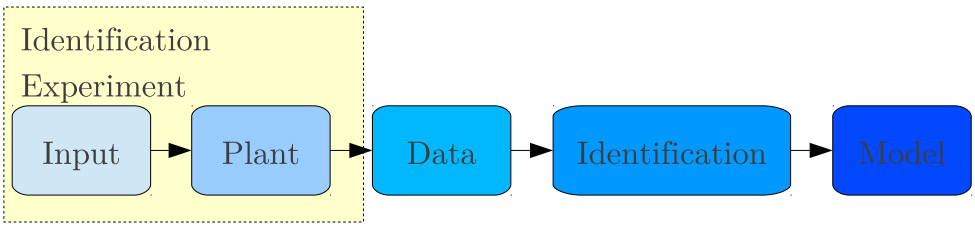


Figure 2.19: System identification of a dynamic system

### 2.7.1 AutoRegressive eXogenous model (ARX)

An assumed mathematical relationship between observable variables of a system is called a model of the system. A model need not be a true and accurate description of the system. These models can take many forms. ARX (AutoRegressive with eXogenous input) is one such discrete-time model which provides a fast and efficient solution by means of a least

squares approach [Lju98]. A second order ARX model was used for the identification process in this thesis. The structure of the second order system for input $u$, and output $y$, was taken as:

$$A(z)y(t) = B(z)u(t) + e(t) \tag{2.29}$$

*where*

$$\begin{aligned} A(z) &= 1 + A_1 z^{-1} + A_2 z^{-2} \\ B(z) &= 1 + B_1 z^{-1} \end{aligned} \tag{2.30}$$

for a second order system, with *forward shift operator* $z$

$$zu(t) = u(t+1) \tag{2.31}$$

and *backward shift operator* $z^{-1}$

$$z^{-1}u(t) = u(t-1) \tag{2.32}$$

and noise component $e$.

It must be noted that the ARX is a linear, time invariant (LTI) model, i.e. the matrices $A$ and $B$ do not depend upon absolute time, or operating conditions.

### 2.7.2 Piecewise linearization of a parameter varying model

If, however, the matrices $A$ and $B$ vary over time, or operating conditions, approximations need to be applied. In the setup described in the thesis, the matrix $B$ changes with the operating value of $u$, while $A$ remains constant throughout. To obtain $B$ over the range of $u$, small-step changes are made to $u$ and the resulting 'piece' of the system is identified, assuming $B$ remains constant for the small step change. This makes the system linear for that 'piece' of response. For the whole range of response, $B$ is updated for every discrete step, and the response is 'stitched' over the whole range of $u$. Assumption has been made that for every discrete-time prediction, the absolute value of $u$ does not change significantly, enabling us to use $B$ for the said prediction, and update $B$ for the subsequent discrete-time predictions. Thus, the identification experiments conducted in Section 3.4.2 use a small value of $\Delta u$ for the piecewise linearisation to hold true.

### 2.7.3 Validation

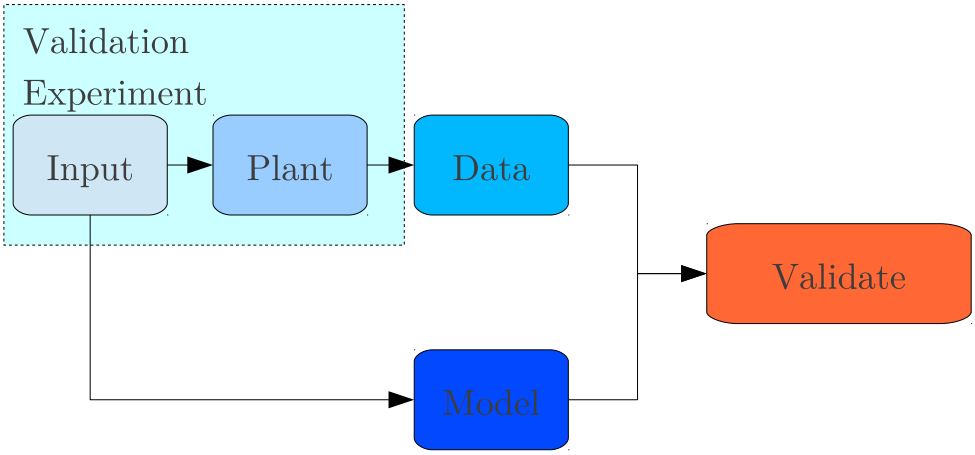


Figure 2.20: Schematic of model validation

Validation here refers to the process of demonstrating that the identified model is a reasonable representation of the actual system. Validity of results in a system identification study crucially depends upon the validity of the identified model. Even though it is an essential aspect of such studies, no single established definition of validation and model validity exists in the modelling literature [Bar96, PEB+00, SB06]. Model validation essentially is semi-formal and subjective, due to the relationship between the validity of the model and its "purpose".

In this thesis, specific experiments are conducted to record plant output for validation. These experiments are done separately from the identification experiments and quasi-static approximation is not assumed. The experimental set up was dismantled and reassembled between these experiments. Initially, the models are validated through eyeballing the predictions of the model output and experimental plant output for the same inputs (refer to Figure 2.20 and human intuition. Formally, standard deviation of $(\Delta Model - \Delta Plant)$ was analysed to validate the model.

## 2.8 Aerodynamic tests in a wind tunnel

Wind tunnels are used to study aerodynamic effects of air moving past solid objects. A typical wind tunnel consists of a tubular passage with the test object (aerofoil for this thesis) mounted in the middle. A powerful fan is usually employed to move the air inside the tunnel. Pre-determined wind conditions including turbulence level, 2-dimensionality,

stability of the flow etc. are created inside the tunnel. The aerodynamic effects are studied through various visualisation techniques and measurement of forces using various sensors.

For this thesis, two techniques of visualisation have been used – smoke visualisation and wool tuft visualisation. Smoke particles are injected into the wind tunnel, which follow the path of the air, thus highlighting streak-lines of the flow around the aerofoil. This allows the flow to be 'seen' and analysed. For the other technique, multiple wool tufts are stuck to the surface of the aerofoil. The wool tufts align to the direction of the flow, and thus show the streamlines on the aerofoil for attached flow. For separated flow, the tufts flutter in the air, and thus, separation can be easily visualised.

Such visualisation techniques, however, give only qualitative information. For quantitative information, the aerofoil, and the tunnel is typically instrumented with various sensors. In this thesis, surface pressure is measured over multiple points on the aerofoil, which is later integrated to calculate the lift force produced by the aerofoil. Drag calculation is done using wake survey method, which uses the measured air velocity deficit in wake of the aerofoil compared to the front of the aerofoil to calculate drag. The values of lift and drag (and thus, $C_L$ and $C_D$) thus obtained are used in simulations for small wind turbines. To be able to use these values for prototype applications, similitude and dimensionless analysis is carried out:

### 2.8.1 Similitude and dimensionless analysis

It is a usual practice to employ engineering models to study complex aerodynamic problems. More often than not, these models are smaller than the final prototype, as is the case in this thesis. For the results to hold for the prototype, the models tests are accompanied by a 'Similitude' analysis [Dha06, Szü80]. 'Similitude' is achieved by meeting the following criteria:

1. *Geometric Similitude*: The model should be an exact scale copy of the final prototype with the same surface roughness.

2. *Kinematic Similitude*: Fluid flow of both the model and the prototype must have similar time rates of change of motions, that is, fluid streamlines should be similar. In order to achieve this, the flow conditions for the model are kept similar to the prototype.

3. *Dynamic Similitude*: All forces in the model must be proportional to all forces in the prototype. To implement dynamic similitude, dimensionless analysis is used to express the system in terms of dimensionless parameters. These parameters are kept constant for both, the scale model and the prototype.

For this thesis, scaled model tests were conducted in wind tunnels. The results are eventually used in small wind turbine simulations. The similitude analysis is discussed further in Section 4.1.

## 2.9 Wind turbine simulators

Over the past years, various wind turbine simulators have been developed to investigate the dynamic behaviour, or to carry out design calculations. The simulators need to capture the structural dynamics as well as aerodynamic interaction of the blades with the wind. The typical inputs to wind turbine simulators are three-dimensional wind speed, aerodynamic and structural parameters of the blades and tower, electrical parameters of the generator and others. The generated output is typically a time series of power produced, mechanical loads, rotor speed, tower deformation and nacelle displacement and the like. The most popular turbine design software of today include FAST, FOCUS, GH Bladed, FLEX, ADCoS, MLS control Design Toolbox etc [JBJ05].

In this thesis, to predict the power output of a wind turbine in steady wind conditions, the numerical simulator Windsim [(DU05], developed by TU Delft has been used. WindSim models the most important aerodynamic (i.e. Blade Element Momentum, stall, aerodynamic damping) and dynamic features of modern wind turbines, so realistic simulations can be performed.

For the simulation of loads in this thesis, a suite of turbine design and performance prediction codes by National Wind Technology Centre (NWTC), collectively called as FAST (Fatigue, Aerodynamics, Structures, and Turbulence) Code is used. FAST is a comprehensive aero-elastic simulator, capable of predicting both the extreme and fatigue loads of two and three-bladed horizontal-axis wind turbines (HAWTs). FAST uses the unsteady BEM theory to model a turbine as a collection of rigid and flexible bodies in a spatio-temporal field of turbulent flow [JBJ05].

## 2.10 Turbine classification based on wind conditions

Wind is caused by differences in atmospheric pressure. When a difference in atmospheric pressure exists, air moves from the higher to the lower pressure area, resulting in winds of various speeds. Wind speed is measured by anemometers, most commonly using rotating cups or propellers. For higher frequency measurements, ultrasound signals or hot wire anemometers are used. Wind direction is usually expressed in terms of the direction from which it originates. Wind wanes and wind socks are used to indicate the direction of the wind. Sustained wind speeds in India are reported at a 10 meters height and are averaged over a 3 minute time frame [JAS07]. A wind rose (Figure 2.21(a)) is a graphic tool used by meteorologists to give a succinct view of how wind speed and direction are typically distributed at a particular location. The wind's speed constantly varies. In order to calculate the mean power delivered by a wind turbine, a probability density distribution of the wind speed is used. The Weibull distribution [PP02] is often a good approximation for the wind speed distribution. The Probability Density Function (PDF) of a Weibull distribution is:

$$P(x) = \frac{\alpha_w}{\beta_w} x^{\alpha-1} e^{-x^{\frac{\alpha}{\beta}}} \tag{2.33}$$

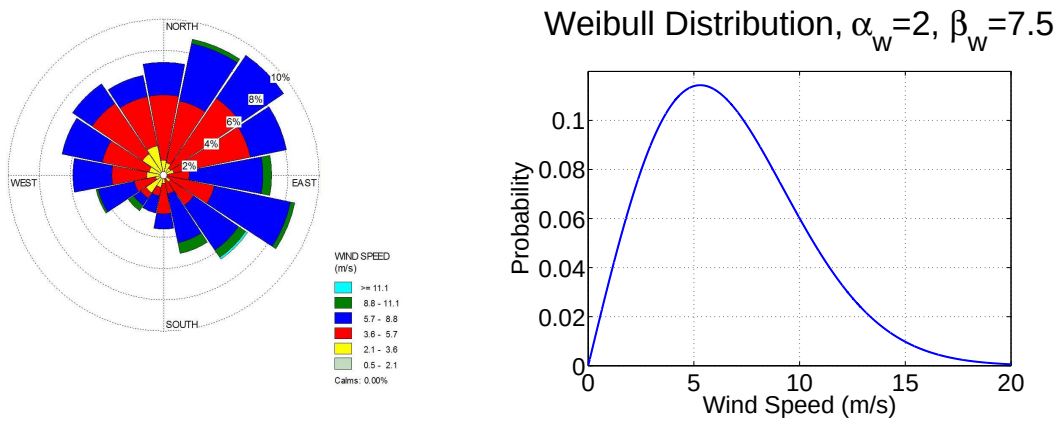


(a) Typical wind rose

(b) Weibull distribution (PDF) of wind speed

Figure 2.21: Representation of wind distribution

In fluid dynamics, turbulence or turbulent flow is a flow regime characterised by chaotic property changes [PK08]. This includes low momentum diffusion, high momentum convection, and rapid variation of pressure and velocity in space and time. Wind turbulence is the major contributor to the fatigue loading on wind turbines.

Table 2.1: Turbine classification based on wind conditions

| **Wind Class/Turbulence** | **Annual average wind speed at hub-height (m/s)** | **Extreme 50-year gust (m/s)** |
|---|---|---|
| **I A** High wind - Higher Turbulence 18% | 10 | 70 |
| **I B** High wind - Lower Turbulence 16% | 10 | 70 |
| **II A** Medium wind - Higher Turbulence 18% | 8.5 | 59.5 |
| **II B** Medium wind - Lower Turbulence 16% | 8.5 | 59.5 |
| **III A** Low wind - Higher Turbulence 18% | 7.5 | 52.5 |
| **III B** Low wind - Lower Turbulence 16% | 7.5 | 52.5 |
| **IV** | 6 | 42.0 |

For meteorological purposes, wind is classified on different scales, like Beaufort scale and Enhanced Fujita scale [Sau13]. For designing wind turbines against damage from hazards within the planned lifetime, the International Standards Organisation (ISO) classifies wind turbines according to wind conditions that the turbine can safely operate in. The IEC 61400 [Int08a] standards classes are determined by three parameters - the average wind speed, extreme 50-year gust, and turbulence, which are shown in Table 2.1. In this thesis, wind class IEC III A has been used.

## 2.11 Fatigue life and rain-flow count of stresses

Fatigue refers to the progressive and localised structural damage of a material subjected to cyclic loading [Lal99, Ari04]. Fatigue occurs when a material is subjected to repeated loading and unloading, even at stresses lesser than the ultimate tensile stress limit. In high cycle fatigue situations, material life time is characterised by an S-N (Stress and Number of cycles to failure) curve [Col93, DCFC09]. A typical S-N curve is shown in Figure 2.22.

Fatigue life is the number of cycles of a specific stress loading that a given material can sustain before failure occurs. It can be inferred from the figure, that higher amplitude stress cycles impact the fatigue life more significantly than the lower amplitude cycles. When plotted on a log-log scale, the S-N curve reduces to a straight line. The slope of the line, b, (after Basquin, who first proposed the law) is used to represent the relationship

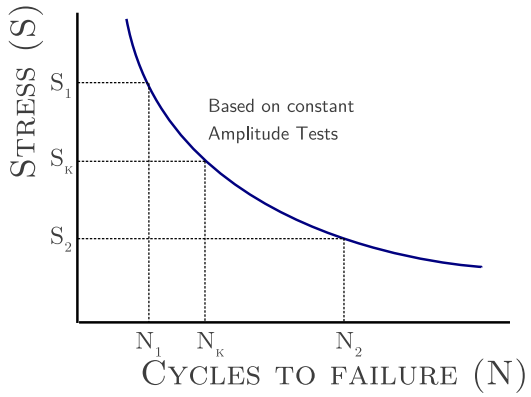


Figure 2.22: Constant amplitude S-N curve for a metal [Col93]

between S and N as:

$$N = \frac{S}{S_e}^{1/b} \times 10^6 \tag{2.34}$$

where $S_e$ is the endurance stress, under which, there is no failure for infinite (or, accepted as $10^7$) number of cycles and $N$ is the number of cycles to failure at stress level $S$.

Real life applications like wind turbine tower loading are usually not constant stress amplitude cycles. Thus, a method like the American Society for Testing and Materials (ASTM) rain-flow counting method [Sta05, Ari04] is used to reduce a spectrum of varying stresses into a set of simple stress reversals in order to assess the fatigue life, using S-N curves. Figure 2.23 shows the schematic of the conversion of stresses into rain-flow counts [WPO95].

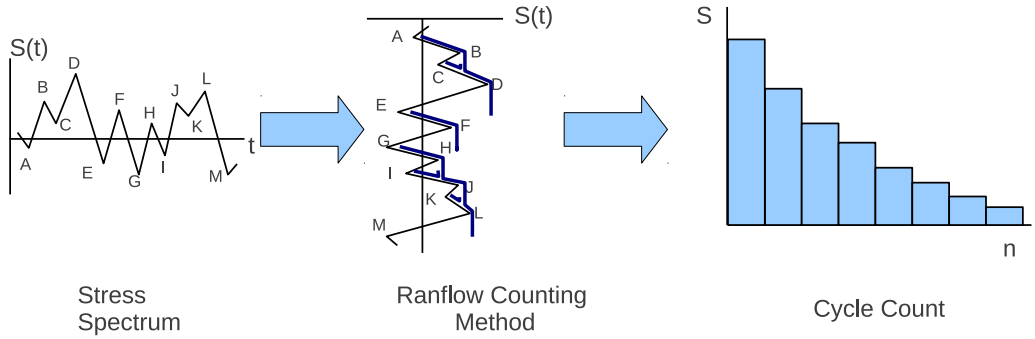


Figure 2.23: Schematic of rain-flow counting [WPO95]

Life span or material damage estimates are usually made using Palmgren-Miner rule along with a cycle counting procedure [Col93, Ari04, DCFC09]. The Palmgren-Miner

rule uses the S-N curve (Figure 2.22) to define 'Damage Fraction' at any stress level $S_i$ as the ratio of number of cycles of operation ($n_i$) to the total number of cycles ($N_i$) that produces failure at that stress level, that is,

$$D_i = \frac{n_i}{N_i} \tag{2.35}$$

The total damage, or 'Damage Equivalent' is defined as the sum of all the fractional damages. The event of failure occurs, if the damage equivalent exceeds unity:

$$D = \sum_{i=1}^{k} \frac{n_i}{N_i} \geq 1.0 \tag{2.36}$$

## 2.12 Prior work

This section gives an overview of the most relevant prior work and literature available in the fields worked on in this thesis, that is, low Reynolds number experiments, flow control at low Reynolds number flows, and flow control applications in wind turbines.

### 2.12.1 Low Reynolds number experiments

Owing to most of the applications in aerodynamics operating at higher $Re$ (primarily, aeroplanes at $> 10^7$), the contemporary aerofoil theory exists for higher $Re$. Low $Re$ flow theory and experiments have recently gained popularity because of interest in applications such as small wind turbines, Micro Air Vehicles (MAVs), Unmanned Air Vehicles (UAVs), and High Altitude Long Endurance (HALE). Principal investigations among these applications have been carried out by Mueller and group [MO87, Mue02, Mue00]. Specific work on NACA0012 aerofoil at low $Re$ has been carried out by Gregory and Oŕeilly [GO73], Kim et al. [KCC11], Sheldahl and Klimas [SP81], Laitone [Lai97] etc. However, such experiments are difficult to conduct, and reliability and repeat-ability of experiments are issues to be dealt with. Barlow et al., in their book [BRP99] discuss such issues and set guidelines for setting up of experiments at low $Re$. Yarusevych and Boutilier have investigated the effect of end-plates and blockage on low Reynolds number flows in [YB12]. Neatby and Yarusevych have suggested improvements in experimental set-up for reliable drag measurements on aerofoils at low $Re$ in [NY12].

Low $Re$ experimentation, is thus, a still-evolving field, with no standardised set-up and testing techniques available which can be followed. Further, there is a general lack of usable engineering data for various aerofoil profiles at low $Re$. The predictions of popular aerofoil software, like Xfoil, too are not validated for such $Re$. Thus, to obtain reliable data on steady-state $C_L$ and $C_D$ data for this thesis, specific low $Re$ experiments were set up, as described in Sections 3.2.1 – 3.2.7.

### 2.12.2 Flow control at high and low Reynolds numbers

Active flow control has been an area of interest for applications in flight-dynamics, with earliest known experimental work dating from late 1930s [Bra99]. Braslow presents a historic overview of flow control through suction in [Bra99]. Collisa et al. have reviewed the theoretical and practical issues in active flow control theory in [CJST04]. Gad-el-Haq's book on flow control [GeH07] discusses in detail the active, passive and reactive methods utilised for flow control. These two sources form a good reference for understanding the state of the art in active flow control.

Washburn et al. present a snapshot of active flow control programs at NASA's Langley research centre in [WGA02]. It is stressed that active flow control technologies need maturing to the point that their benefits and functionality can correctly be assessed. Kibens and Bower [KB04] discuss the active flow control research for applications at the Boeing company. Boeing has focused on active flow control for more than two decades and are developing applications for both - transport and combat aircrafts. Shmilovish and Yadlin [SY11] and Stanewsky [Sta01] present cases for flow control, including surface suction for transport and combat aircraft at Boeing and NASA, respectively. These studies demonstrate an interest in flow-control based application. However, such flight-dynamics based studies on flow control concentrate on $Re$ orders of magnitude higher ($10^7$ and above) than small wind turbine $Re$ ($10^4$ - $10^5$).

For understanding surface-suction based flow-control, the method applied in this thesis, Gad-el-haq [GeH07] and Eppler [Epp99] form a comprehensive theoretical base. Braslow, in [Bra99] as discussed earlier, provides a historic perspective on suction-based flow control, albeit at higher $Re$. Greenblatt et al. in [GPY+06] and [GPCSH06] conducted experiments to study fluid dynamics of separation control through surface suction as well as zero-net-mass oscillatory blowing, and collect data to validate computational

fluid dynamic simulations. These experiments were carried out for a non-aerofoil profile mould in wind tunnel, and at $Re = 9.29 \times 10^5$, which is slightly higher than the $Re$ numbers in this thesis.

Mouyon et al. have studied feedback control of boundary layer transition on a flat plate from laminar to turbulent using suction as control input [MCSP98]. The flow speeds are higher than the experiments in this thesis, and the flat plate is assumed to be of infinite length, thus, the characteristic $Re$ range for this paper is higher, as well as the geometry is not relevant to that considered in this thesis . However, this paper discusses the system-dynamic of flow control, which is an integral part of the thesis, and the values of time-constant of the system identified matches with that in this paper.

There are a number of numerical studies on surface suction based flow control. Thus, some specific literature on aerofoils is available. Huang et al. present numerical results of suction and blowing over NACA0012 aerofoil at $Re = 10^5$ [HHLH04]. The $Re$ and aerofoil profile are relevant to the experiments in this thesis, but Huang et al. [HHLH04] conducted simulations only at angle of attack 18°. Wind turbines require aerofoil data over a larger range – in this thesis, non-flow-control aerofoil data is taken from −180° to 180° and flow-control aerofoil data from 0° to 45°. Such range of data is difficult to find in the literature.

Shojaefard et al. simulated suction and injection based flow control on sub-sonic aerofoils [SNAG05]. They discuss the effect of flow control on $C_L$ and $C_D$ at $Re > 10^7$. Liu et al. also present numerical results for suction and blowing at higher $Re$ ($3.4 \times 10^6$ and $5.9 \times 10^6$ on RAE2882 aerofoil [LDCH10]. Results from such studies cannot be used directly for small wind turbine applications because of orders of magnitude difference in the operating $Re$ range of small turbines.

Apart from surface suction, zero-net-mass-flow, or synthetic jets are a popular method of achieving flow control. Ekaterinaris [Eka04], Tuck et al. [TS+04], Williams et al [WTC+09], Zhang and Zhong [ZZ10], Taira et al. [TRCW10] have researched on synthetic jets for enhancing aerofoil performance. Other methods include use of pop-up feathers [Sch09], constant blowing [Chu10], hydrophillic surfaces [FMG+08] and MEMS actuators [PPM+10] etc.

The literature is abundant with flow control for high $Re$ applications. Multiple techniques like suction, blowing, synthetic jets, vortex generators etc. have been researched

on, for controlling boundary layer, managing vortices, maintaining laminar flow, among other control objectives. Thus, there is a prima-facie case for exploring flow control for low $Re$ applications like small wind turbines.

The availability of literature at low Re, however, is sparse. Further, as seen above, majority of these studies focus on using numerical simulations to understand the fluid dynamics aspect of flow control. Consequently, quantified engineering values, that is, effect of suction-based flow-control on $C_L$ and $C_D$ at low $Re$, obtained through validated experiments, are hard to come by in literature.

The system-dynamic perspective of flow control, is largely missing in these studies. This has also been noted by Washburn's study on NASA Langley's flow control program in [WGA02]. To apply suction-based flow-control using wind turbine simulators, a dynamic model of suction is needed. In the papers mentioned above, Mouyon et al. [MCSP98] and Williams et al. [WTC+09] present temporal response of output to flow-control input, but do not identify the associated dynamics with the temporal response. The author came across only one instance of experimental system identification of fluid-dynamics based system in the literature, which is similar to the methodology applied in this thesis. In [Wey01], Weyer identified the system-dynamics associated with an water irrigation channel. Though the methodology is similar, the application, geometry and $Re$ are vastly different from the experiments in this thesis.

Thus, there appears to be a dearth of validated experimental data involving the use of active flow control that may be used for designs relating to low Reynolds number applications, including small wind turbines. The experimental part of this thesis (Chapter 3) aims to address this lack, specifically:

- Steady-state effect of suction-based flow control on $C_L$ and $C_D$
- System-dynamic, or temporal aspect of suction-based flow control

### 2.12.3 Utilisation of flow control in wind turbines

Wind turbine control is a rapidly growing discipline. With the increase in the size of turbines, more complex control algorithms are needed. The focus of most of these algorithms is two-fold: i) maximise power through generator torque control, below rated wind speed, and ii) maintain loads within design limit, above rated wind speed. A good amount of

information about these techniques can be found in Burton et al. [BSJB01], Bianchi et al. [BDBM06] and Write and Fingersh [WF08].

Review papers by Laks et al. [LPW09], Musunuri and Ginn [MG11] and Abdullah et al. [AYTS12] provide an updated overview of control algorithms for Maximum Power Point Tracking (MPPT). Write and Fingersh, [WF08] and Suryanarayanan and Dixit [SD05] discuss Multiple Input Multiple Output (MIMO) algorithms. These MIMO algorithms aim to achieve multiple control objectives, like fatigue reduction along with maximising output. The most popular actuation technique used for fatigue mitigation is collective and individual pitching of blades, and multiple studies can be found in literature: [Bos05, GC08, LPW09, DPW+10, DPW+11]. These studies are usually conducted for large wind turbines.

The available literature on utilisation of flow control for applications in large as well as small wind turbines is, however, limited. Technical report by Johnson et al. [JVDB08] from Sandia National Laboratories discusses multiple techniques of flow control and how they can be potentially used in wind turbines. The report concentrates on reviewing the available flow-control techniques through published papers, and proposing potential use in wind turbine applications. Experimentation or numerical simulations, however, were not carried out to establish quantitative benefits of using flow-control in wind turbine applications.

Such quantification has been done by Greenblat et al. in [Gre10, GSBH12, GBHMV14] using plasma actuators, and Sasson and Greenblatt in [SG11] using slot blowing. These studies have been conducted for increase in power capture for large, Vertical Axis Wind Turbines (VAWT), whose aerodynamics are significantly different from small, Horizontal Axis Wind Turbines (HAWT) analysed in this thesis.

The quantification of benefits of the use of active flow-control techniques, specifically, surface suction based techniques for small wind turbines, is thus, largely unexplored. A small amount of literature is available for increase in power capture through flow-control for large wind turbines, though they employ flow-control techniques other than surface suction. There seems to be no instance of literature for mitigation of loads using active flow-control. Chapter 4 addresses these gaps by providing a quantitative study on increase in power capture as well as mitigation of fatigue loads using active flow-control through surface suction for small, horizontal axis wind turbines.

# Chapter 3

# Low Reynolds number experiments

## 3.1 Introduction

This chapter describes flow control experiments conducted at low $Re$. The experiments were set up to investigate the effectiveness and dynamics of flow control by suction. The quantitative results from these experiments were used in simulations in Chapter 4 to determine the benefits achievable when surface-suction based flow-control is applied to small wind turbines. The set-up parameters were designed to correspond to the relevant $Re$ regimes for these turbines. The objective of the tests was to obtain:

i time averaged values of change in lift drag and stall angle on application of suction, which are calculated based on the coefficient of pressure, $C_{pressure}$

ii time averaged variation of $C_{pressure}$ with change in suction, that is, change in the suction momentum coefficient, $C_{\mu}$

iii temporal change in $C_{pressure}$ for a step change in $C_{\mu}$

Two types of tests were conducted on the set-up – steady state, to obtain time averaged outputs, and dynamic, to record the temporal change in pressures caused by applying suction. The results from the steady state tests were used to estimate the possible increase in the power output of pseudo-static small wind turbine rotors by applying a surface suction technique over the blades. The dynamic results were used to obtain the map of dynamics between application of suction and change in pressures over aerofoils. This dynamic map is required to devise a control strategy to realise surface suction in

Table 3.1: Reynolds numbers for the experiments

| Wind Tunnel | Power | Cross Section | Wind Speeds | Reynolds Numbers |
|---|---|---|---|---|
| **IIT Bombay** | $220kW$ | $0.6m \times 1m$ | $2.0\ m/s$ | $3.3 \times 10^4$ |
| | | | $2.5\ m/s$ | $4.1 \times 10^4$ |
| | | | $3.0\ m/s$ | $4.9 \times 10^4$ |
| | | | $3.5\ m/s$ | $5.7 \times 10^4$ |
| **Monash University** | $450kW$ | $2m \times 2m$ | $5.0\ m/s$ | $8.2 \times 10^4$ |
| | | | $10.0\ m/s$ | $1.6 \times 10^5$ |
| | | | $20.0\ m/s$ | $3.3 \times 10^5$ |
| | | | $30.0\ m/s$ | $4.9 \times 10^5$ |

wind turbines which operate in variable wind conditions (which are closer to reality than pseudo-static simulations).

## 3.2 Experimental set-up

The first part of this section describes how the relevant $Re$ regime was obtained. The next part describes the choice of aerofoil profiles and their fabrication. It is followed by details of the suction mechanism, instrumentation, wind tunnels and the measures taken to ensure two-dimensionality of flow over the aerofoils. The set-up is common for the steady state and dynamic tests.

### 3.2.1 Reynolds number regime

Small and medium wind turbines typically operate in $Re$ in the range $10^4$ to $10^5$ [Woo11, WW04]. Wind tunnel experiments were designed to correspond to these $Re$. Preliminary experiments were conducted at the 220kW open circuit wind tunnel at IIT Bombay and final experiments were conducted at the $450kW$ closed circuit wind tunnel at the Monash University. The tunnel at IIT Bombay is capable of producing wind speeds from $2m/s$ to $20m/s$, whereas the wind tunnel at Monash has speeds from $5m/s$ to $30m/s$. To keep the Reynolds numbers in the relevant regime, the chord length of the aerofoil specimens was kept at $250mm$. The wind speeds and corresponding chord-based Reynolds numbers are given in Table 3.1.

### 3.2.2 Aerofoils

#### Aerofoil profile selection and dimensions

Two aerofoil profiles were chosen. A symmetrical aerofoil profile, NACA0012 was chosen for its ease of construction and abundant availability of data in literature to validate results. A low-speed, wind turbine-specific aerofoil, S814 was chosen to obtain relevant data for wind turbines. The chord length for both aerofoil profiles was $c = 250mm$. The span of the aerofoils was $b = 200mm$. A $2mm \times 180mm$ span-wise slit was provided on the upper surface of the aerofoil. A wide slit, along with a smaller span, was chosen to avoid possible three-dimensional flow effects rising from the suction through the slit.

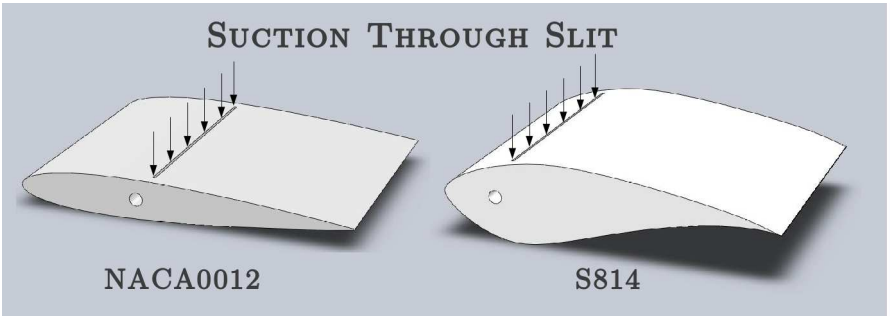


Figure 3.1: Aerofoil profiles showing suction through the slits

#### Aerofoil fabrication

Vacuum forming technique was used to fabricate the aerofoils. A teak-wood mould matching the upper-half and lower-half profile of the aerofoils was made. The dimensions of the mould were set at $248mm$ for the chord length and $198mm$ for span. Since NACA0012 is symmetrical, only one wooden mould was needed. A $1mm$ thick High-Impact-Polystyrene (HIP) sheet was heated to a forming temperature, stretched onto the wooden mould, and held against the mould by the application of vacuum between the mould surface and the sheet, which was then slowly cooled. This set one half of the aerofoil section with the appropriate dimensions. The two halves obtained by this method were pasted together to get a basic aerofoil section, which was later provided for suction and instrumentation.

### Surface suction over aerofoil

Slits of $2mm \times 180mm$ were created on the suction surface of the aerofoils at varying distances from the leading edge. A wide slit was chosen to avoid three-dimensional flow effects, and to be as close as possible to a two-dimensional flow. In the preliminary tests at the IIT Bombay wind tunnel, multiple slit positions were tested for each of the aerofoil profiles, from which the most optimal positions, were selected for each of the aerofoil profiles, based on the increase in $C_L$ in the operating range of wind turbines. These slit positions were used in the final tests at the Monash University wind tunnel.

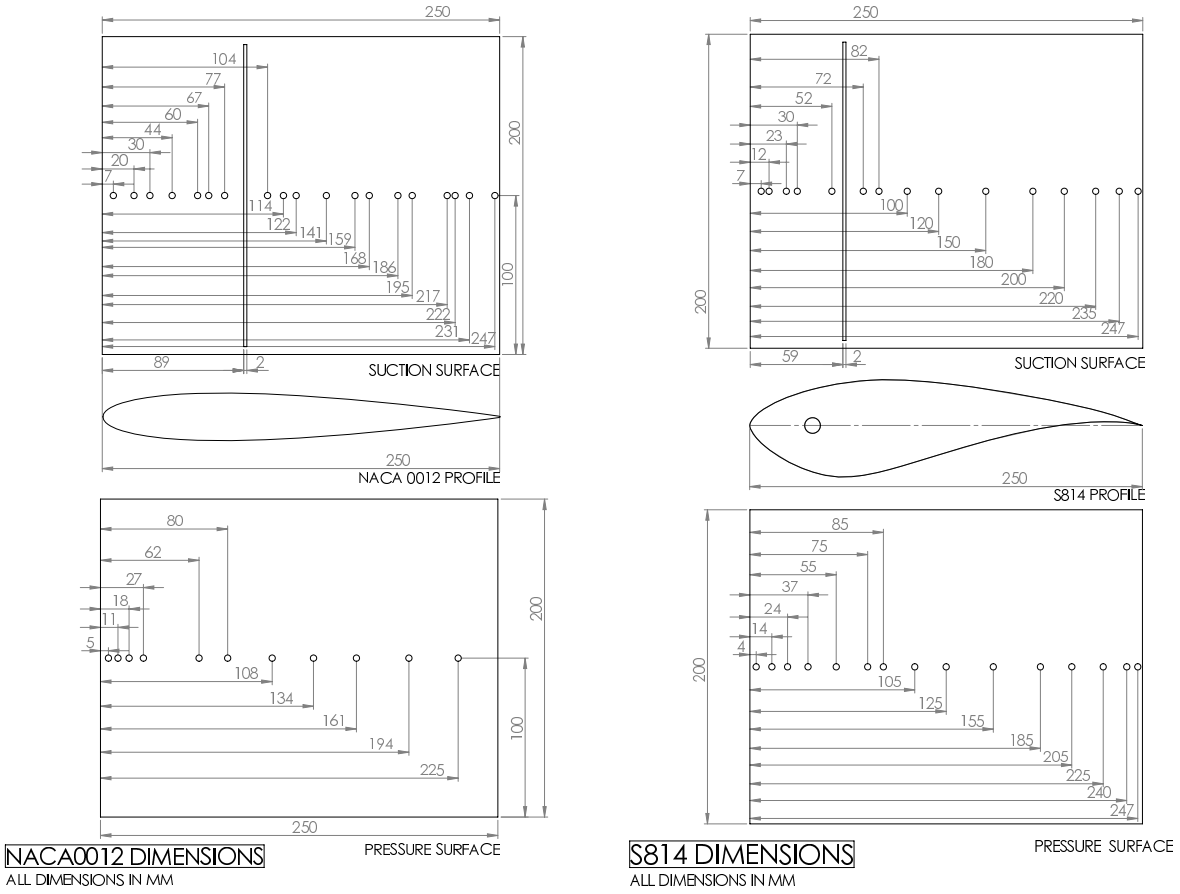


(a) NACA0012 (b) S814

Figure 3.2: Aerofoil profiles showing dimensions and positions of suction slits and pressure taps

For the NACA0012 aerofoil profile, slit positions $x/c = 0.16$, $x/c = 0.36$ and $x/c = 0.56$ from the leading edge were tested. The slit closest to the leading edge ($x/c = 0.16$) provided maximum change in $C_L$ at higher angles of attack and insignificant change in $C_L$ at low angles of attack. The slit closest to the trailing edge provided maximum benefit

at low angles of attack, and very less benefit close to the stall angle. The optimum and maximum benefit was seen for the centre slit, that is, when the slit was at $x/c = 0.36$ from the leading edge.

The slit positions tested for S814 were at $x/c = 0.12$, $x/c = 0.24$, $x/c = 0.44$ and $x/c = 0.64$ from the leading edge. The S814 profile has a thicker leading edge, which allowed the suction mechanism to be housed closer to the leading edge. The most beneficial slit position, by the same criterion of increase in $C_L$, was at $x/c = 0.24$ . The reason why a smaller $x/c$ ratio works better in the case of the S814 aerofoil may be the fact that the S814 aerofoil has a thicker root and a greater camber which in turn lead to a greater propensity for flow separation to occur at smaller $x/c$ ratios, which can be better controlled by a slit position closer to the leading edge as compared to the NACA0012 aerofoil.

Figure 3.2 shows NACA0012 aerofoil profile with the suction slit at $0.36c$ and S814 aerofoil profile with the suction slit at $0.24c$. A $20mm$ diameter PVC pipe was glued under the slit, using a cyano-acrylite based adhesive. A slit of the same dimensions was cut in the pipe just under the slit in the aerofoil. Both ends of this pipe were connected to a vacuum pump using standard hoses and joints. A vacuum cleaner was used as a suction pump, as described in 3.2.4

### Taps for pressure measurement

The surface pressure was measured using pressure taps on the surface of the aerofoil. Multiple taps of $2mm$ diameter were provided on the top and bottom surfaces to measure pressure across the chord length of the aerofoil. These taps were in the span-wise centre of the aerofoil. The location of the pressure taps are detailed in Table 3.2. A higher concentration of pressure taps was placed near the leading edge where the pressure gradient is typically large. The NACA0012 aerofoil was provided with more taps on the suction surface, to study the effect of suction relative to the distance from the suction slit. The S814 aerofoil has a complex pressure surface, hence both suction surface as well as pressure surface had same number of taps.

Table 3.2: Pressure tap positions on aerofoil surfaces

| **Aerofoil Profile** | Tap positions from leading edge | |
|---|---|---|
| | Suction surface | Pressure surface |
| **NACA0012** | $7mm$, $20mm$, $31mm$, $44mm$, $60mm$, $67mm$, $77mm$, $104mm$, $114mm$, $122mm$, $141mm$, $159mm$, $168mm$, $186mm$, $195mm$, $217mm$, $222mm$, $231mm$, $247mm$ | $5mm$, $11mm$, $18mm$, $27mm$, $62mm$, $80mm$, $108mm$, $134mm$, $161mm$, $194mm$ , $225mm$ |
| **S814** | $7mm$, $12mm$, $23mm$, $30mm$, $52mm$, $72mm$, $82mm$, $100mm$, $120mm$, $150mm$, $180mm$, $200mm$, $220mm$, $235mm$, $247mm$ | $4mm$, $14mm$, $24mm$, $37mm$, $55mm$, $75mm$, $85mm$, $105mm$, $125mm$, $155mm$, $185mm$, $205mm$, $225mm$, $240mm$, $247mm$ |

### 3.2.3 End-plates for two-dimensionality of flow

Since the span of the aerofoil was lesser than the chord of the aerofoil, the flow over the centre of the aerofoil was susceptible to three-dimensional flow affects by the vortices created by the edges. To minimise the effect of the tip vortices, and to ensure two-dimensionality of the flow over the surface, end-plates were mounted on the sides of the aerofoils [Sta74, YB12]. Preliminary tests at IIT Bombay were conducted without end-plates. Preliminary tests at Monash University were conducted with and without end-plates. The final tests at Monash University were conducted with end plates. Figures 3.3 and 3.4 show the set-up at the Monash University $450kW$ tunnel. The aerofoil was mounted at the "centre" – consequently, the leading edge was at a distance of $2c$ downstream from the start of the end plates. The end-plates and the aerofoils were held in place by a steel structure. All parts of the steel structure were downstream of the end plates and the aerofoils such that the flow over the aerofoil was not disturbed.

The end-plates induce boundary layer over their surface, which may affect the flow over the aerofoil. The boundary layer thickness was estimated using Blasius solution for the working wind speeds. The boundary layer thickness at the leading edge of the aerofoil

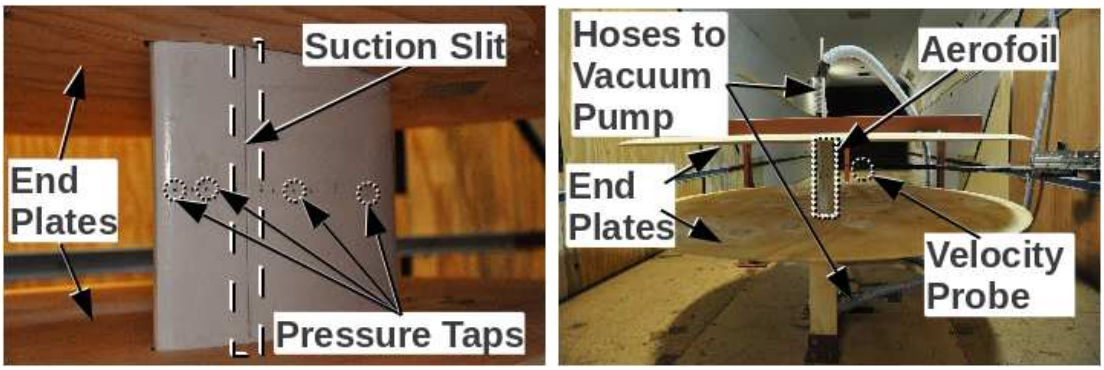


(a) Close up of S814 in experimental set-up (b) Complete set-up in wind tunnel

Figure 3.3: Aerofoil test set-up inside wind tunnel

was estimated to lie between $5.9mm$ for wind speed $5m/s$ and $2.4mm$ for wind speed $30m/s$. The pressure taps were at the centre of the aerofoil, that is, at a distance of $100mm$ from the end plates. This distance is large enough for the boundary layer to have a significant effect on the pressure measurements, thus, a two-dimensional flow over the aerofoils was assumed.

Figures 3.5 and 3.6 highlight the effects of using end plates. At lower angles of attack, as shown in figure 3.5, the trends of surface pressure for experiments with, and without end plates are similar. At low speeds and low angles of attack, the pressures remained close to each other, indicating that edge effects do not affect the pressures significantly at the centre of the aerofoil. At higher angles of attack, however, the trends varied significantly for the two cases. In figure 3.6, for high angle of attack, the flow separated and the aerofoil stalled for both, low wind speed, as well as high wind speed with end-plates. Without the end-plates, however, the aerofoils do no stall at high angles of attack. Edge effects seem to energise the boundary layer, which helped to avoid flow separation, and hence, stall. Since the use of end-plates believed to have achieved a more reliable two-dimensional flow over the aerofoils, only the end-plate experiments' data is used for simulations in Chapter 4.

### 3.2.4 Suction pumps

A venturi-principle based vacuum generator was used in the preliminary tests to generate suction pressure. However, both, the suction pressure and the rate of suction with this pump were insufficient. An oil-based vacuum generator was tried next, which pro-

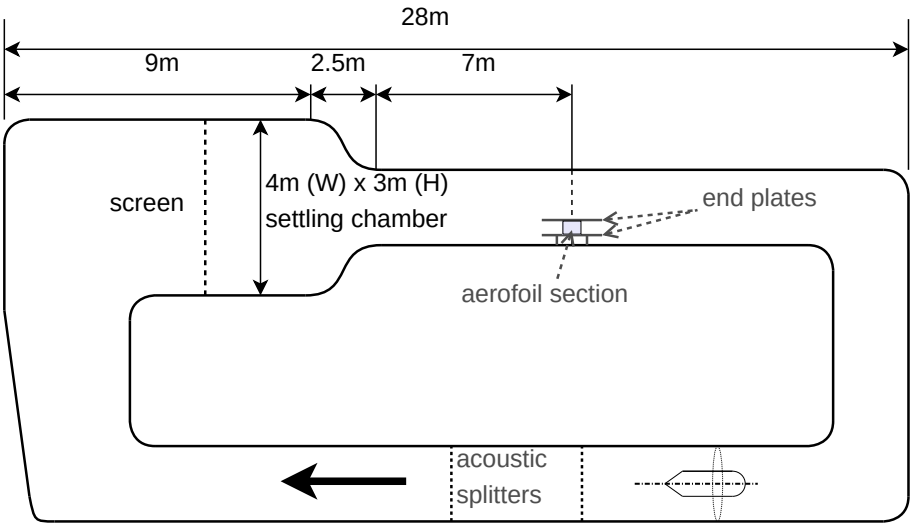


(a) Placement of the set-up in wind tunnel

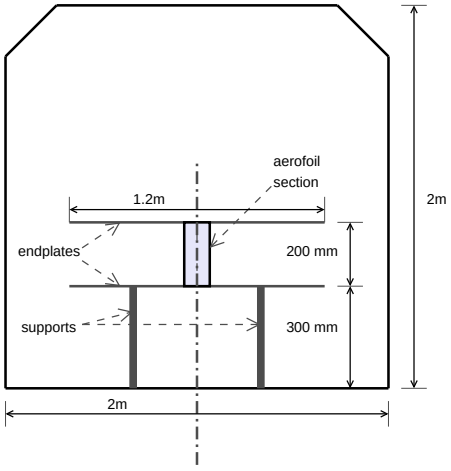


(b) Front view of the set-up

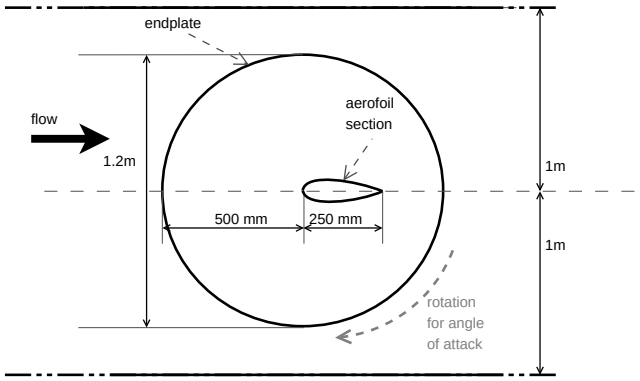


(c) Top view of the set-up

Figure 3.4: Schematic of the test set-up inside Monash $450kW$ tunnel

vided good suction pressure. However, the rate of suction still remained insufficient. A consumer, off-the-shelf vacuum cleaner was able to provide satisfactory suction pressures and suction rates. For the experiments at IIT Bombay, the free stream velocity was low ($2m/s$-$4m/s$), hence, a $600W$ vacuum cleaner proved capable of providing relevant suction effort (see Section 3.2.7). For the experiments conducted at the Monash University, the wind speed was higher($5m/s$-$30m/s$). To maintain meaningful suction efforts a more powerful, $2400W$ vacuum cleaner was used.

The suction rate was varied using a valve as shown in figure 3.7. A venturi tube was provided between the valve and the aerofoil to measure the flow rate. The venturi was connected to the aerofoils from two ends using flexible hoses. The connections were

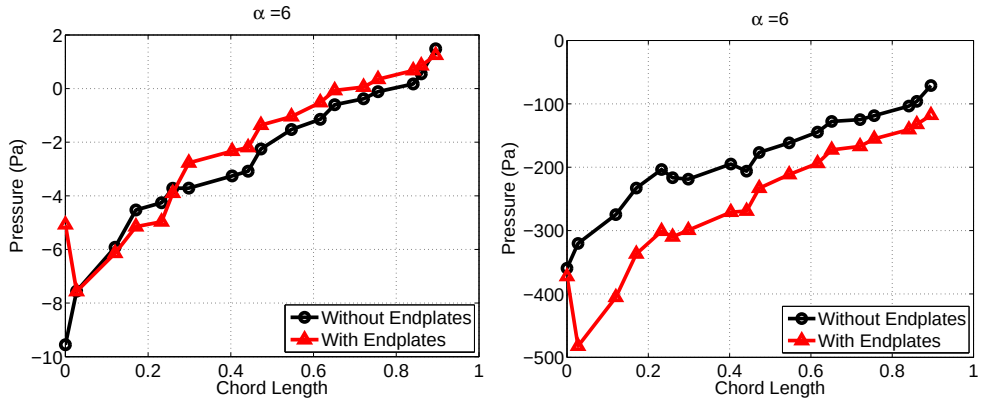


(a) $Re = 8.2 \times 10^4$, $\alpha = 6°$ (b) $Re = 3.3 \times 10^5$, $\alpha = 6°$

Figure 3.5: Surface pressures with and without end-plates for low $\alpha$ for NACA0012 aerofoil profile

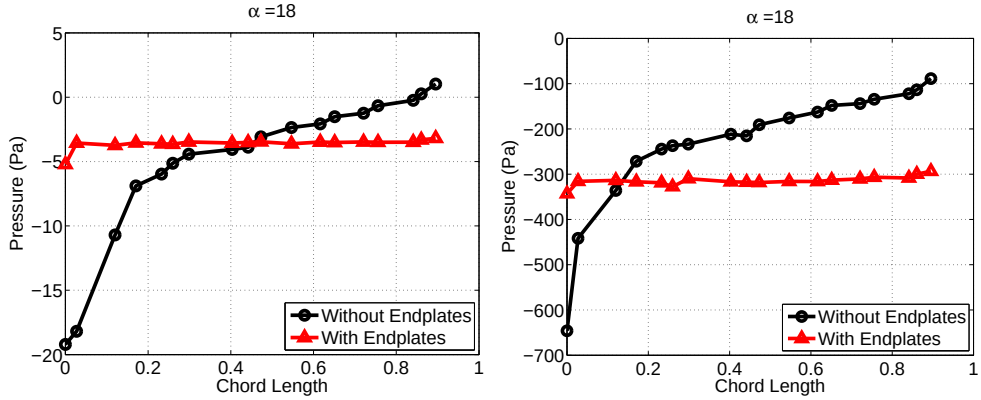


(a) $Re = 8.2 \times 10^4$, $\alpha = 18°$ (b) $Re = 3.3 \times 10^5$, $\alpha = 18°$

Figure 3.6: Surface pressures with and without end-plates for high $\alpha$ for NACA0012 aerofoil profile

provided on both sides of the aerofoils to maintain a uniform flow in the slit.

### 3.2.5 Instrumentation

#### Aerofoil surface pressures

The $2mm$ diameter pressure taps over the surface of the aerofoils (see Section 3.2.2) were connected to pressure transducers using $1.1m$ long silicon tubes. The internal diameter of these tubes was $1mm$.

At IIT Bombay, $3 \times 16$-channel micro-manometers (Scanivalve Digital Sensor Array, DSA 3217) was used to record pressures at $500Hz$. The pressure values for a single tap obtained were averaged over a time period of $30s$ to obtain a mean pressure reading for

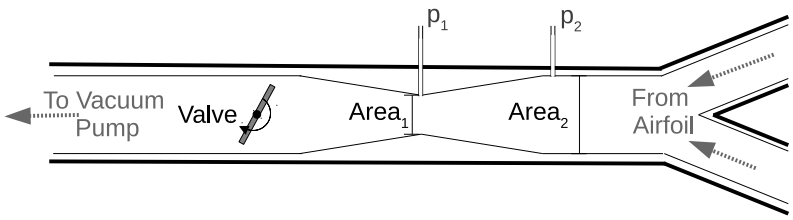


Figure 3.7: Suction Schematic

that particular tap. For Scanivalve DSA3217, the manufacturer specifies a $\pm 0.05\%$ full scale accuracy. These instruments were calibrated against an FCO510 micro-manometer with resolution down to $0.001Pa$.

At Monash University, a 64-channel Turbulent Flow Instrumentation Dynamic Pressure Measurement System (DPMS) was used to measure surface pressures. The sampling frequency was kept at $500Hz$ to calculate mean pressures measured over $30s$. In addition to steady state tests, dynamic tests were conducted at this wind tunnel. For dynamic analysis, the pressures were sampled at a frequency of $1000Hz$. For DPMS, the manufacturer specifies a $\pm 0.3\%$ full scale accuracy.

The error in time averaged pressure values is shown in Figure 3.8 for pre-stall($12°$) and post-stall ($18°$) angles of attack for the NACA0012 aerofoil at Reynolds number $1.6 \times 10^5$. The observed trend is that the errors remained between $1.5Pa$ and $8Pa$, except for angle of attack close to the stall angle. When stall is about to occur, the flow attaches and detaches periodically, varying the pressure to a larger extent. Hence, the errors around the mean are larger, ranging from $15Pa$ to $25Pa$ as shown in Figure 3.8(b) for the suction-on case. At $18°$, stall has occurred without suction, thus, the errors are comparable those at the pre-stall angles.

### Pressures in the wake

A Turbulent Flow Instrumentation Cobra Probe was used to measure the velocities $x/c = 1$ behind the aerofoil. The Cobra Probe incorporates four 0.5 mm pressure taps in a multi-faceted head which can resolve three component velocities and static pressure measurement within a $\pm 45°$ acceptance cone. The manufacturer-specified accuracy of the probe is $\pm 0.3m/s$ for velocity.

The measurement positions were in the span-wise centre of the aerofoil and ranged from $0.32c$ on the suction side to $0.56c$ on the pressure side. The velocities were sampled

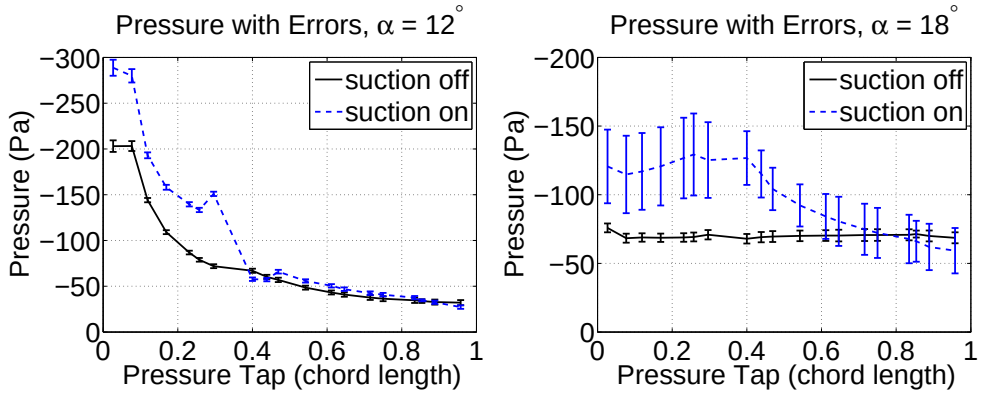


(a) Pre-stall errors

(b) Post-stall errors

Figure 3.8: Errors in surface pressure measurement at $Re = 1.6 \times 10^5$

at $1000Hz$ and time averaged for a period of $30s$. Since the measurements for the surface pressures over the aerofoil and the velocities wake were done in the centre section of the aerofoil, which remained significantly away from the boundary layer over the end plate, the measured coefficients of lift and drag should be representative of a two-dimensional section.

### Free stream velocity

At IIT Bombay, an upstream pitot tube was connected to the FCO510 micro-manometer, which used the static and stagnation pressures to calculate and display the free stream velocity in $m/s$. The accuracy of the speed display was $\pm 0.01m/s$. To conduct the experiments, the free stream velocity was kept within $\pm 0.1m/s$ of the desired velocity.

At the Monash University, the static and stagnation pressures for a similar upstream pitot tube were recorded by the DPMS. These values were used to calculate free stream velocities for each sample, as detailed in 3.2.7.

### Data acquisition

The pressure transducers DSA and DPMS were connected to a computer through the intranet and USB, respectively. The computer communicated with the transducers and collected data for each of the sample cases and stored the data in the CSV format. The CSV files were imported into MATLAB for analysis, as explained in Section 3.2.7.

### 3.2.6 Wind tunnel

Preliminary experiments were carried out in the wind tunnel located in the Aircraft Propulsion Laboratory at IIT Bombay. It is a low-speed, open-circuit wind tunnel of the suction type. It incorporates an air inlet, cross-section settling chamber fitted with a honeycomb structure and meshes, and a 10:1 contraction. The test section is $0.6m \times 1m$. It can create uniform steady flows with free stream velocities $U_\infty = 1.6m/s$ and higher. A 12 blade axial fan, located at the end of the diffuser, is driven by a $220kW$ variable-speed motor. The blade speed was controlled with a PID controller for the motor. Figure 3.9(a) shows the wind tunnel at IIT Bombay. Figure 3.10 shows the schemaatic of the tunnel.

The learnings from the IIT Bombay wind tunnel experiments were used to select the set-up parameters for the final tests at the Monash University Wind Tunnel. It is a recirculating, closed-circuit–type wind tunnel. The test section is $2m \times 2m$. The axial flow fan is powered by a 450kW constant speed motor. To vary the wind speed, the pitch of the fan blades was varied. Figure 3.9(b) shows the wind tunnel test section at the Monash University. Figure 3.4 shows the schematic of the wind tunnel.

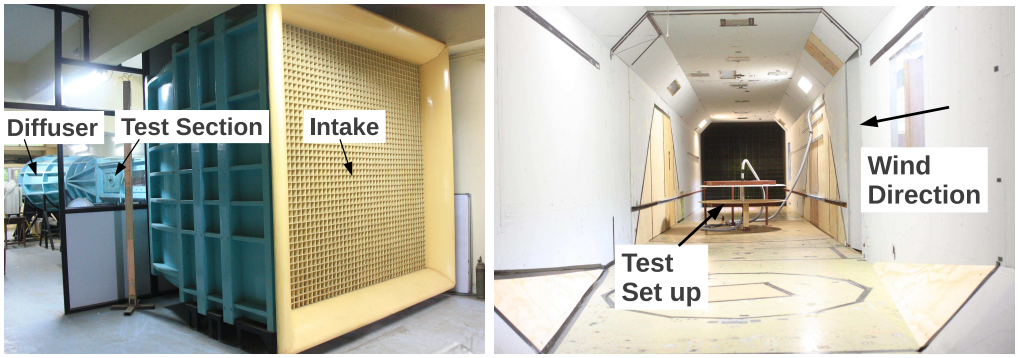


(a) Wind Tunnel at IIT Bombay (b) Wind Tunnel at Monash University

Figure 3.9: Wind Tunnels

The dynamic and static pressures inside the wind tunnel at the Monash University were measured using a Pitot tube in the tunnel connected to the same DPMS transducers as the pressure taps. The calibration of wind speed and turbulence intensity was done using a Cobra Probe at 10 span-wise locations $0.5c$ upstream of the leading edge and parallel to the centre section of the aerofoil. During calibration, both the Cobra probe and the pitot tube in the wind tunnel were used to obtain mean velocities inside the end plates and in the wind tunnel, respectively. During active tests, the Cobra probe was removed

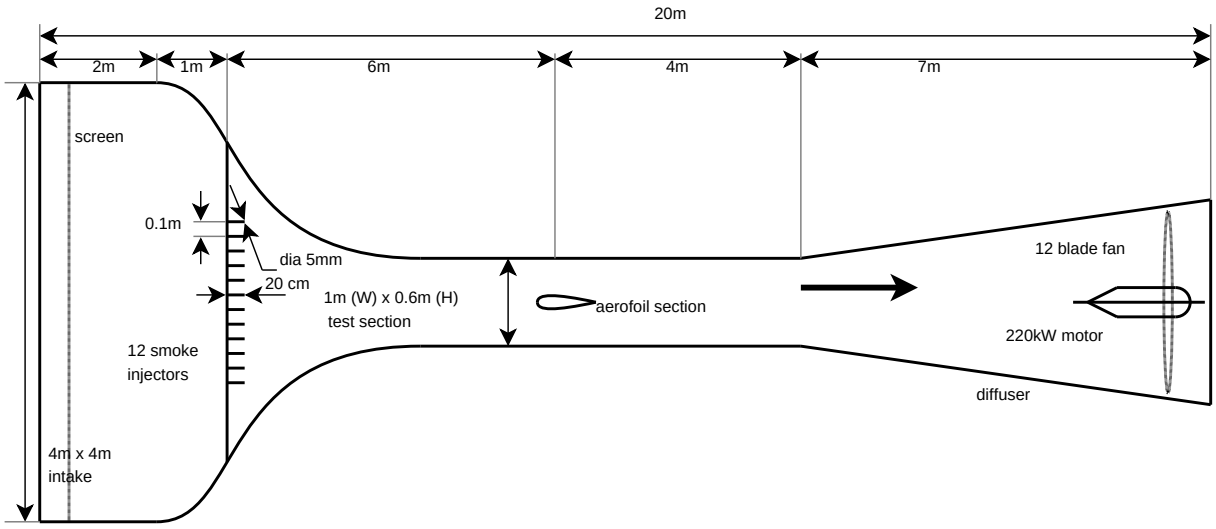


Figure 3.10: $220kW$ wind tunnel at IIT Bombay

and pitot tube readings were used. These time-averaged velocities and turbulence levels were sampled for $30s$ at a sampling rate of $1000Hz$. The turbulence intensities between the end plates for wind speeds of $5m/s$, $10m/s$, $20m/s$ and $30m/s$, respectively, were recorded as 6.5%, 1.4%, 1.3% and 1.1%. For the set-up, the estimated the solid-blockage ratios including end-plate blockage [BRP99] ranged from 0.0135 to 0.0213 for angles of attack $0° - 45°$. The estimated errors for Reynolds numbers for these blockage ratio were less than 4%.

### Yaw

In the $220kW$ wind tunnel at IIT Bombay, the aerofoils were mounted horizontally on a rod that ran span-wise through the aerofoil. The rod was held in position on two bushes on the side wall. the angle of attack of the aerofoil was changed by rotating the bushes. The aerofoil was mounted at an angle of attack = $0°$ using a spirit level. The bushes could be adjusted to be within $\pm 0.5°$ of the desired angle.

In the $450kW$ wind tunnel at the Monash University, the aerofoil was mounted vertically on a turn-table inside the tunnel. The end-plates were fixed to the turn table such that the chords of the aerofoils were aligned with the $0°$ line of the turn table. The turn-table was controlled using a digital controller which could position the table within $\pm 0.1°$ of the desired angle.

### 3.2.7 Data processing

The data from the sensors was recorded in a CSV file and imported into MATLAB and the following calculations were done in MATLAB.

#### Surface pressures and coefficient of pressures

The static pressure ($P_{static}$) recorded by the pitot tube was subtracted from the mean pressure values at the taps to obtain the surface pressure at the taps ($P_{tap}$). To calculate the coefficient of pressure at the tap, equation 3.1 was used. $P_{stagnation}$ was recorded by the pitot tube. $C_{Pressure}$ was plotted against chord length for the upper and lower surface of the aerofoil to get $C_{Pressure}$ curves for analysis.

$$C_{pressure} = \frac{P_{tap} - P_{static}}{\frac{1}{2}\rho_{\infty}V_{\infty}^2} = \frac{P_{tap} - P_{static}}{P_{stagnation} - P_{static}} \tag{3.1}$$

#### Lift and drag coefficients from surface pressures

To calculate the lift and drag forces from surface pressures, tangential and normal forces were calculated first. The chord length of the aerofoil was divided into 500 parts starting from the leading edge. The $C_{Pressure,i}$ for the midpoints of these segments were extrapolated from measured values. The normal ($\Delta x_i$) and tangential($\Delta y_i$) areas on which the pressure acted was calculated for the segments from the aerofoil profile. The normal and tangential forces were computed by multiplying $C_{Pressure,i}$ with ($\Delta x_i$) and ($\Delta y_i$), respectively. Since positive pressure on top of the aerofoil would push it down, the sum of forces acting on upper surface was subtracted from the sum of forces on the lower surface to get the Lift Coefficient. For the tangential force, the sign of $\Delta y_i$ incorporates the direction of the tangential force.

$$C_N = \sum_{LowerSurface} C_{Pressure,i}\frac{\Delta x_i}{c} - \sum_{UpperSurface} C_{Pressure,i}\frac{\Delta x_i}{c} \tag{3.2}$$

$$C_T = \sum C_{Pressure,i}\frac{\Delta y_i}{c} \tag{3.3}$$

After obtaining the tangential and normal components, a transformation matrix was applied to $C_N$ and $C_T$ for angle of attack ($\alpha$) to obtain the lift and drag coefficients ($C_L$,$C_D$). The efficiency of the aerofoil was calculated as $C_L/C_D$.

$$\begin{bmatrix} C_L \\ C_D \end{bmatrix} = \begin{bmatrix} \cos\alpha & -\sin\alpha \\ \sin\alpha & \cos\alpha \end{bmatrix} \begin{bmatrix} C_N \\ C_T \end{bmatrix} \tag{3.4}$$

### Drag coefficients from pressures in the wake

The coefficient of drag was calculated using the wake survey method. The equation 3.5 as described in [BRP99] was used to calculate the drag coefficient.

$$C_D = 2/S \int\int_S (U_{wake}/U_\infty - U^2_{wake}/U^2_\infty) \tag{3.5}$$

where $S$ is the area of the aerofoil section.

### Efficiency

The ratio of the coefficients of lift and drag (that is, $C_L/C_D$) is called efficiency of the aerofoil.

### Suction velocity

The pressure differential recorded by the venturi tube was used to calculate the mass flow rate inside the venturi tube. The mass flow rate and the area of the suction slit were used to find the suction velocity.

The mass flow rate through the venturi was calculated as:

$$Q = Area_1 \sqrt{2\rho \cdot \frac{(p_1 - p_2)}{\left(\frac{Area_1}{Area_2}\right)^2 - 1}} \tag{3.6}$$

where $Area_1$ and $Area_2$ were the areas at the two measurement positions in the venturi tube, and $p_1$, $p_2$ were the pressures at the respective positions (Figure 3.7). The average velocity of suction ($u_s$) at slit was calculated by dividing mass flow rate by the slit area.

### Suction ratio and momentum coefficient

The Suction ratio ($C_{suction}$)and the Momentum coefficient ($C_\mu$) were used to quantify the rate of suction.

Suction ratio is described as the ratio of velocity of the air through the suction slit with the free stream velocity.

$$C_{suction} = \frac{u_s}{U_\infty} \tag{3.7}$$

Momentum coefficient is defined as the ratio of momentum of air drawn in to the momentum of the air passing over the aerofoil surface, that is,

$$C_\mu = \frac{\rho\, A_{slit}\, u_s^2}{\rho\, A_{aerofoil}\, U_\infty^2} \tag{3.8}$$

## 3.3 Steady state tests

The steady state experiments were conducted at both, the IITB $220kW$ wind tunnel and the Monash University $450kW$ wind tunnel. The objective of these tests was to obtain time-averaged values of pressure distribution around the aerofoils. Table 3.3 outlines the static experiments that were performed for gathering surface pressures. The pressure data was collected for these tests for $30s$ and averaged to get the mean value. The equations described in Section 3.2.7 were used to calculate the lift and drag coefficients for the aerofoils.

Table 3.3: Steady-state tests conducted for surface pressure

| Wind Tunnel | Aerofoil Profile | End Plates | Suction location $(x/c)$ | Wind Speed (m/s) | Re | $\alpha$ (°) |
|---|---|---|---|---|---|---|
| IITB | NACA0012 | No | 0.2,0.4,0.6 | 2,2.5,3,3.5 | 33,000-57,000 | 0-20 |
| IITB | S814 | No | 0.12,0.24,0.44,0.64 | 2,2.5,3,3.5 | 33,000-57,000 | 0-20 |
| Monash | NACA0012 | Yes | 0.4 | 5,10, 20, 30 | 82,000-492,000 | 0-45 |
| Monash | NACA0012 | No | 0.4 | 10 | 82,000 | 0-45 |
| Monash | S814 | Yes | 0.24 | 5,10, 20, 30 | 82,000-492,000 | 0-45 |
| Monash | S814 | No | 0.24 | 10 | 82,000 | 0-45 |

Drag estimates for low angles of attack were estimated from the wake survey method, as described in Section 3.2.7. The tests conducted for obtaining the pressures and velocities in the wake are outlined in Table 3.4.

Table 3.4: Static Tests Conducted for Wake Pressures

| Wind Tunnel | Aerofoil Profile | End Plates | Suction location $(x/c)$ | Wind Speed (m/s) | Re | $\alpha$ (°) |
|---|---|---|---|---|---|---|
| Monash | NACA0012 | Yes | 0.4 | 5,10, 20, 30 | 82,000-492,000 | 0-21 |
| Monash | S814 | Yes | 0.24 | 5,10, 20, 30 | 82,000-492,000 | 0-21 |

### 3.3.1 Visulalisations

A set of visualisation tests were conducted for preliminary investigation before the quantitative tests:

#### Smoke visualisations

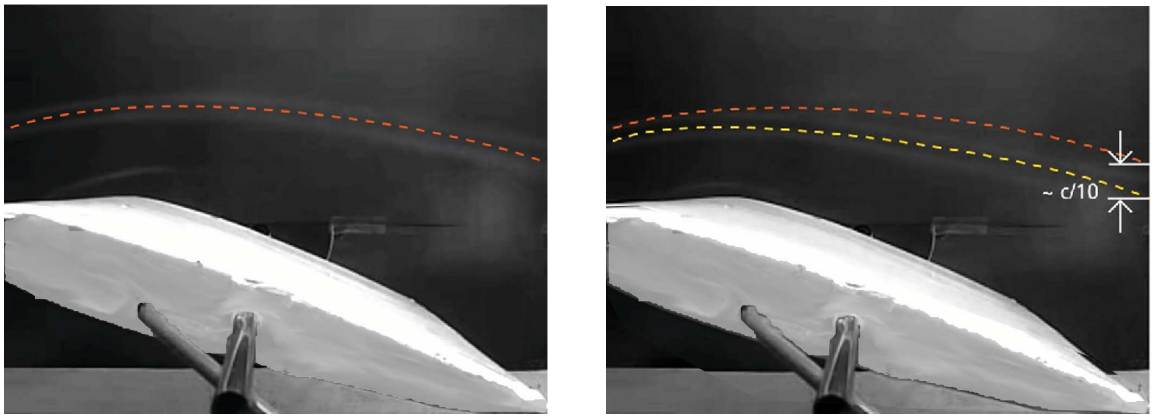


(a) Suction off

(b) Suction on

Figure 3.11: Smoke visualisation, NACA0012 aerofoil, $Re = 3.3 \times 10^4$

Smoke visualisation tests were done at IIT Bombay. The aerofoil section was mounted in the wind tunnel. In a reservoir outside the wind tunnel, smoke was created by evaporating smoke oil using a wick wrapped around a heating element. The smoke was then injected in the tunnel using a streamlined feeder pipe which was mounted vertically in the centre of the flow, upstream of the aerofoil, in the contraction section of the wind tunnel. The feeder pipes were $5mm$ in diameter and $20cm$ long. The feeder pipes were kept parallel to the flow in the tunnel, to minimise separation. The details of the set-up are shown in Figure 3.10. Smoke streaks were observed for deflection when suction was switched on, as shown in Figure 3.11. In these figures, air is flowing from the left to right.

Figure 3.11(a) shows the smoke streak-line (highlighted by a dashed line) over the aerofoil without employing flow-control. Figure 3.11(b) shows the aerofoil with suction on, and the corresponding smoke streak-line highlighted using a dashed line, closer to the surface. The streak-line from suction-off case is also superimposed in the image, and is further away from the surface of the aerofoil. Thus, the streak-lines moved closer to the surface of the aerofoil by about $0.1c$ around the trailing edge. The position of the suction slit was varied from $0.2c$ of the chord length from the leading edge to $0.6c$ of the chord length. The best results were achieved for the angle of attack $\sim 20^{\circ}$ and when the suction slit was closer to the leading edge. The wind speed was kept at $2m/s$.

This movement of streak-lines closer to the aerofoil surface on applying surface-suction based flow-control indicates that the boundary layer was reduced and the inviscid layer moved closer to the surface, as was expected. However, since the streaklines are not distinctively visible, this may only be considered as a preliminary evidence of boundary layer reattachment. For final tests in the Monash $450kW$ wind tunnel, wool tuft visualization technique was used.

### Wool tuft visualisations

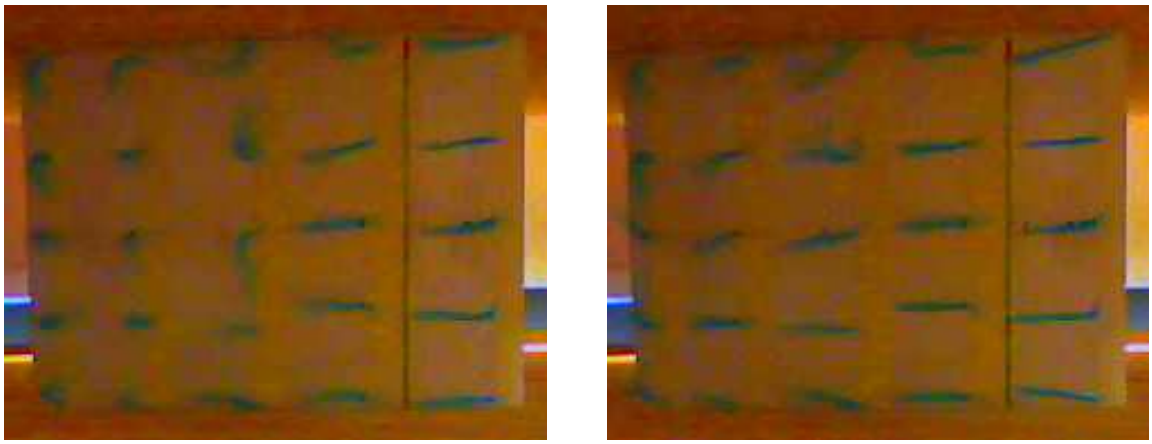

(a) Suction off

(b) Suction on

Figure 3.12: Wool tuft visualisations, S814, $U_{\infty} = 10m/s$, $Re = 1.6 \times 10^5$ , $\alpha = 20^{\circ}$

Wool tuft visualisation were conducted at the Monash University wind tunnel. For attached flow, the wool tufts followed the direction of the flow, whereas for separated flow, they fluttered and lifted off the surface. Figure 3.12 shows the wool tuft visualisations for S814 aerofoil profile at $U_{\infty} = 10m/s$, $Re = 1.6 \times 10^5$ and $\alpha = 20^{\circ}$. The air flow

is from right to left in these figures. There are five columns of wool tufts. The suction slit is between the first and second column of the wool tufts. Without applying suction, the boundary layer separated between the middle of the aerofoil and the trailing edge (Figure 3.12(a)). There was no reattachment towards the trailing edge, indicating the absence of a separation bubble at this angle of attack. When suction was switched on, the wool tufts rearranged and were more aligned with the direction of the flow, as shown in Figure 3.12(b). It can be visually concluded that surface suction prevented boundary layer separation over the aerofoil.

Another observation was that the top and bottom rows of the wool tufts shown in the figure were not oriented parallel to the flow direction, indicating potential three-dimensional effects due to the boundary layer over the end-plates. The rest of the rows of the wool tufts, which were closer to the span-wise centre of the aerofoil, pointed in the direction of the flow, indicating that the flow could be considered as a uniform two-dimensional flow over the centre of the aerofoil.

The visual method showed qualitatively, the better attachment of the boundary layer to the aerofoil surface. A discussion on quantitative tests follows.

### 3.3.2 Preliminary tests at IITB 220kW tunnel

Tests in the IIT Bombay 220kW tunnel were performed for low wind speeds. The wind speeds for these tests were $2m/s$, $2.5m/s$ $3m/s$ and $3.5m/s$. The corresponding chord $Re$ were $3.3 \times 10^4$, $4.1 \times 10^4$, $4.9 \times 10^4$ and $5.7 \times 10^4$. Multiple slit positions for suction were tested for both aerofoil profiles - NACA0012 and S814. These learning from these tests were used to select set up parameters for the final experiments at the Monash University wind tunnel. The results from the IIT Bombay wind tunnel tests were not used in the numerical simulations in Chapter 4.

It must be noted that negative pressures on the suction surface of the aerofoil produce the upward force, lift. Hence, the figures depicting surface pressure and $C_{Pressure}$ have a reversed vertical axis. Thus, on $C_{Pressure}$ curves, a peak implies a local minima. Similarly, in the discussion of the values of pressures, increased magnitudes indicate a decrease in the absolute value of pressure. In the subsequent sections, the increased magnitudes of pressure (decreased absolute values) are favourable to the production of lift, which the reader should bear in mind in order to avoid confusion.

**Surface pressures between the leading edge and the suction slit**

Figure 3.13 shows the surface pressures for the three slits for angle of attack = 9° and wind speed $2m/s$, which corresponds to $Re = 3.3 \times 10^4$. For the first position (at $0.2c$ from the leading edge), on the application of suction, the surface pressure decreased and attained a magnitude between 1.4 and 1.5 times the suction-off value for various angles of attack. For the second position (at $0.4c$ from the leading edge), the suction-on pressure was 1.2 times the suction-off pressure at the leading edge. This ratio increased to 1.5 times immediately upstream of the slit. For the third position (at $0.6c$ from the leading edge), the change in pressure from the leading edge to $0.4c$ from the leading edge was lesser than the other two slit positions. The ratio of suction-on and suction-off pressures was $\sim 1.1$. However, between $0.4c$ and $0.6c$ ratio increases to 1.7.

Thus, on application of suction, the pressure between the leading edge and the slit decreased over the suction-off value for all three slit positions. These observation suggest a better attachment of the flow upstream of the slit when suction is applied.

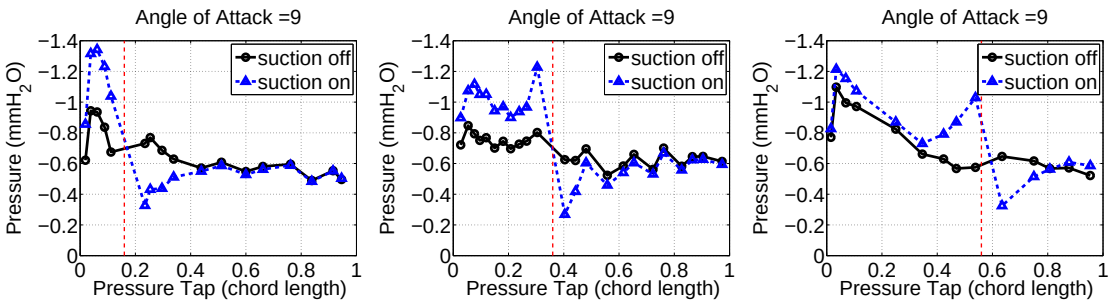


(a) Suction at $x = 0.16c$ (b) Suction at $x = 0.36c$ (c) Suction at $x = 0.56c$

Figure 3.13: Surface pressures, NACA0012, $\alpha = 9°$, $Re = 4.1 \times 10^4$

**Surface pressures between the suction slit and the trailing edge**

The pressures immediately downstream of the slit increased for all three slit positions. The pressure, however, immediately recovered towards the trailing edge of the aerofoil. This increase in pressure indicates a lower wind velocity immediately downstream of the slit. The slit walls were kept perpendicular to the surface of the aerofoil. Thus, when suction was applied, boundary layer was drawn in from both, upstream and downstream of the slit. This accelerated the flow immediately upstream and decelerated the flow immediately downstream of the slit, resulting lower pressure upstream and higher pressure downstream

of the slit, which can be verified by observing the sharp increase in pressure across the slit.

**Lift, drag and efficiency**

The section $C_L$, $C_D$ and $C_L/C_D$ were calculated using the surface pressure measurements over the aerofoil and the methodology described in Section 3.2.7. Figure 3.14 and shows the variation of $C_L$, $C_D$ and $C_L/C_D$ for different angles of attack for slit at $x/c = 0.36$, and $Re = 4.9 \times 10^4$.

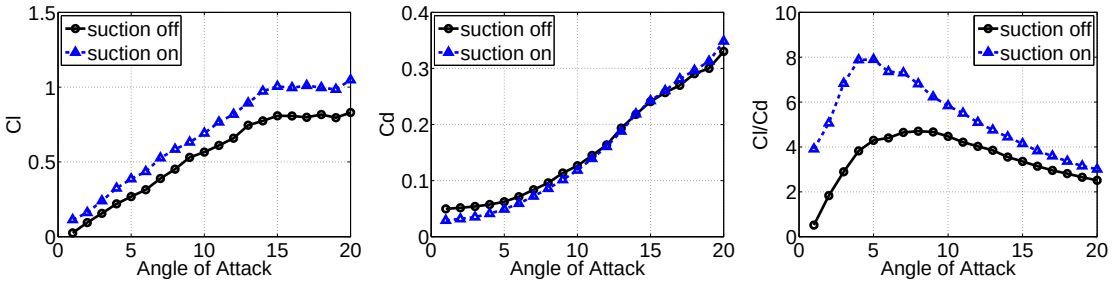


(a) $C_L$ (b) $C_D$ (c) $C_L/C_D$

Figure 3.14: Suction at $x/c = 0.36$, $Re = 4.9 \times 10^4$, NACA0012

$C_L$ for pre-stall angles of attack improved for the aerofoils with suction slits at $x/c = 0.36$ and $x/c = 0.56$. The improvement was more than 60% for angle of attack close to 1° and decreased steadily to about 20% at the stall angle ($\sim 5°$). The enhancement in $C_L$ remains between 15% and 20% for angles of attack between 5° and 20°. For the slit position at $x/c = 0.16$, $C_L$ worsened until the stall angle was reached. After the stall angle, however, $C_L$ improved by a maximum of 20%. The maximum overall improvement in $C_L$ was for the slit position at $x/c = 0.36$.

$C_D$ reduced for all angles of attack for the slit position $x/c = 0.16$. For suction slit at $x/c = 0.36$, $C_D$ reduced for low angles of attack and increased for angles of attack greater than 11°. For suction at $x/c = 0.56$, $C_D$ increased for all angles of attack.

$C_L/C_D$ increased for the first slit position, $x/c = 0.16$ only after the stall angle. The improvement over the baseline was around $40\% - 50\%$ for angles of attack between 6° and 15°. On the application of suction, $C_L/C_D$ was maximum after the stall angle. For suction at $x/c = 0.36$, $C_L/C_D$ improved for all angles of attack. The improvement ranges from almost two-fold over the baseline at angle of attack = 1°. It decreased to $\sim 65\%$ improvement at 5° and remained well over 30% at the angle of attack = 10°. On the application of suction, $C_L/C_D$ was the maximum close to the stall angle. $C_L/C_D$ for all

Table 3.5: Comparison of suction effects on NACA0012 aerofoil

| | slit at x=0.16c | slit at x=0.36c | slit at x=0.56c |
|---|---|---|---|
| pressure: | | | |
| leading edge to slit | 40% – 50% | 20% – 50% | 10% – 70% |
| slit to trailing edge | worsens & recovers | worsens & recovers | worsens & recovers |
| $C_L$ enhancement | 45% | 60% | 40% |
| $C_D$ enhancement | -20% – -10% | -20% – 5% | -5% – 15% |
| $C_L/C_D$ enhancement | 40% – 50% | 100% – 65% | 50% – 30% |
| maximum benefit of suction | after stall angle | at stall angle | before stall angle |

angles of attack for the third slit position, $x/c = 0.56$ as well. It improved by 50% before the stall angle to around 30% at the stall angle and around 15% at the angle of attack = 10°. On the application of suction, $C_L/C_D$ was maximum before the stall angle.

### *S814*

#### Surface pressures

The surface pressure readings on the top of the 814 aerofoil for the four slit positions are presented in Figure 3.15. The results are presented for angle of attack 9° for all four slit positions. The wind speeds were $2m/s$, corresponding to $Re = 3.3 \times 10^4$. The surface pressure distribution was similar to the trend observed with the NACA0012 aerofoil. The pressure improved between the leading edge and the suction slit. The ratios for suction-on and suction-off pressures were as high as 1.8 immediately upstream of the slit. The pressure worsened behind the suction slit, just as in the case of the NACA0012 aerofoil. However, the pressure downstream of the slit did not recover as quickly for the two slits closer to the trailing edge as compared to the two closer to the leading edge.

#### Lift, drag and efficiency

Figures 3.16, 3.17 and 3.18 show the variation of $C_L$, $C_D$ and $C_L/C_D$ for different angles of attack for the four slit positions.

$C_L$ increased in all cases when suction was applied. The enhancement in lift for suction at $x/c = 0.12$ was between 10% and 20%. For suction at $x/c = 0.24$, the lift improved by 20% – 50% and for the suction at $x/c = 0.44$, the lift improved by 15% – 20%.

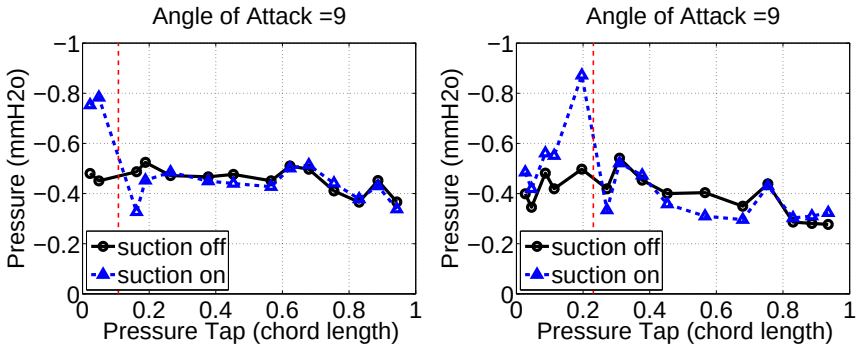


(a) suction at $x = 0.12c$ (b) suction at $x = 0.24c$

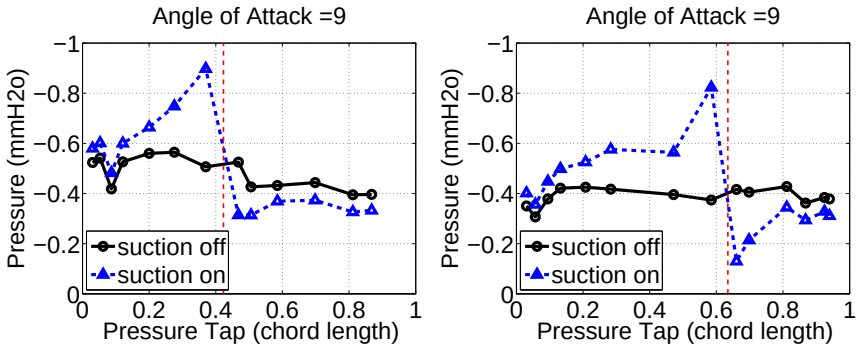


(c) suction at $x = 0.44c$ (d) suction at $x = 0.64c$

Figure 3.15: Surface pressures, $\alpha = 9°$, $3.3 \times 10^4$, S814 profile

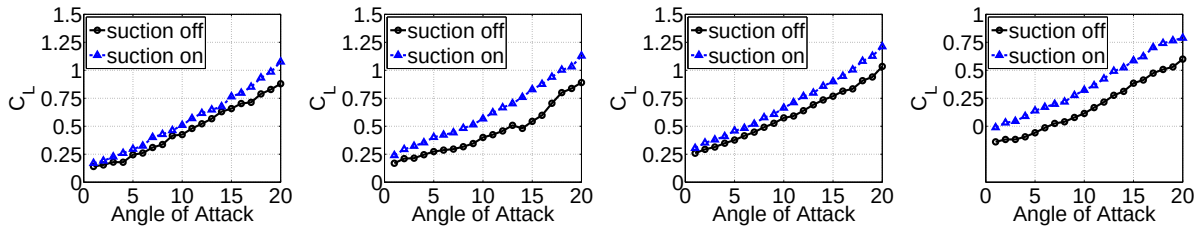


(a) suction at x = 0.12c (b) suction at x = 0.24c (c) suction at x = 0.44c (d) suction at x =0.64c

Figure 3.16: $C_L$ for different slit positions, $Re = 4.9 \times 10^4$, S814

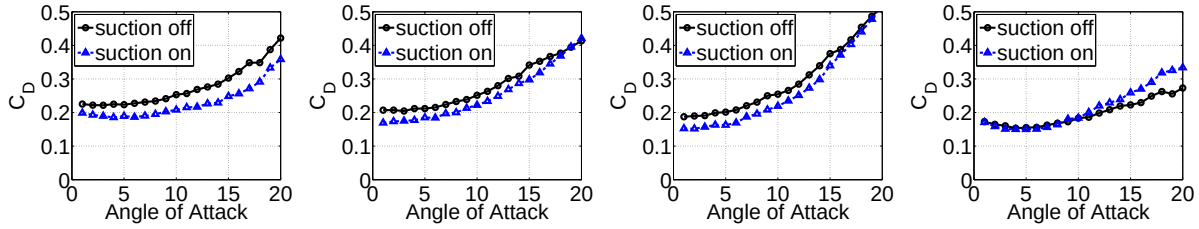


(a) suction at x = 0.12c (b) suction at x = 0.24c (c) suction at x = 0.44c (d) suction at x = 0.64c

Figure 3.17: $C_D$ for different slit positions, $Re = 4.1 \times 10^4$ ,S814

Table 3.6: Comparison of suction effects on S814 aerofoil

| | slit at x=0.12c | slit at x=0.24c | slit at x=0.44c | slit at x=0.64c |
|---|---|---|---|---|
| pressure: | | | | |
| leading edge to slit | 40% – 50% | 20% – 50% | 10% – 70% | 5% – 50% |
| slit to trailing edge | worsens | worsens | worsens | worsens |
| lift enhancement | 10% – 30% | 20% – 50% | 15% – 20% | 15% – 20% |
| drag enhancement | -25% – -5% | -20% – 5% | -25% – 5% | -5% – 20% |
| efficiency enhancement | 25% – 40% | 20% – 60% | 20% – 50% | 10% – 30% |
| maximum benefit | 5°–15° | 0°–10° | 0°–5° | 0°–5° |

$C_D$ reduced for most of the cases. With the suction closer to the leading edge of the aerofoil, drag decreased for all angles of attack. With the suction slit in the middle of the aerofoil, the drag reduced for low angles of attack, but increases slightly for higher angles of attack. For low angles of attack, drag decreased by up to 25% for all positions of the slit. For higher angles of attack, the maximum increase in drag is up to 5%.

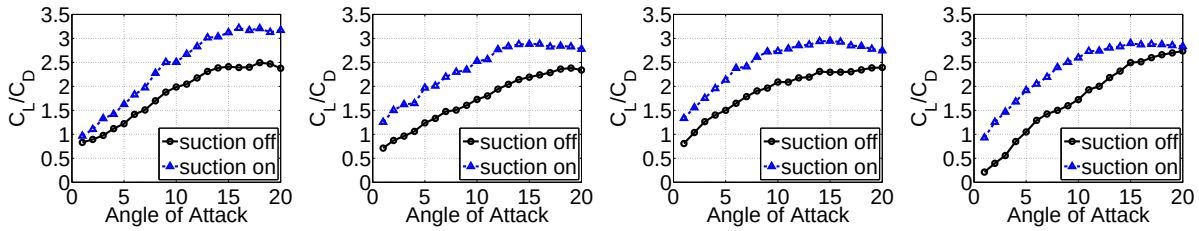


(a) suction at x = 0.12c (b) suction at x = 0.24c (c) suction at x = 0.44c (d) suction at x = 0.64c

Figure 3.18: $C_L/C_D$ for different slit positions,$5.7 \times 10^4$, S814

With improvement in $C_L$ and reduction in $C_D$, $C_L/C_D$ of the aerofoil increased in all cases. The improvement for suction at $x = 0.12c$ was 25% – 40%, 20% – 60% for $x = 0.24c$ and 20% – −50% for $x = 0.44c$. Applying suction in the front of the aerofoil improved $C_D$ at higher angles of attack, and moving the suction slit backwards lowered the angle of attack for maximum $C_L/C_D$.

These tests were conducted to gather preliminary data for both aerofoil profiles and to understand flow-control through surface suction. The $C_L$ and $C_D$ values from these tests were not used in numerical simulations in Chapter 4, instead, they were used to select the slit positions and test parameters for the final tests.

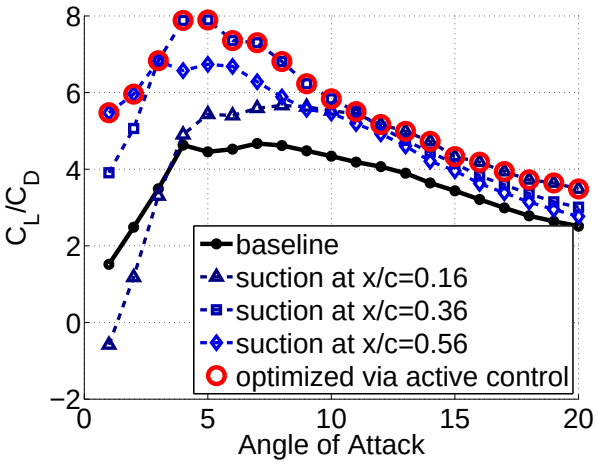


Figure 3.19: Optimised efficiency curve using active control

As seen earlier, the positioning of the suction slits affected the efficiency of the aerofoil versus the angle of attack curve peak. For suction slit closer to the trailing edge, the maximum enhancement in efficiency over the baseline case occurred at low angles of attack. For suction slit closer to the leading edge, the maximum enhancement in efficiency occurred at higher angles of attack. Figure 3.19 shows the curves for the three slit positions of NACA0012 aerofoil, and the baseline case. The black line shows the baseline case, without suction. The dashed blue lines show the efficiency for suction at $x/c = 0.16$, 0.36 and 0.56 from the leading edge.

With an active control strategy to activate different slits at different angles of attack, the aerofoil can achieve higher efficiency over a larger angle of attack range. This will make the efficiency curve flatter, as shown in the figure using red circles. This would enable the aerofoil to be used over a larger angle of attack range. Having a higher and flatter curve for efficiency will help in reducing optimisation constraints while designing the blade for various stages of operation. The benefits and effectiveness of this method needs to be further analysed, but has not been covered in this thesis.

### 3.3.3 Final tests at Monash 450kW wind tunnel tests

Tests at Monash University were conducted in the $450kW$ wind tunnel. Both, NACA0012 and S814 profiles were tested, but only one slit position per profile was used. For the NACA0012 profile, the suction slit was at $x/c = 0.36$ and for S814 the slit position was

$x/c = 0.24$ (refer to Section 3.2.2 for the reasons dictating these choices). The wind speeds for these tests were higher than those at IIT Bombay to achieve higher $Re$. The tests were conducted at $5m/s$, $10m/s$, $20m/s$ and $30m/s$. The resulting chord $Re$ were $8.2 \times 10^4$, $1.6 \times 10^5$, $3.2 \times 10^5$ and $4.9 \times 10^5$. The suction rate was varied for these tests and the improvements were analysed for different suction rates. The results from these tests were used for simulations in Chapter 4.

### 3.3.4 Coefficient of pressure

The pressure distribution over the aerofoil was characterised using the non-dimensional Coefficient of Pressure ($C_{Pressure}$). The difference between the surface pressure and the static pressure inside the wind tunnel was divided by dynamic pressure to obtain $C_{Pressure}$. This section describes how $C_{Pressure}$ changed on the application of suction. For these tests, the suction velocity at the slit was kept constant at $17.6m/s$.

Figure 3.20 shows the $C_{Pressure}$, with a solid line for suction-off, for $Re = 8.2 \times 10^4$ for the NACA0012 aerofoil, $\alpha = 3°$, $9°$ and $18°$. The aerofoil is stalled at $18°$ for the $Re$ $8.2 \times 10^4$. The angle of attack range $\alpha = 3°$ - $9°$ is typical for conditions where a separation bubble forms [MO87]. In Figures 3.20(a) and 3.20(b), for the flow control by suction switched off, the pressure on the suction side decreased rapidly up to a peak near the leading edge. Downstream of this peak, the pressure recovered, with the rate of recovery decreasing steadily till the $C_{Pressure}$ reached a plateau. This plateau indicates region of a separation bubble [MO87, YB12].

Figure 3.20(c) shows typical conditions for a separated boundary layer without reattachment. The pressure has a small peak immediately downstream of the leading edge. Downstream of this peak, the pressure recovered by a small amount and remained flat till the trailing edge. The absence of a significant peak and a flat $C_{Pressure}$ curve at higher plateaus as compared to lower angles of attack indicates that the aerofoil had stalled at the angle of attack of $18°$.

When suction was applied, the pressure distribution on the suction surface changed substantially as compared to the non-suction case, as shown by a dashed line in Figures 3.20(a), 3.20(b) and 3.20(c). In these figures, the vertical dotted line shows the position of the suction slit. Upstream of the slit, the pressure decreased for all three angles of attack. The peak immediately behind the leading edge attained a lower pressure as

compared to the non-suction case. Slightly upstream of the suction, there was another peak which indicated that suction accelerated the flow upstream of the slit by creating low pressure over the slit area. The air flowing over the surface experienced a negative pressure gradient, which increased its velocity. Similarly, just downstream of the slit, the pressure gradient became positive, thus, it retarded the flow. Hence, the pressure directly downstream of the slit increased, compared to the non-suction case. However, the pressure gradient had a local effect, and the pressure reduced again downstream of the slit and matched with the non-suction case at the trailing edge.

The most important effect of suction was seen for post-stall angles of attack for $Re = 8.2 \times 10^4$ (Figure 3.20(c)). Instead of a small peak, a significantly higher peak was observed, following which, the pressure steadily increased downstream of the peak till the suction slit. The pressure gradient over the suction slit accelerated the flow upstream and decelerates the flow downstream of the slit, similar to what was observed at the pre-stall angles of attack. Downstream of the slit, the pressure steadily recovered till the trailing edge. A significant low pressure area between the leading edge and the slit indicates that the application of suction prevented boundary layer separation and effectively avoided stall at $\alpha = 18°$ for $Re = 8.2 \times 10^4$.

The pressures on the non-suction (pressure) surface of the aerofoil, however, were not affected by suction for angles of attack lesser than the stall angle. Above the stall angle, there was an insignificant change in the pressure profile for suction-on. The pressure increased by a small amount for all pressure taps on the non-suction surface when suction was applied.

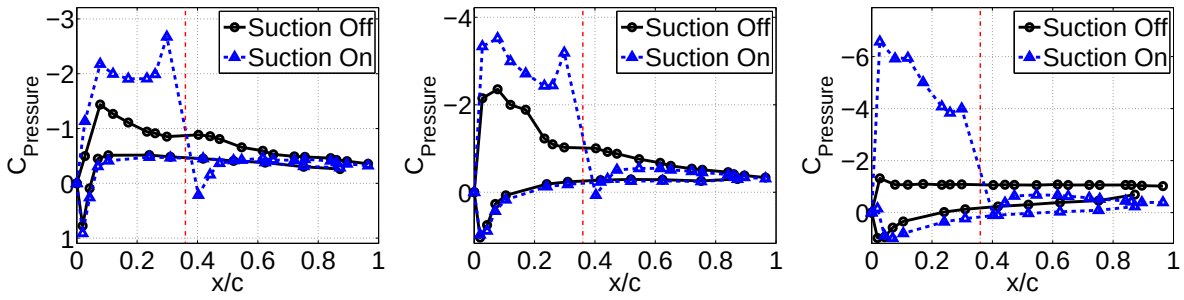


(a) $\alpha = 3°$ (b) $\alpha = 9°$ (c) $\alpha = 18°$

Figure 3.20: $C_{Pressure}$ for NACA0012 $x/c = 0.36$, $U_\infty = 5m/s$, $Re = 8.2 \times 10^4$

For the NACA0012 aerofoil at $Re = 3.3 \times 10^5$ (Figure 3.21), trends similar to $Re =$

$8.2 \times 10^4$ were observed with and without flow control. Without the suction applied, for angles of attack of 3° and 9°, there was a peak immediately downstream of the leading edge for the suction surface. Downstream of the peak, the pressure recovered, but flattened for some distance, indicating a separation bubble similar to the lower Reynolds number flow. Downstream of this plateau, the pressure steadily recovered till the trailing edge. For the post-stall angle, there was a small peak just downstream of the leading edge, downstream of which, the pressure recovered and remained flat till the trailing edge.

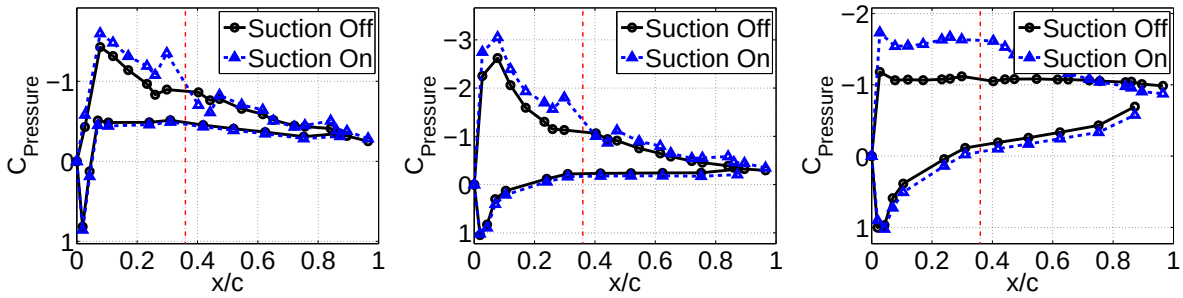


(a) $\alpha = 3°$ (b) $\alpha = 9°$ (c) $\alpha = 18°$

Figure 3.21: $C_{Pressure}$ for NACA0012, $x/c = 0.36$, $U_\infty = 20m/s$, $Re = 3.3 \times 10^5$

When suction was applied, higher peaks were observed immediately downstream of the leading edge for all three angles of attack, similar to the application of suction for $Re = 8.2 \times 10^4$. The peaks at higher $Re$ were not as pronounced as those at lower $Re$. The reason for lower peaks was that the wind speed increased, while the suction velocity remained constant. This reduced the suction momentum coefficient ($C_\mu$), which reduced the effectiveness of suction. This behaviour is detailed in Section 3.3.7. Similar to $Re = 8.2 \times 10^4$, the pressure gradient over the suction slit accelerated the flow upstream of the slit, which reduced the pressure, and decelerated the flow downstream of the slit, which increased the pressure. Suction also avoided the boundary layer separation, and thus, stall at the angle of attack 18°.

The pressures over the surface of the S814 aerofoil profile are shown in Figures 3.22 and 3.23. The $Re$ for these tests were $1.6 \times 10^5$ and $4.9 \times 10^5$, respectively. For an angle of attack of 5° without suction, the pressure over the suction surface decreased rapidly downstream from the leading edge for both $Re$. A sudden increase in pressure was seen at about $0.12c$ downstream from the leading edge. The pressure decreased sharply again at around $0.28c$. This sudden increase in pressure and subsequent decrease indicated a

local separation and reattachment, known as a laminar bubble [ST95]. This bubble was observed for both $Re$.

For an angle of attack of 9°, similar separation bubble was observed. However, the separation bubble moved forward from $0.12c$ to $0.025c$ with an increase in $Re$. Somers et. al. [ST95] found the separation bubble moved forward for an increased angle of attack for the S814 aerofoil at $Re = 1.5 \times 10^6$. The separation bubble did not occur for Somers et. al. [ST95] beyond an angle of attack of 7°. Since our experiments were performed at lower $Re$, in which aerofoils are more prone to separation, the bubble was expected to be seen even at higher angles of attack.

The pressure recovered downstream after the peak for angle of attack of 5° till the trailing edge. For angle of attack 9°, the pressure recovered till $0.55c$ for Re $1.6 \times 10^5$, downstream of which, the boundary layer separated. At Re $1.6 \times 10^5$, the pressure recovered till $0.65c$ for angle of attack 9° before the boundary layer separated. For post stall angles, the pressure decreased rapidly over the suction surface downstream from the leading edge. There was no peak, and the pressure curve remained flat from close to the leading edge till the trailing edge.

On the pressure side, the pressure increased downstream from the leading edge to the stagnation point, rapidly. Downstream of the stagnation point, the flow accelerated due to the curvature of the aerofoil, which decreased the pressure. $C_{Pressure}$ decreased to a minimum of close to -1 for pre-stall angles, and -0.5 for post stall angles of attack. This minimum pressure was observed till the thickness of the aerofoil decreased, that is, till $0.35c$. Downstream of this point, the pressure recovered steadily till the trailing edge.

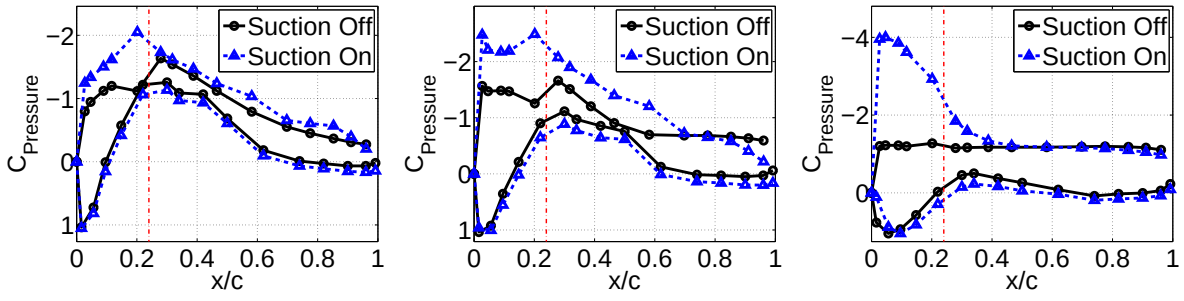


(a) $\alpha = 5°$ (b) $\alpha = 9°$ (c) $\alpha = 23°$

Figure 3.22: $C_{Pressure}$ for S814, $x/c = 0.24$, $U_\infty = 10m/s$, $Re = 1.6 \times 10^5$

On application of suction, the pressure on the suction surface, downstream of the leading edge, decreased further than in the case without suction. The laminar separation

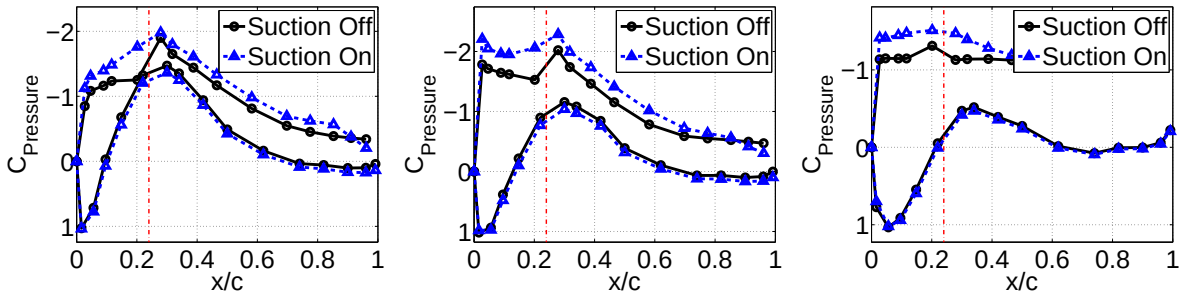


(a) $\alpha = 5°$ (b) $\alpha = 9°$ (c) $\alpha = 23°$

Figure 3.23: $C_{Pressure}$ for S814, $x/c = 0.24$, $U_\infty = 30m/s$, $Re = 4.9 \times 10^5$

bubble was not present for the angle of attack of 5° for both $Re$. The pressures in suction and non-suction cases remained close to each other, downstream of the suction slit. For an angle of attack of 9°, the separation bubble was present. A higher peak was observed for suction as compared to that in the non-suction case. For both Re numbers, $1.6 \times 10^5$ and $4.9 \times 10^5$, the pressure recovered from downstream of the slit to the trailing edge, indicating that the boundary layer remained attached to the aerofoil surface when suction was applied.

For post stall angles, the pressure downstream of the leading edge decreased on the application of suction. For Re $1.6 \times 10^5$, the $C_{pressure}$ reached a minimum of $-4$ before recovering to close to -1 around $0.4c$, downstream of which, the boundary layer separated. For Re $4.9 \times 10^5$, the $C_{pressure}$ remained close to $-1.5$ from just downstream of the leading edge to $0.3c$, after which it slightly recovered till $0.6c$, downstream of which, the boundary layer separated. On the non-suction surface, the pressures were not affected significantly on application of suction.

To summarise, the application of suction significantly altered the $C_{Pressure}$ curve over the aerofoil. The following was observed:

i The leading edge was effected the most on application of suction and the $C_{Pressure}$ decreased substantially when suction was applied. Since the leading edge provides the maximum lift, we expect the lift coefficients to increase substantially with suction.

ii Between the suction slit and the trailing edge, suction was able to prevent boundary layer separation for low angles of attack. The attached boundary layer is expected to increase lift coefficients and decrease drag coefficients.

### 3.3.5 Coefficient of lift

In this section the effect of suction on $C_L$ is discussed. $C_L$ for the NACA0012 aerofoil are presented in Figure 3.24 for Reynolds numbers $8.2 \times 10^4$, $1.6 \times 10^5$, $3.3 \times 10^5$ and $4.9 \times 10^5$. The suction velocity, $u_s$ was kept constant at $17.6 m/s$ for the suction-on tests. Without suction, the lift coefficient curve is affected primarily by the $Re$ and turbulence intensity.

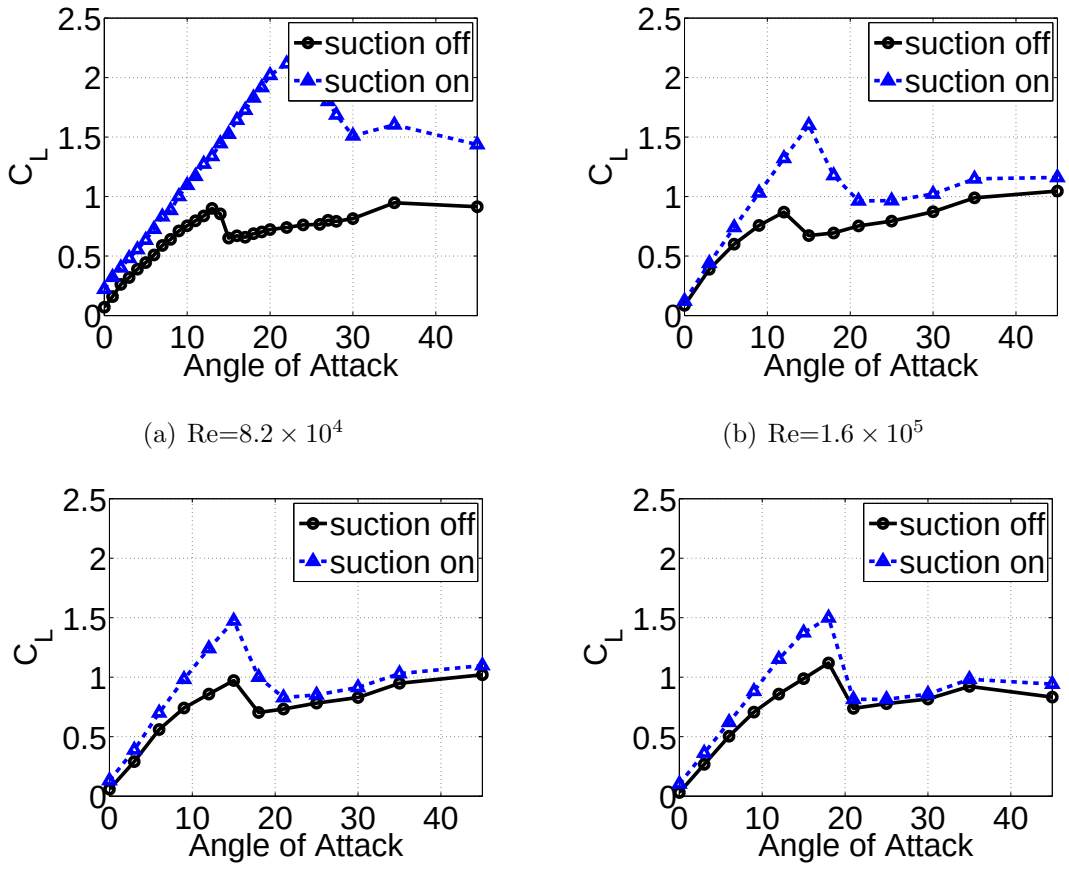


(a) Re=$8.2 \times 10^4$ (b) Re=$1.6 \times 10^5$

(c) Re=$3.3 \times 10^5$ (d) Re=$4.9 \times 10^5$

Figure 3.24: Change in $C_L$ for NACA0012, constant suction

Sheldahl and Klimas [SP81] concluded that the slope of the lift coefficient remains constant for varying $Re$, and the stall angle increases with the increase in the $Re$. Swalwell et al. [SSM01] experimented in the same wind tunnel in Monash University, and found that an increase in turbulence led to an increase in the stall angle. In the experiments conducted for this thesis, the stall angle increased with an increase in the $Re$ and turbulence, as was expected from the works of Sheldahl and Swalwell. For suction-off, the slope of the lift coefficient curve remained constant for all four $Re$. The stall angles were 13°, 12°, 15° and 18° for the $Re$ $8.2 \times 10^4$, $1.6 \times 10^5$, $3.3 \times 10^5$ and $4.9 \times 10^5$, respectively.

The stall angle for Re $8.2 \times 10^4$ was closer to the stall angle for Re $1.6 \times 10^5$ because of the higher turbulence at Re $8.2 \times 10^4$. The average turbulence was 6.5%, 1.4%, 1.3% and 1.1% for the *Re* $8.2 \times 10^4$, $1.6 \times 10^5$, $3.3 \times 10^5$ and $4.9 \times 10^5$, respectively.

On application of suction, $C_L$ increased for all angles of attack and the stall angle was delayed for lower *Re*. Since the suction velocity $u_s$ remained constant, $C_\mu$ was higher for low *Re*. The effect of suction in increasing lift and delaying stall was more significant for lower *Re*. At *Re* $8.2 \times 10^4$, the stall angle for suction-on was 25°, and it was 15°, for *Re* $1.6 \times 10^5$ as compared to 13° and 12°, respectively for the non-suction tests. For *Re* $3.3 \times 10^5$ and $4.9 \times 10^5$, the stall angles remained the same as their non-suction values, 15° and 18°, respectively.

For angles of attack less than the stall angle, $C_L$ increased significantly. For Re $8.2 \times 10^4$, $C_L$ increased by 40% for all angles of attack below the stall angle as compared to the non-suction case. The increase was between 20% and 60% for Re $1.6 \times 10^5$, 20% and 50% for Re $3.3 \times 10^5$ and 20% and 30% for Re $4.9 \times 10^5$ .

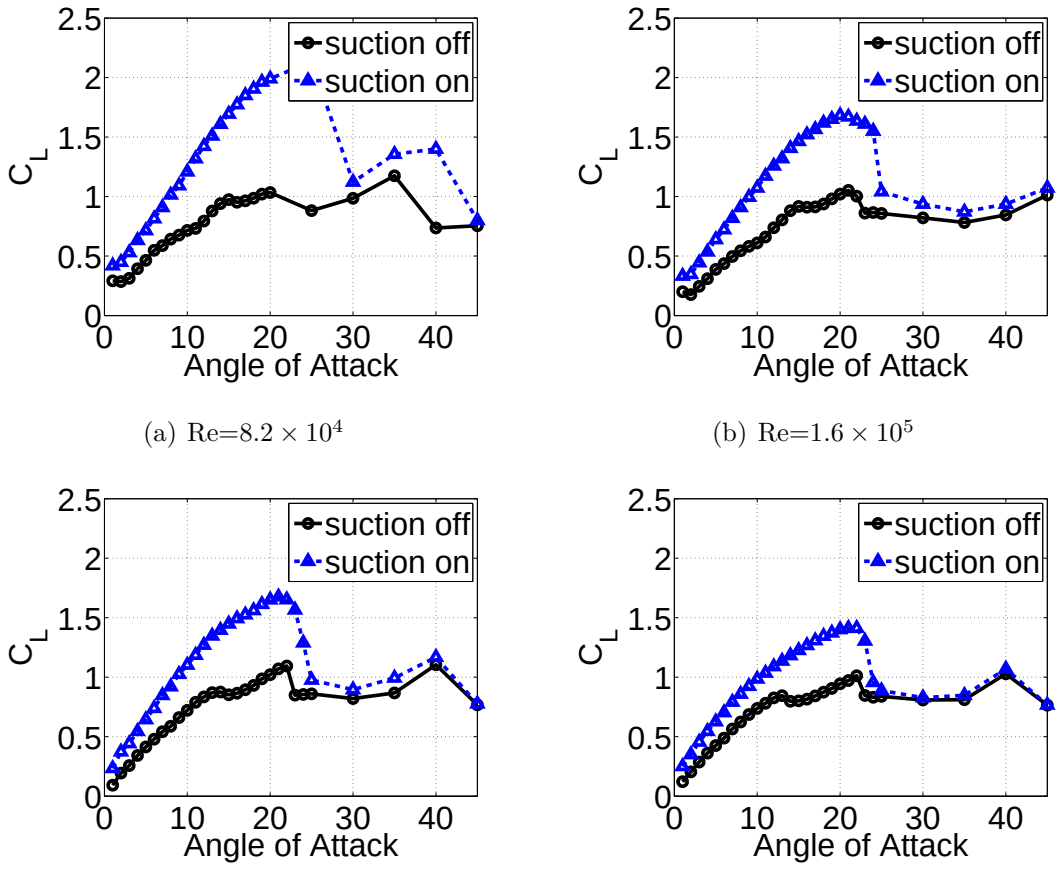


(a) Re=$8.2 \times 10^4$

(b) Re=$1.6 \times 10^5$

(c) Re=$3.3 \times 10^5$

(d) Re=$4.9 \times 10^5$

Figure 3.25: Change in $C_L$ for S814, constant suction

$C_L$ fore S814 aerofoil profile are presented in Figure 3.25 for $Re$ $8.2 \times 10^4$, $1.6 \times 10^5$, $3.3 \times 10^5$ and $4.9 \times 10^5$. Without suction, the aerofoil stalled at the angle of attack of 21° for all four $Re$. For Re $8.2 \times 10^4$, the lift coefficient increased with the angle of attack from 0° to 16°, after which it dropped to 18°, increasing thereafter, till the stall angle of 21°. The same trends were observed for higher $Re$. However, the observed drop in $C_L$ before stall angle occurred at lower angles of attack with the increase in $Re$.

On application of suction, $C_L$ increased for all angles of attack less than the stall angle. For Re=$8.2 \times 10^4$, the aerofoil did not stall till 25°. The maximum $C_L$ increased by 80% from 1.17 to 2.13. For higher Re, the stall angle was between 22° and 24°. $C_L$ increased by more than 50% for all angles of attack on application of suction. The maximum lift coefficients with suction were 1.68, 1.67 and 1.41 for Re $1.6 \times 10^5$, $3.3 \times 10^5$ and $4.9 \times 10^5$, respectively.

Thus, similar trends were observed for both profiles, NACA0012 and S814. To summarise:

i The lift coefficients for pre-stall angles increased significantly on the application of suction.

ii The stall angle was delayed with the application of suction

iii Since $C_L$ increased with suction, implementing a suction flow control technique in wind turbine blades is expected to increase the efficiency of the wind turbines.

### 3.3.6 Coefficient of drag

Figure 3.26(a) shows the velocities in the wake for different angles of attack at Reynolds number $1.6 \times 10^5$ for the NACA0012 aerofoil. This figure is example of a typical wake profile. As the angle of attack increased, the wake width and the maximum velocity deficit increased [NY12]. The wake was angled more downwards for an increase in angle of attack. Figure 3.26(b) shows the wake velocities for an angle of attack of 10° for suction-off and suction-on. With suction on, both, the wake width and maximum velocity deficit decreased.

$C_D$ for the NACA0012 profile for Re= $4.9 \times 10^5$ is shown in Figure 3.26(c). At angles of attack of less than 10°, $C_D$ remained close to 0.05 for the non-suction case. $C_D$

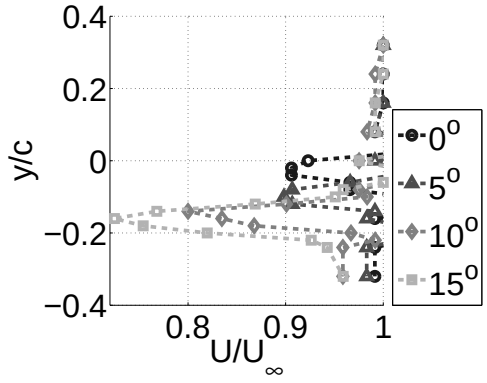


(a) Wake velocities, no suction NACA0012, Re=$1.6 \times 10^5$

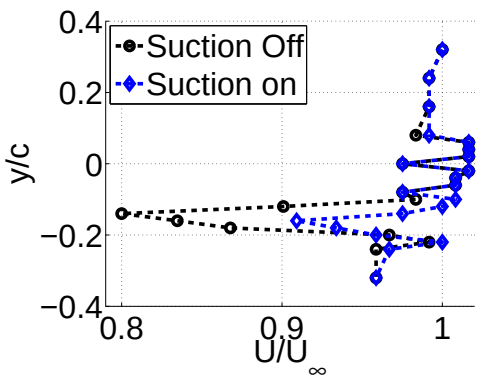


(b) Wake velocities, with and without suction, NACA0012, Re=$1.6 \times 10^5$,$\alpha = 10°$

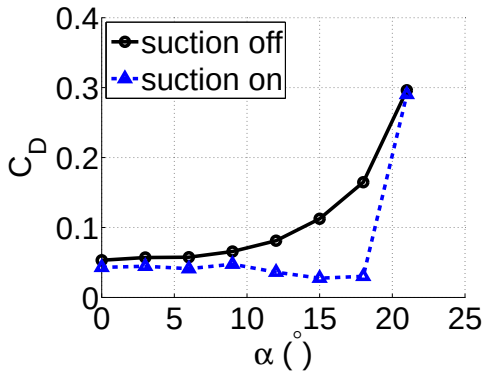


(c) NACA0012, Re=$4.9 \times 10^5$

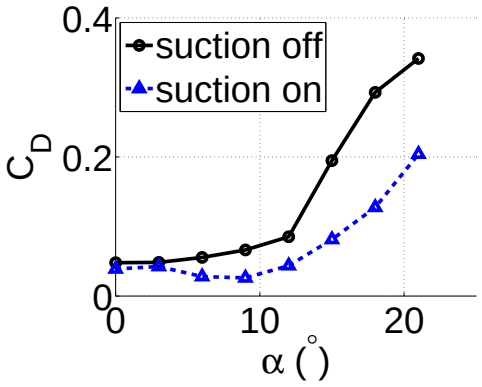


(d) S814, Re=$3.3 \times 10^5$

Figure 3.26: Wake velocities and $C_D$ for constant suction

increased steadily beyond 10° and reached 0.3 at an angle of attack of 20°. When suction was applied, $C_D$ reduced by up to 30% for angles of attack of less than 10°. For angles of attack between 10° and 18°, $C_D$ decreased as compared to the values less than 10°. As compared to the non-suction case, $C_D$ decreased by up to 80% for angle of attack of 18°. For an angle of attack of 21°, which is greater than the stall angle, $C_D$ was similar for suction and non-suction case.

Figure 3.26(d) shows the $C_D$ values for S814 profile for Re=$3.3 \times 10^5$. $C_D$ increased at a slow rate from 0.05 to 0.09 between 0° and 12°. The slope increased for angles of attack greater than 12° and $C_D$ was 0.34 for angle of attack 21°. On applying suction, $C_D$ reduced for all angles of attack till 21°. The maximum change in $C_D$ was for angle of attack 15°, with the drag reducing by 59%.

Thus, it was observed that the drag coefficient decreased for all angles of attack on application of suction. The decrease in drag is expected to increase the efficiency of a

wind turbine.

### 3.3.7 Effect of varying suction

In this section the effect of varying $C_\mu$ on $C_L$ and $C_D$ is examined. For constant $Re$, $C_L$ monotonically increased, and $C_D$ monotonically decreased with increase in $C_\mu$

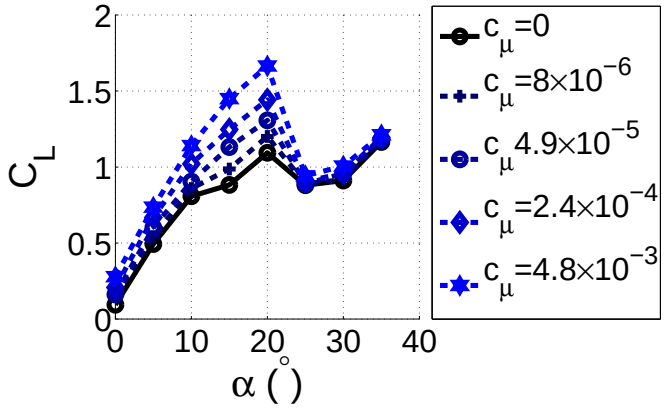


(a) S814, $\alpha = 0° - 35°$

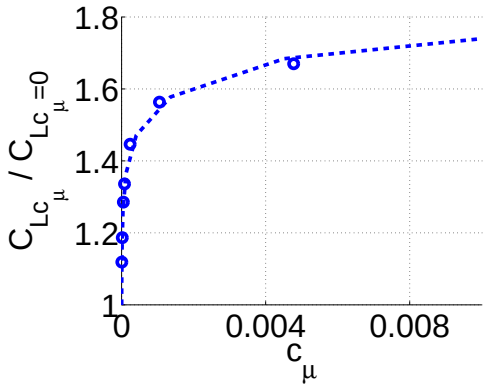


(b) S814, $\alpha = 15°$

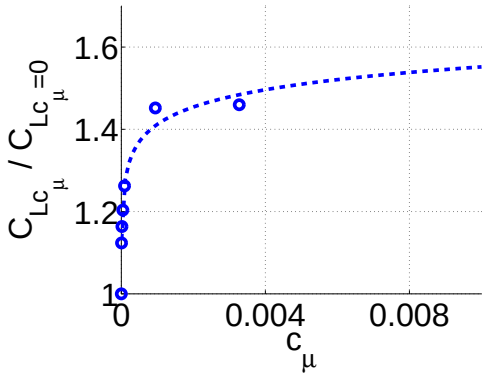


(c) NACA0012, $\alpha = 15°$

Figure 3.27: $C_L$ improvement, varying suction ($C_\mu$), $Re = 3.3 \times 10^5$

Figure 3.27 shows the variation of $C_L$ for $Re = 3.3 \times 10^5$ and varying $C_\mu$ For the S814 aerofoil, $C_L$ is shown for no suction and increasing magnitudes of suction in figure 3.27(a). The angle of attack varies from 0° to 35° at 5° intervals. $C_L$ increased for all angles of attack with increase in $C_\mu$. The improvement in lift coefficient was significant for the angle of attack less than the stall angle, with the $C_L$ increasing by more than 60% at $\alpha = 20°$ for maximum suction. Post stall, there was no significant improvement in the lift coefficient.

Figures 3.27(b) and 3.27(c) show the increase in $C_L$ over a no-suction case for varying values of $C_\mu$ for aerofoil profiles S814 and NACA0012 respectively. The Re was $3.3 \times 10^5$ and the angle of attack was 15°. The ratio of $C_L$ with suction over the non-suction $C_L$ is marked as a circle in the graph. A semi-log fit has been plotted along with the points to show the relationship between the increase in $C_L$ and $c_\mu$. For both aerofoil profiles, NACA0012 and S814, the improvement in lift increased sharply with an increase in $C_\mu$ close to 0. The slope decreased with an increase in $C_\mu$ and displayed an asymptotic behaviour for larger values of $C_\mu$. For S814, the maximum increase in $C_L$ was over 65% and for the NACA0012 profile, the increase was 45%. The equations for the semi-log fit for the aerofoils S814 and NACA0012 are:

$$\frac{C_{Lc_\mu}}{C_{LC_\mu=0}}_{\text{S814}} = 0.0886 \times \log(C_\mu) + 2.164 \tag{3.9}$$

$$\frac{C_{Lc_\mu}}{C_{LC_\mu=0}}_{\text{NACA0012}} = 0.0607 \times \log(C_\mu) + 1.831 \tag{3.10}$$

Figure 3.28 shows the variation of wake velocities and $C_D$ with change in $C_\mu$. The aerofoil profile was NACA0012, $Re = 1.6 \times 10^5$ and $\alpha = 9°$. $C_\mu$ varied from 0 to 0.014. The deficiency in velocity in the wake was maximum for no-suction (Figure 3.28(a)). With an increasing $C_\mu$, both, the maximum velocity deficit and wake width decreased. The resulting $C_D$ is shown in figure 3.28(b). For no-suction, the $C_D$ is close to 0.05, and decreased sharply with an increase in $C_\mu$ close to 0. With a further increase in $C_\mu$, the slope reduced. For $C_\mu = 0.0147$, $C_D$ decreased by 80%.

Figures 3.28(b) and 3.28(c) show a semi-log fit between $C_D$ and $C_\mu$ for the aerofoil profiles NACA0012 and S814 respectively. Equations 3.11 and 3.12 are the respective relations.

$$\frac{C_{DC_\mu}}{C_{Dc_\mu=0}}_{\text{NACA0012}} = -0.105 \times \log(C_\mu) - 1.986 \tag{3.11}$$

$$\frac{C_{Dc_\mu}}{C_{Dc_\mu=0}}_{\text{S814}} = -0.0623 \times \log(C_\mu) + 0.4390 \tag{3.12}$$

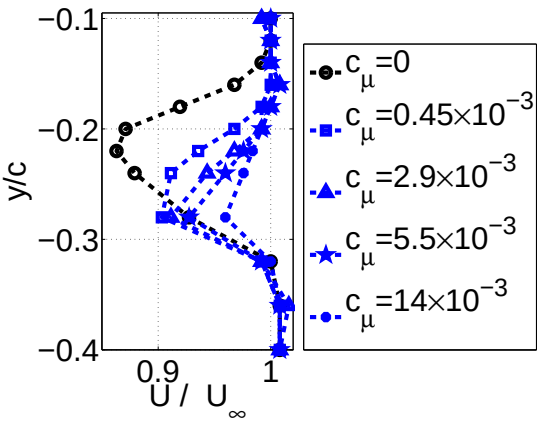


(a) Wake velocities

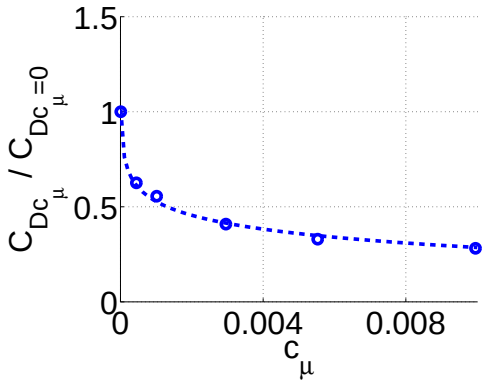


(b) $C_D$ vs $C_\mu$, NACA0012

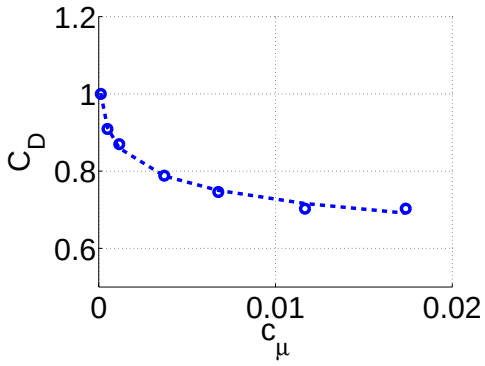


(c) $C_D$ vs $C_\mu$, S814

Figure 3.28: Wake velocities and $C_D$ for varying $C_\mu$, $Re = 1.6 \times 10^5$, $\alpha = 9°$

### 3.3.8 Validation of the experimental set-up

In order to ensure that the experimental set-up produced reliable data, the measurements from the the experimental set-up were compared with those reported in literature. Specifically, experimental lift curves obtained for the NACA0012 aerofoil were compared with those of Sheldahl and Klimas [SP81].

Figure 3.29 compares the lift coefficients for NACA0012 aerofoils for the wind tunnel experiments in the $Re$ range $1.6 \times 10^5$ - $4.9 \times 10^5$ with Sheldahl and Klimas' experiments at $Re$ between $1.6 \times 10^5$ and $7 \times 10^5$. The following salient observations were made.

i The trends for the measured values of $C_L$ matched well with those obtained by Sheldahl and Klimas [SP81].

ii The slope remained constant in the angle of attack range until stall, for the measured $C_L$, as well as for Sheldahl and Klimas [SP81]. However, the slope for the measured

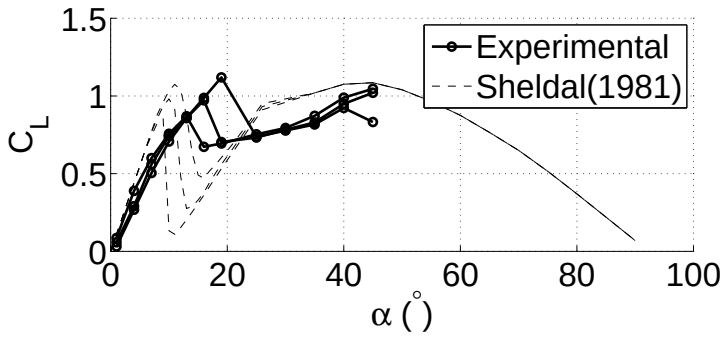


Figure 3.29: Lift curves for NACA0012

$C_L$ was observed to be lesser than that reported by Sheldahl and Klimas.

iii The maximum $C_L$ is consequently lesser that that reported by Sheldahl and Klimas [SP81]. This may be because of the secondary separation and the development of a stream-wise vortex at relatively large angles of attack.

iv It may be noted that this discrepancy does not affect the analysis in the following Chapter, since the objective of the present work is to estimate the difference in the power output of a turbine by the application of suction. Thus, the focus of the experimental part of this thesis is to characterise the difference in the aerodynamic characteristics of the aerofoils with and without suction.

v The measured as well as Sheldahl and Klimas' [SP81] stall angle increases with an increase in the $Re$.

vi For angles of attack greater than the stall angle, the measured $C_L$ decrease significantly, then increase again with increase in angle of attack, with the curves for different $Re$ remaining close to each other.

Swalwell et al. [SSM01] had conducted tests on a NACA0021 aerofoil profile in the same wind tunnel at Monash University and concluded that increase in turbulence delayed the stall, which is consistent with the experiments in this thesis. The turbulence intensities were 6.5%, 1.4%, 1.3% and 1.1% for $Re$ $8.2 \times 10^4$, $1.6 \times 10^5$, $3.3 \times 10^5$ and $4.9 \times 10^5$, respectively. The stall angles for these $Re$ were 13°, 12°, 15° and 18°, respectively. The turbulence intensities for the higher three $Re$ were close to each other, and the stall angle increased with an increase in the $Re$. For $Re = 8 \times 10^4$, the turbulence intensity was $\sim 4$ times higher. Consequently, the stall angle was higher than that expected, that

is, 13° for turbulence of 6.5, than 9° for expected turbulence intensity of $\sim 1.5$. This is consistent with Swalvel's [SSM01] results.

## 3.4 Dynamic tests

This section is aimed at capturing the dynamic mathematical model associated with active surface suction over the aerofoils. This dynamic model reveals the temporal limits of surface suction, for a given $Re$ - $C_\mu$ combination, that is, it says how fast flow control can change $C_L$ and $C_D$, for the given combination. To obtain such a dynamic model, with $C_\mu$ as input and $C_L$, $C_D$ as outputs, a system identification technique was used on the empirically-obtained input-output data from 'transient' experiments, which are explained in this section.

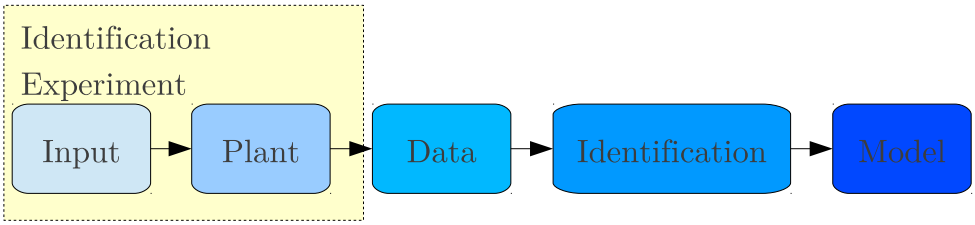


Figure 3.30: System identification of a dynamic system

System identification refers to building mathematical models of dynamic systems from measured data (Figure 3.30). (Refer to Sections 2.6 and 2.7 for an introduction on dynamic systems and system identification, respectively.) To generate and gather relevant data, special experiments are required to be designed to excite all relevant modes of the system. In the subsequent experiments, it was aimed to change the input, $u$, in a step-function, in order to excite all frequencies in output, $y$, as, in the frequency domain, step-function can be represented as the sum of all frequencies.

The experiments were conducted on NACA0012 aerofoil profile. The output of the system, $y$ was taken as the surface pressure on the leading edge, since surface pressure determines the relevant aerodynamic characteristics of the aerofoil. The input to the system, $u$ was taken as the pressure difference of the two pressure taps in the Venturi tube, as this relates to the mass transfer and thus the suction effort. The experimental schematic for the dynamic tests is shown in Figure 3.31.

Towards identifying the dynamic map between $u$ and $y$, a black-box approach was

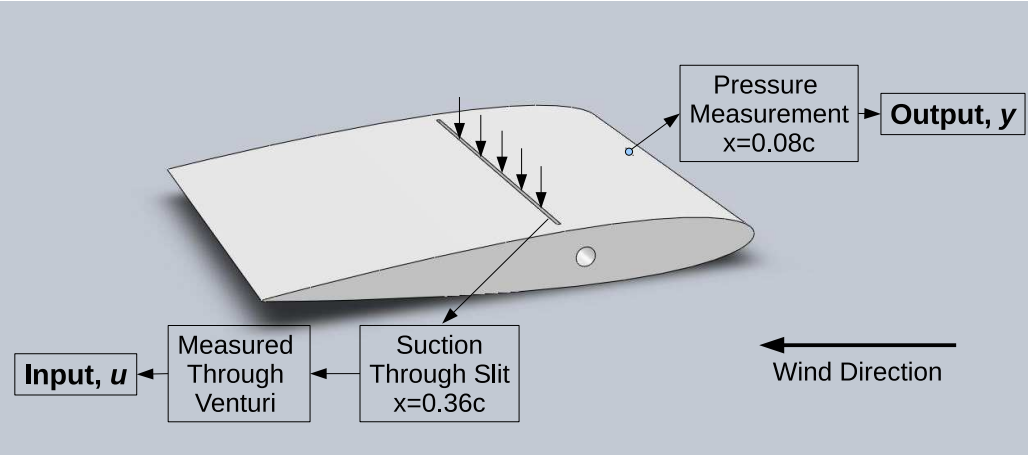


Figure 3.31: Experimentation schematic for system identification

used [Lju98]. It was observed that the relation between $u$ and $y$ was non-linear. Further, $\Delta y$ was depended on the operating value of $u$ and $\Delta u$ given to the plant, for all other physical factors remaining constant, which included angle of attack, wind speed, etc. Due to this specific non-linear nature of the relationship between $u$ and $y$, it was necessary to identify a set of linear time invariant (LTI) models (refer to Section 2.6.1) whose parameters were dictated by the operating $u$ (Figure 3.32(b)). A 'piecewise linearisation' approach was used, to compartmentalise the dynamic map into locally valid LTI models (refer to Section 2.7.2).

Several small changes to $u$ ($\Delta u$) were given and corresponding changes in $y$ ($\Delta y$) were recorded for different operating values of $u$. The structure of the said linear dynamics was assumed to be captured by the ARX model [Lju98] (Section 2.7.1). These LTI models (Figure 3.32(b)) were put together to create a linear parameter varying model (Figure 3.32(c)) to predict the value of $y$ for the whole operating range of $u$.

### 3.4.1 Choice of variables

**Input**: The 'input' of interest ($u$) was the volumetric flow rate of the air drawn from the surface of the aerofoil. This was achieved through the suction slit on the surface of the aerofoil at a distance of $0.36c$ from the leading edge. The volumetric flow rate through this slit was estimated using a venturi tube. The estimate of the volumetric flow rate is calculated using the following relation:

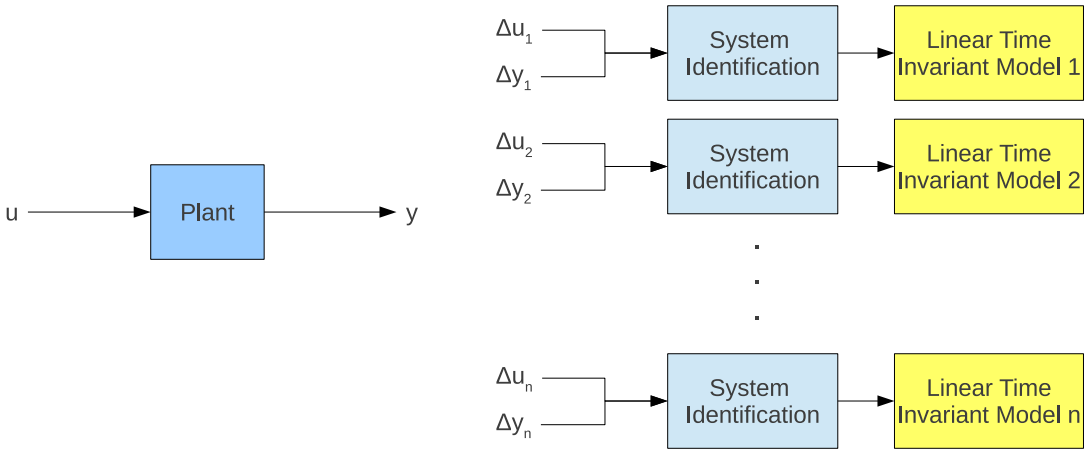


(a) Plant

(b) Identified LTI models

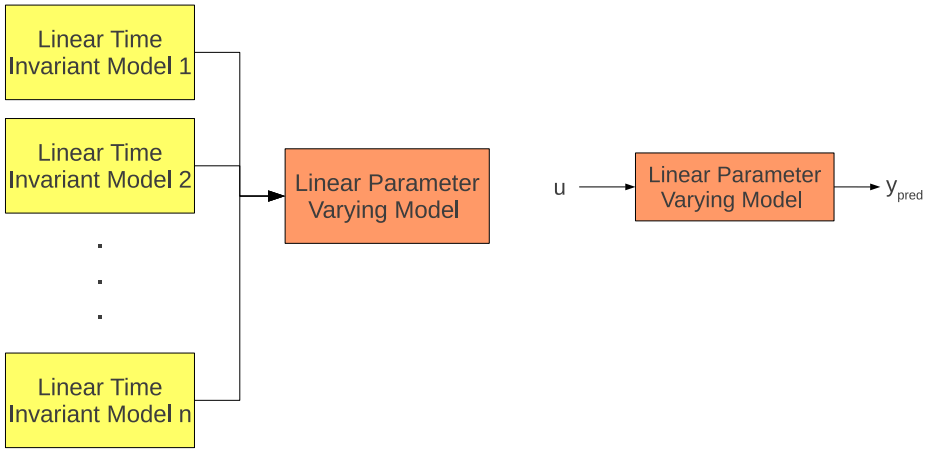


(c) Combination of LTI models into LPV model

(d) Predictions of LPV model

Figure 3.32: System identification schematic

$$Q = Area_1 \sqrt{\frac{2}{\rho} \cdot \frac{(p_1 - p_2)}{\left(\frac{Area_1}{Area_2}\right)^2 - 1}} \tag{3.13}$$

where $Area_1$ and $Area_2$ are the areas at the two measurement positions in the venturi tube, and $p_1$, $p_2$ are the pressures at the respective positions (Figure 3.7). In the equation 3.13, the parameters of the venturi tube remain constant, and the variables are $p_1$ and $p_2$. The flow rate particularly depends on the difference of these pressures, $p_1 - p_2$. Thus, the input variable $u$ has been taken as this difference:

$$u = p_1 - p_2 \tag{3.14}$$

These pressures were sampled using Turbulent Flow Instrumentation's Dynamic

Pressure Measurement System (DPMS) [Tur13] pressure transducers at a sampling frequency of $1000Hz$. The standard deviation for the value of $u$ lies between $5Pa$ and $10Pa$ for operating values of $u$ varying between $0Pa$ and $200Pa$, respectively.

**Output**: The 'output' of interest ($y$) was the pressure over the surface of the aerofoil. More specifically, at a distance of $0.08c$ from the leading edge. The motivation for choosing surface pressure stems from the fact that Lift and Drag, the performance characteristics of an aerofoil can be calculated using the pressure distribution (or, non dimensional $C_{Pressure}$) around the aerofoil:

$$C_N = \sum_{Suction\,Surface} C_{Pressure}\frac{\Delta x_i}{c} - \sum_{Pressure\,Surface} C_{Pressure,i}\frac{\Delta x_i}{c} \tag{3.15}$$

$$C_T = \sum C_{Pressure,i}\frac{\Delta y_i}{c} \tag{3.16}$$

$$\begin{bmatrix} C_L \\ C_D \end{bmatrix} = \begin{bmatrix} \cos\alpha & -\sin\alpha \\ \sin\alpha & \cos\alpha \end{bmatrix} \begin{bmatrix} C_N \\ C_T \end{bmatrix} \tag{3.17}$$

Thus, pressure over the surface of the aerofoil was taken as the output, $y$. Since the leading edge of an aerofoil produces the maximum lift force, the surface pressure at the leading edge (at a distance of $0.08c$ from the leading edge) was chosen as the output for system identification, in order to maximise signal-to-noise ratio. $\Delta y$ was taken as the change from the equilibrium pressure for the initial conditions:

$$\Delta y = P_{surface} - P_{surface,equilibrium} \tag{3.18}$$

The surface pressure was measured using a tap on the aerofoil, which was connected to the Turbulent Flow Instrumentation's Dynamic Pressure Measurement System pressure transducer using a $1.1m$ long silicon tube with an internal diameter of $1mm$. An appropriate transfer function for the tubing was input to the transducer to account for the dynamics introduced by the tubes. The sampling frequency was $1000Hz$.

### 3.4.2 Tests conducted

The tests were divided into two parts, one for gathering data for identification, and other for validation of the models built. The identification and validation tests were done on different dates, and the set up was dismantled and assembled again between these tests.

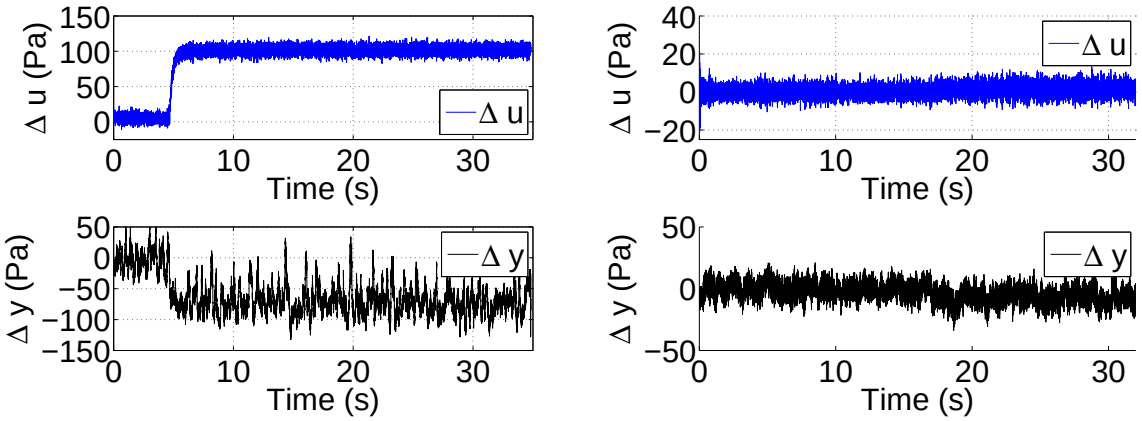


(a) Large-step test, with large change in $\Delta u$ from $u_{initial} = 0$

(b) Small-step test, with small change in $\Delta u$, $u_{initial} \neq 0$

Figure 3.33: Identification test types

For **identification**, the step tests were conducted at all four wind speed $20m/s$, that is, $Re = 3.3 \times 10^5$ and angle of attack of 10°. Suction pressure, $u$ was changed from the initial value to the final value in varying step sizes. Since the pressure over the aerofoil was lower than the static in the wind tunnel, the values of $y$ were negative. With suction control, that is, positive $u$, the pressure over the aerofoil reduced further. Hence, $y$ and $\Delta y$ were negative for positive $u$ and $\Delta u$. Two types of tests were conducted for identification:

i Large-step, with $u$ changing in a step from an initial value of $0Pa$ to various final values, the maximum being close to $200Pa$. This was done to identify steady state characteristics of suction control. Figure 3.33(a) shows the temporal variation of surface pressure, $y$ with a typical large-step change in $u$. Table 3.7 documents the steady state values of $\Delta y$ with the steady state values of $\Delta u$ for these tests. The steady state value of $\Delta y$ was found to vary non linearly with the steady state value of $u$. The incremental effect of suction was maximum at lower $u$, and the gains per unit $\Delta u$ diminished as $u$ increased.

ii Small-step, with $u$ changing from a non-zero initial value to a final value in a small step. This was done to compartmentalise the characteristics of the suction model into various small linear regions. (Refer to Section 2.7.2 for discussion on piecewise linearisation). Figure 3.33(b) shows the typical response of such a test. It was observed that for same $\Delta u$, $\Delta y$ was larger for smaller values of operating $u$. Table

Table 3.7: Tests for Identification

| | Large-step | | | Small-step | | |
|---|---|---|---|---|---|---|
| No. | $u_{initial}$ | $\Delta u$ | $\Delta y$ | $u_{initial}$ | $\Delta u$ | $\Delta y$ |
| 1 | 0 | 5.5 | -26.2 | 0.4 | 1.2 | -1.7 |
| 2 | 0 | 10.3 | -30 | 7.2 | 5.7 | -6.8 |
| 3 | 0 | 20.1 | -37.3 | 9.3 | 7.1 | -6.5 |
| 4 | 0 | 40.3 | -42.9 | 15.1 | 12.1 | -7.1 |
| 5 | 0 | 58.7 | -48.5 | 20.3 | 16.2 | -0.8 |
| 6 | 0 | 80.2 | -63.2 | 32.7 | 26.6 | -5 |
| 7 | 0 | 98.6 | -68.4 | 46.4 | 37.3 | -5.6 |
| 8 | 0 | 130.4 | -77.2 | 70.1 | 56.1 | -5.4 |
| 9 | 0 | 166.5 | -87.6 | 89.8 | 73.1 | -8 |
| 10 | 0 | 201.3 | -88 | 112.8 | 90.8 | -8 |

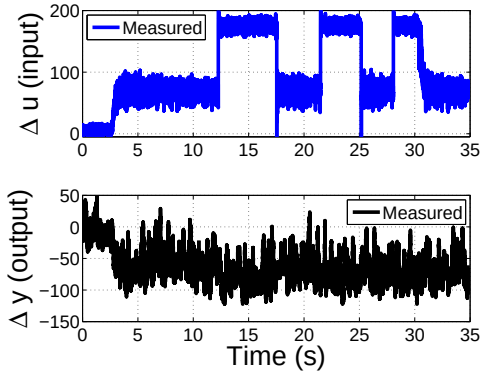


Figure 3.34: Validation test

3.7 documents these $\Delta u$ and $\Delta y$ values.

For **validation**, of the models, similar tests were conducted on the same set-up, albeit at a different time, to collect a separate set of data for validation. These tests were conducted for 35 seconds and multiple changes to the input were given for the duration of the tests. The range of $u$ was not restricted, that is, no small-step change assumption was made. The $u$ of these tests was input to the Linear Parameter Varying model, to find the $y_{predicted}$. The $y_{predicted}$ thus obtained was compared with the actual output of the plant ($y_{actual}$) from the validation tests. Figure 3.34 shows the input and output of one of the validation tests.

### 3.4.3 System identification

This section details the process of identifying the plant characteristics from the captured $u$ and $y$ data. Figure 3.32 shows a schematic of the process followed to arrive at the final Linear Parameter Varying (LPV) model.

Multiple Linear Time Invariant (LTI) models were identified by giving small $\Delta u$ inputs for $u$ varying from $0\,Pa$ to $200\,Pa$. (Figure 3.32(b)). The values of $\Delta y$ were recorded for these values of $\Delta u$. Filtering and parametric identification were done using a discrete algorithm, ARX (AutoRegressive with eXogenous input), which provides a fast and efficient solution by means of a least squares approach [Lju98] (see Section 2.7.1). The LTI models thus obtained were of the form:

$$A(z)y(t) = B(z)u(t) + e(t) \tag{3.19}$$

*where*

$$\begin{aligned} A(z) &= 1 + A_1 z^{-1} + A_2 z^{-2} \\ B(z) &= 1 + B_1 z^{-1} \end{aligned} \tag{3.20}$$

for a second order system, with *forward shift operator, $z$*

$$zu(t) = u(t+1) \tag{3.21}$$

and *backward shift operator, $z^{-1}$*

$$z^{-1}u(t) = u(t-1) \tag{3.22}$$

and noise component $e$.

Since the flow control involves removal of mass from the fluid, and the governing equations of the motion of fluid, the Navier-Stokes equation are second order; the characteristics of the identified system were assumed to be second order or higher. A second order system was found to capture the dynamics of the system well. With third order and higher systems, there was no significant benefit in prediction, that is, no significant change in standard deviation of $\Delta y_{predicted} - \Delta y_{actual}$ was observed. Both, second order and third order identified systems had a dominant pole close to 1 on the real axis. Thus,

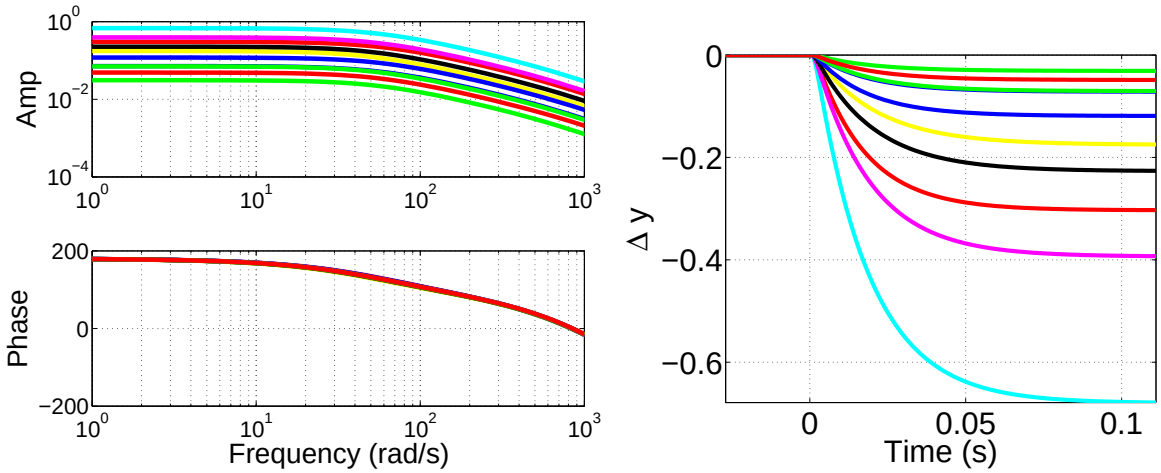


(a) Bode plots for LTI models identified from small-step tests

(b) Unit step responses for LTI models identified from small-step tests

Figure 3.35: Properties of the LTI models identified through small-step tests

the predictions with the third order system were similar to the ones with the second order system. Hence, second order ARX was used throughout the identification process.

The ARX algorithm was used on 10 sets of $\Delta u$ and $\Delta y$ for small-step tests at wind speed $20m/s$ and 10 LTI models were obtained. The output was assumed to lag the input by 1 sample time. Hence, one previous value of input, that is, $u(t-1)$ was used in the model. The second order model implies that two previous values of output, $y(t-1)$, and $y(t-2)$ were used. Table 3.7 shows the operating $u$ and $\Delta u$ for the tests.

Figure 3.35(a) shows Bode plots for these LTI models. The phase difference for all the linear models remained the same over the whole frequency range. The trends of amplitude too remained the same over the frequency range, however the absolute amplitude varied with the operating $u$. This indicates that the structure of the linear models remains the same for all operating $u$s, but the steady state gain varies with the regime of the operating $u$. The same inference can be drawn from the pole-zero map. The dominant poles for all 10 linear models are close to 1. Their values range from 0.976 to 0.983. The higher frequency poles for all ten of these models lie between 0.378 and 0.410. Since the respective poles of these models lie in the vicinity of each other, the response characteristics are expected to be similar, as predicted by the bode plots.

Figure 3.35(b) shows the step responses of these linear models to an input unit step at time $t = 0$. The predicted output is a typical over-damped second order response. The time constants of all the linear models were close to $0.02s$. The settling time was close to

Table 3.8: Identified Parameters

| No. | $u_{initial}$ | $A_1$ | $A_2$ | $B_1/\Delta u$ |
|---|---|---|---|---|
| 1 | 0.4 | 1.338 | -0.373 | -0.0035 |
| 2 | 7.2 | 1.354 | -0.387 | -0.0002 |
| 3 | 9.3 | 1.342 | -0.378 | -0.0014 |
| 4 | 15.1 | 1.337 | -0.371 | -0.0018 |
| 5 | 20.3 | 1.346 | -0.379 | -0.0006 |
| 6 | 32.7 | 1.340 | -0.370 | -0.0002 |
| 7 | 46.4 | 1.335 | -0.367 | -0.0002 |
| 8 | 70.1 | 1.325 | -0.361 | -0.0001 |
| 9 | 89.8 | 1.328 | -0.362 | -0.00003 |
| 10 | 112.8 | 1.323 | -0.357 | -0.00002 |

$0.1s$. These values are in the same order of magnitude as that obtained by Mouyon et al. in their suction-based flow control experiments on flat plate [MCSP98]. The amplitude of the steady state settling value, however, varied with the value of operating $u$ and $\Delta$u.

**Construction of the LPV model**

Table 3.8 shows the parameters of the linear models identified using the experimental data. The structure of the model is governed by $A_1$ and $A_2$ , while the steady state gain by $B_1$. From the bode plots, the pole-zero map and the step response it is expected that respective sets of $A_1$s and $A_2$s should be close to each other, and $B_1$s should vary according to $u$ and $\Delta u$. $A_1$ for these tests lies between 1.323 and 1.354, and $A_2$ lies between -0.387 and -0.337. The values of $B_1$ vary with both, $u$ and $\Delta u$. Here, the values of $B_1/\Delta u$ are presented. The values of $B_1$ were estimated using the large-step tests, because of ease of calculations, owing to lower observed noise-to-signal ratio, which may be due to large step change in $u$.

The linear models thus obtained were combined to construct the LPV model. The structure of the system was kept constant and the steady state gain was varied according to the operating $u$. The structure of the LPV system is governed by $A_1$ and $A_2$ , which were taken as the average of values in Table 3.8. The steady state gain is determined by $B_1$, changed according to operating $u$, and was looked up for each time step in the numerical prediction. The following equation gives the final LPV model:

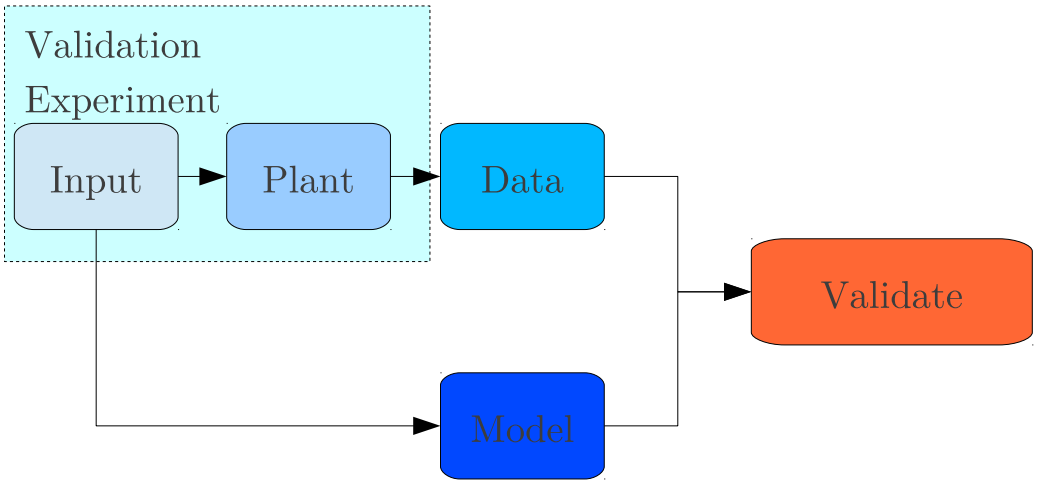


Figure 3.36: Validation Process

$$
\begin{aligned}
A(z)y(t) &= B(z)u(t) + e(t) \\
A(z) &= 1 + 1.3368z^{-1} - 0.3705z^{-2} \\
B(z) &= 1 + B_{lookup}\, z^{-1}
\end{aligned}
\tag{3.23}
$$

### 3.4.4 Validation of the models and prediction of output

Validation refers to the process of demonstrating that the identified model is a reasonable representation of the actual system. Refer to Section 2.7.3 for an introduction to the relevance of validation. Here, the output predicted ($y_{pred}$) was validated against the output of the plant ($y_{act}$).

Three validation tests are shown in Figures 3.37(a), 3.37(b) and 3.37(c). The measured plant input for each of the tests is shown in blue in the top figure. This signal was filtered and input to the LPV model (equation 3.23) as ($u_{fil}$) to obtain the output, $y_{pred}$.

A discrete-time numerical predictor was constructed in Matlab for the identified LPV model, whose inputs at time $t$ were - (1) previous time-value of $u_{fil}$ ($u_{fil}(t-\Delta t)$), and (2) previous time-values of $y_{pred}$ ($y_{pred}(t-2\Delta t)$ and $y_{pred}(t-\Delta t)$). The values of $A_1$ and $A_2$ were kept constant at 1.3668 and -0.3705, respectively and $B_1$ was read from the look-up table for each operating $u_{fil}$. $\Delta t$ was 0.001s, similar to sampling time in the experiments. The output of the predictor was current value of the output ($y_{pred}(t)$), which was stored as an array, for further predictions, and for comparing with measured output, $y_{meas}$.

$y_{pred}$ and $y_{meas}$ are plotted together in Figures 3.37(a), 3.37(b) and 3.37(c) . The

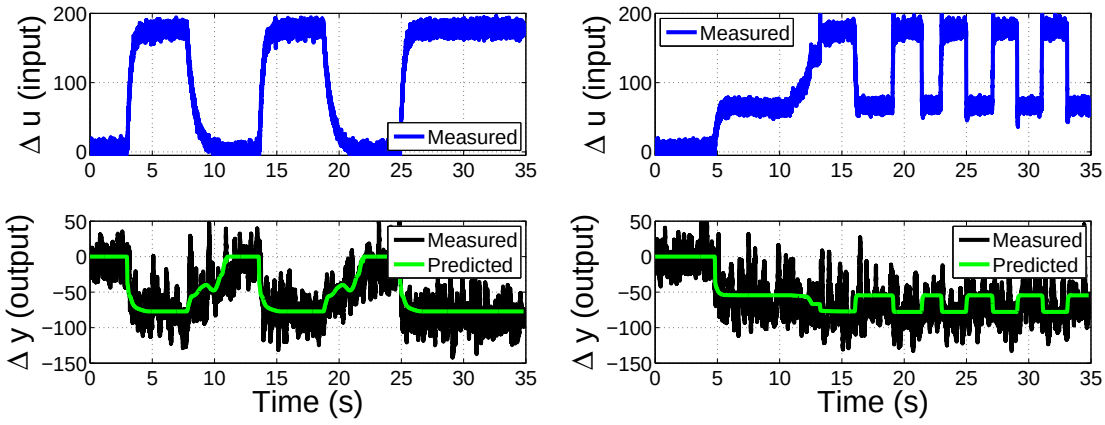


(a) Test no. 1

(b) Test no. 2

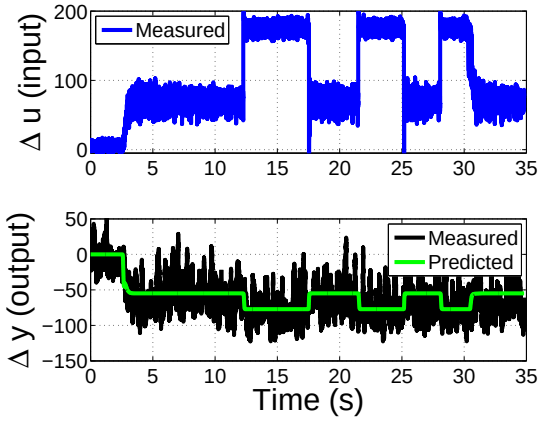


(c) Test no. 3

Figure 3.37: Measured inputs, measured outputs of the plant overlayed with predictions of the LPV model

measured output is shown in black in the figures, and the predicted output in green. It can be seen in the figures that the predictions of the LPV model match well with the measured output. This holds true for low operating values of $u$, high operating values of $u$, low rate of change of $u$ as well as high rate of change. Formally, the error, $\Delta y_{meas} - \Delta y_{pred}$ was measured, and the standard deviation of the error was compared with the standard deviation of $y$ around its mean for steady-state tests.

The standard deviation of error between $y_{pred}$ and $y_{meas}$ remains between 20 and 23, whereas, that of $y$ around its mean in steady wind varies between 18 and 36 for different angles of attack. These values of are close to each other, indicating that the LPV model described here is a reasonable representation of the plant.

Further, the time constant of the model is close to 0.02 seconds, that is, a natural frequency of $50Hz$, which is much higher than the frequencies associated with small wind

turbines (5-10$Hz$). Thus, the dynamic response of surface suction-based flow control should be adequate for compensating the dynamics of small wind turbines.

## 3.5 Summary

1. Experimental set-up

   (a) Two aerofoil profiles, NACA0012 and S814 were set up for experiments in wind tunnels. These aerofoils had a suction slit to draw the air into the aerofoil, in order to control boundary layer separation.

   (b) The $Re$ were kept between $2 \times 10^4$ and $4.9 \times 10^5$ by choosing appropriate chord lengths and wind speeds.

   (c) Time-averaged pressures were measured around the surface of the aerofoils, and the wind speed in the wake of the aerofoils, to calculate $C_L$ and $C_D$, respectively.

   (d) Temporal pressure measurements were set to be measured at a sampling frequency of $1kHz$, to be able to identify the system dynamics.

   (e) The $C_L$ and $C_D$ obtained from time-averaged tests were validated against the values in the literature.

2. Visualisation:

   (a) For the smoke visualisation tests, the streak-lines moved closer to the surface of the aerofoil, indicating inviscid layers moving closer to the surface, hence showing control of boundary layer separation.

   (b) The wool tufts realigned with the flow when suction was switched on, indicating attachment of the boundary layer with surface suction.

3. Surface pressures

   (a) The leading edge was effected the most on application of suction and the $C_{Pressure}$ decreased substantially when suction was applied.

   (b) Between the suction slit and the trailing edge, suction was able to prevent boundary layer separation for low angles of attack.

4. Lift Coefficients

   (a) The $C_L$ for pre-stall angles increased significantly on the application of suction.

   (b) The stall angle was delayed with the application of suction.

5. Drag Coefficients

   (a) The drag coefficient decreased for all angles of attack on application of suction.

6. Suction Momentum Coefficient

   (a) $C_L$ and $C_D$ was found to have a semi-logarithmic relation with $C_\mu$

7. Dynamic Tests

   (a) A second order ARX model was found to capture the dynamics of the system well while keeping the order of the dynamics small.

   (b) The locations of the poles of the dynamics identified were similar across the operating conditions.

   (c) The steady state gain was found to vary with the operating conditions.

   (d) Thus, a non-linear dynamic model (Linear Parameter Varying - LPV), as a system of local linear models, mapping suction pressure ($\Delta u$) to surface pressure ($\Delta y$) was constructed with a single dynamic structure and varying steady state gain.

   (e) The LPV model has a time constant close to 0.02s, that is, a natural frequency of around $50Hz$.

# Chapter 4

# Application of surface suction to small wind turbines

This chapter presents the simulations and their results, aimed at arriving at quantitative estimates of benefits of surface suction to small wind turbines based on the experimental results outlined in Chapter 3. The first section details the similitude argument extension of wind tunnel results to simulation of wind turbines operating in similar fluid dynamic regimes. The second section discusses Blade Element Momentum (BEM) method-based simulations, which estimate the entitlement to the increase in power output using surface suction over blades. The next two sections outline how mitigation of fatigue loads can be achieved using surface suction-based active-flow-control. The aero-elastic simulator, FAST has been used for these simulations. A summary of key simulation results is provided in the last section.

## 4.1 Using wind tunnel results for simulation in wind turbine simulations

Similitude argument analysis (Section 2.8.1) is used for facilitating correlation of experimental data, typically between what is seen in controlled environment testing vs what is seen during actual application. This section seeks to use the wind tunnel results obtained in Chapter 3, that is, the steady state relations between $C_L$, $C_D$ and $C_\mu$ (Equations 3.10, 3.9, 3.11 and 3.12) and the dynamic map between $C_L$, $C_D$ and $C_\mu$ (Equation 3.23), at

similar $Re$ and $C_\mu$ as the experiments in Chapter 3. In order for the argument that wind tunnel results should hold for the wind turbine simulations, the following criteria were satisfied:

1. *Geometric Similitude*: The wind tunnel tests were conducted on the same aerofoil profiles that are used in simulations, that is, NACA0012 and S814. High Impact Polystyrene (HIP) sheet was used to fabricate the aerofoil profiles. HIP has surface roughness close to that of glass fibre composites, which is a common material for the manufacture of wind turbine blades.

2. *Kinematic Similitude*: Blade Element Momentum theory (Section 2.2.1) assumes a two-dimensional flow over the blade elements, that is, there is no radial flow over the elements. For the wind tunnel experiments, end-plates were used to achieve a near two-dimensional flow (For details refer Section 3.2.3).

3. *Dynamic Similitude*: There are two involved aerodynamic phenomena:

   - flow over the aerofoil, characterised by Reynolds number ($\rho VL/\mu$)
   - withdrawal of air through the suction slit, characterised by the Coefficient of Momentum ($C_\mu$).

   The Reynolds numbers and Coefficient of Momentum for the simulations are kept close to the range of the experiments, that is, between $10^4$ and $10^5$, and $< 0.02$, respectively.

The results of interest for the aerodynamic simulations are - change in $C_L$ and $C_D$ with $C_\mu$, and the involved dynamics. The following section presents BEM simulations which estimate the entitlement to increase in power output of a small wind turbine. This is a steady-state analysis, hence it uses the relation between $C_L$, $C_D$ and $C_\mu$ without the dynamics involved. The next section simulates aero-elastic loads, and uses both, the relation between $C_L$, $C_D$ and $C_\mu$ and the involved dynamics, that is, the second order Linear Parameter Varying (LPV) model.

## 4.2 BEM simulations for power capture

This section quantifies the increase in entitled power output of a small turbine incorporating surface suction-based flow control on its blades.

### 4.2.1 Turbine characteristics

For the BEM based power capture analysis, a horizontal axis small wind turbine with the parameters described in Table 4.1 is considered. The number of blades, $N$ is 3. The aerofoil profile used is NACA0012. The radius is assumed to be $2m$. The chord length varies linearly from $150mm$ at the root to $75mm$ at the tip. The blade twist angle similarly varies from 12° at the root to 0° at the tip. The wind speed is assumed to be constant at $7.5m/s$. The rotational speed of the turbine is varied from $107RPM$ to $358RPM$ to vary the tip speed ratio from 3 to 10. Tip speed ratio ($\lambda = \Omega R/U_\infty$) is defined as the ratio of the rotational speed of the tip of a blade and the wind velocity.

Table 4.1: Small wind turbine parameters for BEM based power capture study

| Parameter | Value |
|---|---|
| Number of blades(N) | 3 |
| Aerofoil Profile | NACA0012 |
| Radius | 2m |
| Chord Length (c) | 150mm (root) - 75mm (tip) |
| Blade Twist Angle | 12° (root) - 0° (tip) |
| Wind Speed ($U_\infty$) | $7.5m/s$ |
| Tip Speed Ratio ($\lambda$) | 3-10 |
| Suction Slit | 2mm wide, at 0.36c |

### 4.2.2 BEM Simulations

The software Windsim [(DU05] which incorporates the BEM relations from 2.3 to 2.15 is used for the simulations. The blade is divided into 10 regions. The value of axial flow factor, $a$ is found iteratively using the equation 2.11. The corresponding velocities at different radii are then calculated. Using these velocities and the corresponding chord lengths, the resulting Reynolds number for the blades are shown in Figure 4.1. These Reynolds numbers remain between $8.1 \times 10^4$ and $3.9 \times 10^5$, which is the range of Reynolds

numbers for experiments conducted in wind tunnel (see Section 3.2.1). Thus, using similitude argument, the $\Delta C_L$ and $\Delta C_D$ vs $C_\mu$ values can be used for these simulations, given $C_\mu < 0.02$

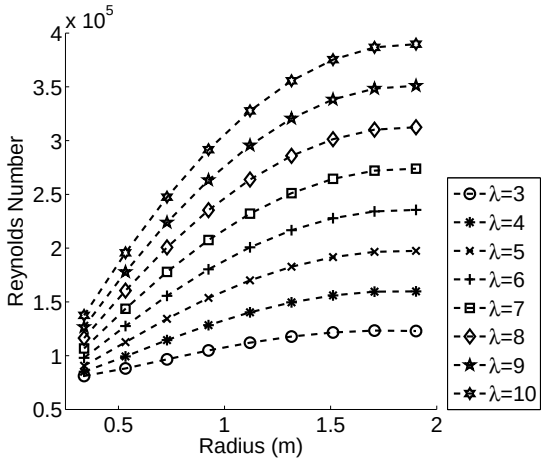


Figure 4.1: Reynolds Numbers for the Turbine Blade

The velocities thus obtained for each blade element are used to find the forces produced by the element. The coefficients $C_L$ and $C_D$ for NACA0012 were taken from Sections 3.3.5 and 3.3.6 and input to the software Windsim. For varying values of suction momentum coefficient, the corresponding values of $C_L$ and $C_D$ were given as inputs and the resulting values of $C_P$ were calculated. Equations 3.10 and 3.11 were used to model the relation between $C_L$ and $C_D$ and $C_\mu$.

### 4.2.3 Aerodynamic power output

Figure 4.2(a) compares the $C_P$ for varying $\lambda$ and applied $C_\mu$. As a general trend, for all values of $\lambda$, the $C_P$ increases with increase in $C_\mu$. This is to be expected, since $C_L$ increased, and $C_D$ decreased with increase in $C_\mu$ in the wind tunnel experiments. Thus, each element of the annular ring produces higher lift and lesser drag force. Hence, the torque produced, $\delta Q = N\delta r(\delta L \cos\phi - \delta D \sin\phi)r$ increased for all annular rings, resulting in increased power output, and thus, $C_P$.

Without applying flow control, for a steady wind speed of $7.5m/s$ for the $2m$ radius turbine described above, the maximum $C_P$ obtained is 0.235 at a tip-speed ratio, $\lambda = 6.6$. With increasing surface suction, the $C_P$ increased for all $\lambda$. The $\lambda_{opt}$ for $C_{Pmax}$ is also pushed towards the right. For $C_\mu = 4.6 \times 10^{-5}$, the $C_{P\,max}$ is 0.313 at $\lambda = 6.7$. With

increase in $c_\mu$ to $1 \times 10^{-4}$, $C_{P\,max}$ increases to 0.336 at $\lambda = 6.9$. For further increase in $C_\mu$ to $1 \times 10^{-3}$, the $C_{P\,max}$ is 0.403 and it occurs at $\lambda = 7.1$. For the maximum value of $C_\mu$=0.1, the $C_{p\,max}$ occurs at $\lambda = 7.5$ and reaches the value of 0.466.

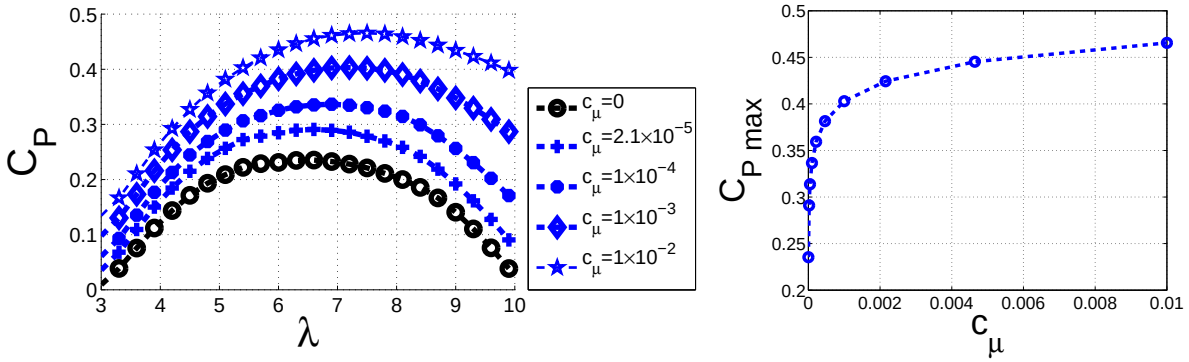


(a) $C_p$ vs $C_\mu$ (b) $C_{p\,max}$ vs $C_\mu$

Figure 4.2: $C_p$ enhancement for small wind turbines using constant surface suction

Figure 4.2(b) shows the relation of $C_{P\,max}$ with $C_\mu$. It ca be seen that this relation follows the law of diminishing returns. Closer to $C_\mu = 0$, $C_{p\,max}$ rises rapidly for small increase in $C_\mu$. For further increase in $C_\mu$, $C_{P\,max}$ shows and asymptotic behaviour and stabilises to a final value just above 0.45. It is worth noting that the operating $C_P$ of such a small wind turbine with active flow control matches the $C_P$ of those typically seen by large ($\geq 500kW$) wind turbines.

### 4.2.4 Power input for flow control

The power required for application of such flow control over the blades was calculated using suction momentum coefficient, $C_\mu$. Suction was assumed to be applied through a $2mm$ wide slit at all blade elements. The slit covered the whole span of the element and was assumed to be at $0.36c$ from the leading edge of the blade, similar to the wind tunnel experiments. For every blade element, the resultant relative wind speed was obtained from the simulations by Windsim. For the resultant wind speed over the blade element, the suction speed was calculated using the equation 3.8:

$$u_s = \sqrt{\frac{c_\mu c_r W_r^2}{w_{slit}}} \tag{4.1}$$

The consequent power ($\delta P_s$) of the air drawn into the blade at $\delta r$ is can be calculated by multiplying its kinetic energy with the rate of flow:

$$\delta P_s = 1/2\,\rho\,u_s^3\,w_{slit}\,\delta r \tag{4.2}$$

Thus the total power of the air drawn into the blades for the turbine is:

$$P_s = N \times \int_{r_{root}}^{r_{tip}} \delta P_s \tag{4.3}$$

The power output of the turbine and the power of the air drawn in is shown in figure 4.3. The power output of the turbines is 764W without applying suction. It rapidly rises to 1308W with suction power of 2.87W. The slope decreases with increase in suction power. For suction power of 106W, the output of the turbine is 1511W. Thus for an input power of 106W, the increase in output of the turbine is 747W.

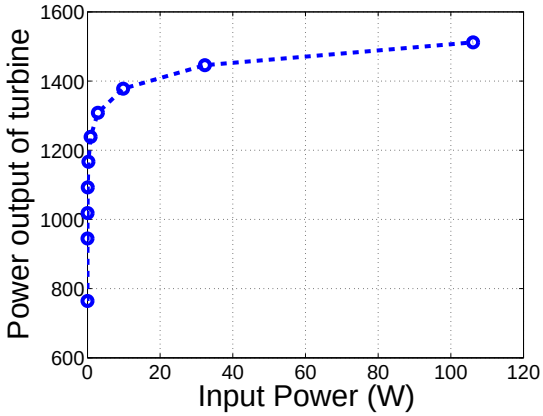


Figure 4.3: Power output vs suction power

The power required for suction calculated here is calculated as the kinetic energy per unit time of the air being drawn into the blades. It does not include the inefficiencies of the pump, the head losses in transmission and the effect of leakages etc. For eventual application, these factors will feature in the power requirement of the overall mechanism.

## 4.3 Aero-elastic simulations for load mitigation

In this section, surface suction-based flow control as a means to regulate rotor thrust and torque is looked at. As discussed earlier in Section 2.3, pitch control and generator torque control are the popular contemporary control techniques used in wind turbines. In Region II, generator torque ($Q_G$) is kept proportional to the square of rotational speed ($\Omega^2$) to maximise $C_P$ whereas in Region III, $Q_G$ and $\Omega$ are kept constant and the blades are

pitched to regulate the rotor torque in order to keep generator speed and torque constant, to produce constant power, and to keep the loads on the generator and turbine structure in the design limits.

Along with regulating power, active control can be utilised to reduce mechanical loads on the turbine and the tower. In unsteady and turbulent winds, the thrust seen by the turbine varies in proportion to the change in wind speed (Figure 4.4). This causes a fore-aft movement of the turbine, resulting in fatigue on the tower.

As discussed earlier in Section 2.3, pitching of blades can be used to regulate the thrust, and thus the fore-aft movement of the tower. Using pitching appropriately, the fore-aft movement of the turbine can be reduced, which would reduce the fatigue loads on the tower structure. This mitigation technique, however requires the blades to be pitched continuously over the whole revolution of the turbine. Thus, it is difficult to implement in small wind turbines as the rotational speeds of small wind turbines ($\sim 300-400$RPM) are significantly higher than those of large wind turbines ($\sim 10-30$RPM) [Woo11, BSJB01]. This is because, in order to operate at the optimum tip speed ratio ($\lambda_{opt}$), $\Omega$ has to increase because of the small size (small $R$) of the turbines. The higher rates of pitching angle and faster reversal of loads lead to larger size of pitching motor and increased fatigue load on the blade components, respectively.

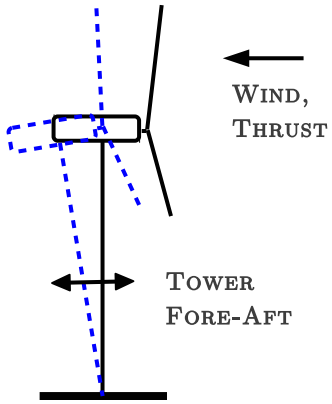


Figure 4.4: Fore-aft DoF of the tower

In this section, a novel method of fatigue load mitigation utilising surface-suction based flow control is proposed and tested. Similar to pitching of the blades, flow control can change the $C_L$ and $C_D$ , and thus, the thrust and torque produced by the turbine. By regulating thrust, the fore-aft movement, and hence, the fatigue loads on the tower can be mitigated. The essential difference between pitch control and flow control is that

pitching changes the operating angle of attack, whereas flow control endeavours to change the $C_L$ and $C_D$ characteristics while keeping the pitch angle constant (Fig. 4.5). As seen in Section 3.4.3, the time constant associated with suction in the $Re$ and $C_\mu$ combination $10^4$ - $10^5$ and $< 10^{-2}$, respectively is $0.02s$, that is, a natural frequency of $50Hz$, which is an order of magnitude higher than $5Hz$ of a small wind turbine (assuming operation at $300RPM$). Thus, flow control seems to have a prima facie advantage over pitching motor because of faster response.

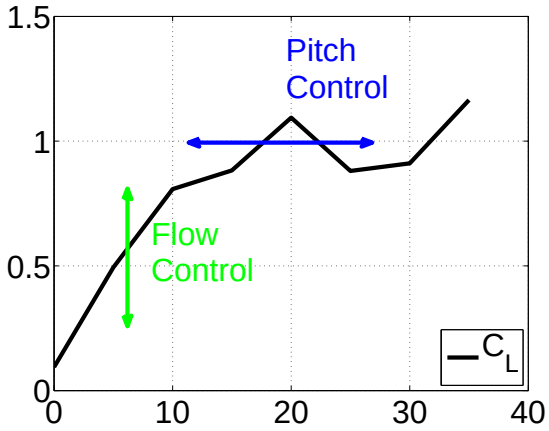


Figure 4.5: Actuation effects on $C_L$

In the following discussion, both – flow control and pitching techniques are utilised for fatigue mitigation, and compared with the baseline (without fatigue mitigation), and with each other.

### 4.3.1 Description of the control problem

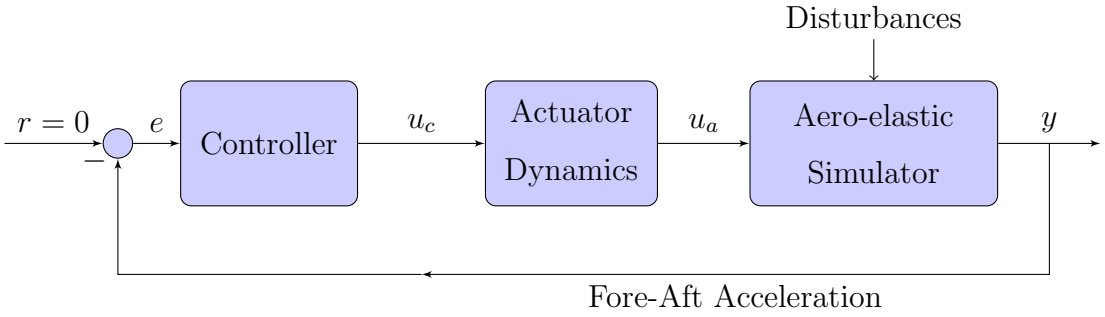


Figure 4.6: Schematic of control structure

The intent is to mitigate the fatigue loads in small wind turbines using flow control for actuation. The control scheme is illustrated in Figure 4.6. It is desired to have no

vibrations, that is, no tower-top acceleration, even in the presence of turbulent wind as described in Section 2.10. Hence, the reference input, $r$ is taken as 0 to find error, $e$. The plant here is a small wind turbine, simulated in FAST, and described further in Section 4.3.2. The plant, as simulated, has wind speed ($U_\infty$), generator loads, turbulence, yaw angle as inputs. The relevant outputs are power, structural loads, fore-aft acceleration, etc. Among these, tower top fore-aft acceleration was used as the only feedback variable to the control algorithm.

To regulate the fore-aft acceleration, the manipulated input is the change in $C_L$ and $C_D$ via changing suction, $C_\mu$. Appropriately using $C_\mu$ can regulate $C_L$ and $C_D$, which in turn control the forces produced by the blade elements, and thus net rotor thrust. As discussed in Section 4.3, thrust can influence the fore-aft acceleration. $C_L$ and $C_D$ can be varied by $\pm 10\%$ around their operating values as shown in Section 3.3.7. A Proportional-Derivative (PD) algorithm ($u = (K_P + \frac{K_D s}{1+\tau s})e$) is used to determine $C_\mu$ as a function of the feedback variable, tower-top fore-aft acceleration.

The active flow control actuation is also compared with control via pitch actuation. In effect, two actuation techniques are looked at, to achieve load mitigation in small wind turbines:

i *pitch control*, which changed the operating angle of attack of the aerofoils, e.g. right-left movement on the coefficient of lift ($C_L$) curve in Fig. 4.5.

ii *flow control*, which changed the coefficients of lift and drag ($C_L$ and $C_D$), e.g. shifting the $C_L$ curve up and down in Fig. 4.5.

### 4.3.2 Simulations

All simulations are performed using US National Renewable Energy Laboratory's (NREL) FAST simulator [JBJ05]. As discussed in Section 2.9, FAST is a comprehensive aero-elastic simulator which uses unsteady Blade Element Momentum (BEM) theory to model a turbine as a collection of rigid and flexible bodies in a spatio-temporal field of turbulent flow. The simulations have been performed on SWRT 10kW small turbine [CM05] with the specifications given in Table 4.2.

Table 4.2: Small wind turbine parameters for aeroelastic simulations

| **NREL SWRT turbine** | |
|---|---|
| Type | 3-bladed, upwind, variable speed turbine |
| Hub Height | $24m$ |
| Radius | $2.9m$ |
| Rated Wind Speed | $13m/s$ |
| Blade Nodes | 10 |
| Aerofoil Profile | S-814 |
| Pitching | Constant pitch for baseline and flow control cases<br>Simulink controlled for pitch control case |
| Flow Control | Surface suction based |
| Tower fore-aft mode | 1 |

Turbulent wind inputs of IEC class III A (see Section 2.10) were generated using NREL's TurbSim software [Jon09], a stochastic full-field inflow simulator. The power output of the turbine remained between $7kW$ and $9kW$. The blade was divided into 15 elements for the analysis. Flow control was applied to 10 elements closer to the root in the flow control case. The Reynolds numbers for these elements remains under $10^6$ during all simulations.

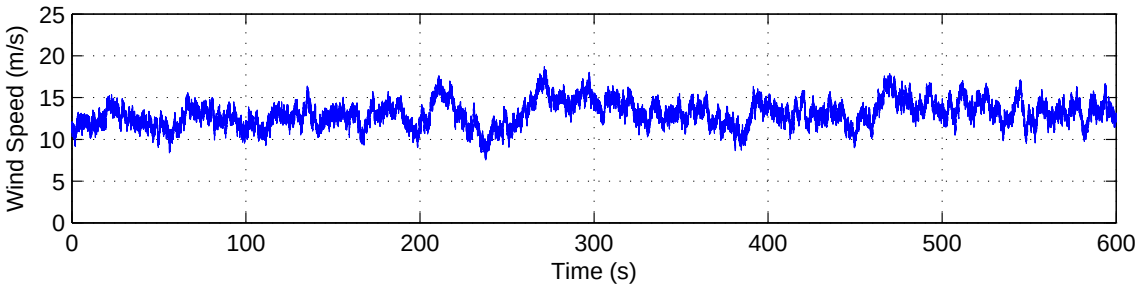


Figure 4.7: Sample wind input at hub height, mean speed 13m/s

### 4.3.3 Case I - baseline

The baseline case provided a benchmark to measure the perform ace of the control cases incorporation pitching and flow-control actuators. The program FAST provided by NREL was used as-is for these simulations. The input files to the program were configured to set the parameters for the blades, tower, generator etc. as described in Table 4.2. The

same input parameters were used for the control cases. The outputs of concern from the FAST simulator are tower-top fore-aft acceleration (for feedback); and tower-top fore-aft movement and tower-base out-of-the-plane bending moments (for bench-marking the control cases).

### 4.3.4 Case II - collective pitch control

As discussed earlier in Section 4.3, pitch control can be utilised to mitigate loads, along with regulating power of the turbine. In this section, we discuss the setting up of pitch control for mitigating loads.

To achieve pitch actuation, a motor mounted in the hub was assumed to provide the required torque. The motor was assumed to be connected to the individual blades with a gearbox of reduction 50. All three blades were pitched through the same angles. This method is called collective pitching of blades. The blades were pitched 'into stall' in order to reduce the actuation required [Bos00, BSJB01]. The motor was modeled as a second order system for the simulations with the parameters moment of inertia ($J_m$) $11.6 \times 10^{-6} kg\,m^2$, motor viscous friction constant ($B_m$) $1.15 \times 10^{-4}$, electro-motive force constant ($K_e$) $0.0261\,V/rad/sec$, electric resistance ($R$) $7.1\Omega$, electrical inductance ($L$) $0.265mH$ and friction torque ($M_\tau$) $0.99 \times 10^{-3}$.

The blade moment of inertia and aerodynamic loads were reflected on the motor through the gearbox. The actuation was saturated at $\pm 2^\circ$ change in blade pitch around the mean pitch angle for one revolution . The mean pitch angle was kept constant for the simulations as the mean wind speed did not vary significantly. The mean pitch angle, however, varied with mean wind speed according to the inbuilt power control strategy of the FAST simulator. Thus, different simulation runs had different mean pitch angles.

To apply pitch control in FAST, a modified version of SFunc Simulink model provided by NREL was used. Tower fore-aft acceleration from outputs of FAST simulator was taken as feedback. PD controller algorithm $(K_{P,P} + \frac{K_{D,P}\,s}{1+\tau s})$ was used to determine the change in pitch angle around the mean ($\Delta\beta$) to be used. $\tau$ was chosen as $150Hz$ to filter the high frequency noise. Since there are mechanical loads on the motor to achieve pitch control, and motor behaves as a second order system, another PD control algorithm $(K_{P,\beta} + \frac{K_{D,\beta}\,s}{1+\tau s})$ was used to decide the required motor torque. Thus, the motor torque was input to the FAST simulator and $\beta$ was used as the feedback for this inner loop. Fig. 4.8 shows the

corresponding block diagram for the complete control algorithm.

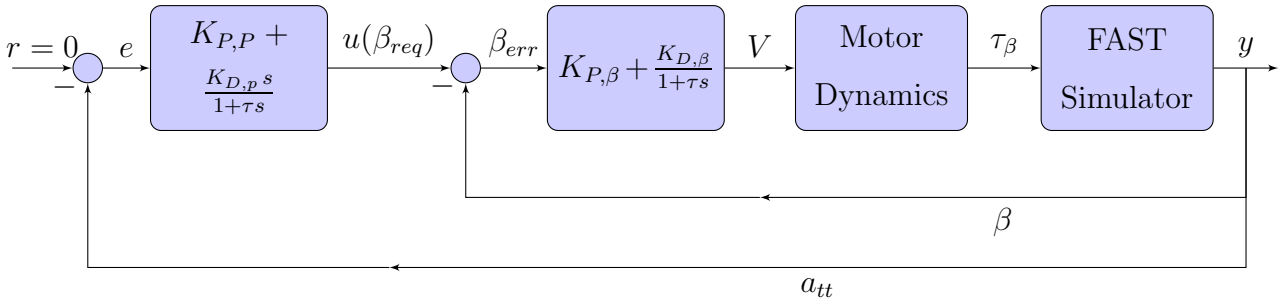


Figure 4.8: Schematic of control algorithm for pitch control

The input parameters given to the modified FAST simulator described above were the same as those given to the baseline case in Section 4.3.3. The outputs for comparison were also the same, that is, tower-top fore-aft movement and tower-base out-of-the-plane bending-moment.

### 4.3.5 Case III - flow control through surface suction

This section describes how the surface suction-based flow control was set up. Suction was assumed to be provided through a pump mounted in the hub. The three blades were provided with the same rate of flow. Over the blades, the air was drawn in trough a span-wise slit. The slit extended from the blade element closest to the root till the 10th element from the root. This covered 66% of the blade span. The Reynolds number for these blade elements remained under $8 \times 10^5$, which corresponds to the same order of magnitude of the wind tunnel experiments (see Section 3.2.1). These experiments indicate that the lift can be increased by up to 40% using suction. For the simulations, the maximum change in lift and drag was limited to $\pm 10\%$, such that the demanded $C_\mu$ remained within the range of the experiments.

Tower fore-aft acceleration was taken as the feedback variable. PD algorithm ($K_{P,F} + \frac{K_{D,F}\, s}{1+\tau s}$) was applied to reduce the fore-aft movement, which was the same as in the pitch control case. However, since there are no aerodynamic forces affecting the actuation like pitch control, the inner loop was not required for the flow control algorithm. The dynamics of the involved fluid dynamic phenomena, identified in Section 3.4, were incorporated into the control modules. These modules were added to the source code of the FAST simulator provided by NREL. On addition of these modules, the schematic of achieved flow control

was as shown in Figure 4.9.

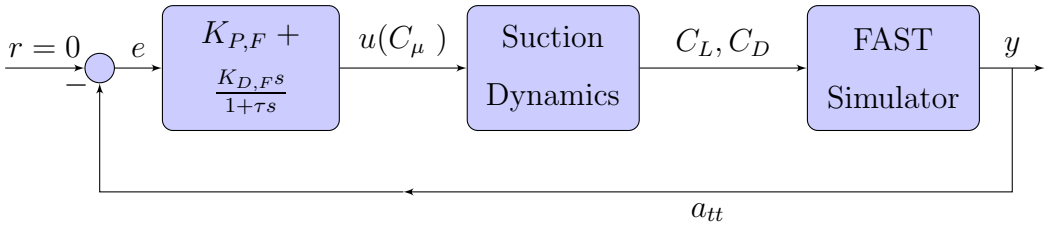


Figure 4.9: Schematic of control algorithm for suction control

The input parameters given to the modified FAST simulator described above were the same as those given to the baseline case and the pitch control case in Sections 4.3.3 and 4.3.4. The outputs for comparison were also the same, that is, tower-top fore-aft movement and tower-base out-of-the-plane bending-moment.

Table 4.3 gives a brief overview of the simulated control cases.

Table 4.3: Control cases

| | **Case I** Baseline | **Case II** Collective pitch control | **Case III** Flow control through suction |
|---|---|---|---|
| Turbine | SWRT (see Table 4.2) | SWRT | SWRT |
| Actuator | - | Pitching motor | Suction via vacuum pump |
| Feedback variable | - | Tower top fore-aft acceleration | Tower top fore-aft acceleration |
| Wind generation | Turbsim [JBJ05] | Turbsim | Turbsim |
| Wind class | IEC III A [Int08a] | IEC III A | IEC III A |
| Numerical computation | FAST [Jon09] | FAST interfaced with Simulink | Modified source code of FAST |

## 4.4 Aero-elastic simulation results

This section details the results of numerical simulations for the three cases described above. These simulations were done for two types of wind input:

i wind gust

ii turbulent wind

Wind gust exposes the turbine structure to extreme wind loads. These simulations are used to test the ultimate loading of the turbine. Turbulent winds expose the turbine to a spectrum of loads, which don't cause immediate damage, but over years cause fatigue damage to the structure.

### 4.4.1 Response to wind gust

Response of the turbine was tested for a turbulent wind gust (Extreme Operating Gust, $EOG_{1year}$). The gust is shown in Figure 4.10. The mean speed of the wind was $13m/s$ and the gust intensity was $8m/s$. The gust lasted from $21s$ to $29s$, that is, for 8 seconds. The turbulent wind input was generated using NREL's Turbsim [Jon09] software according to IEC III A Turbine Class wind.

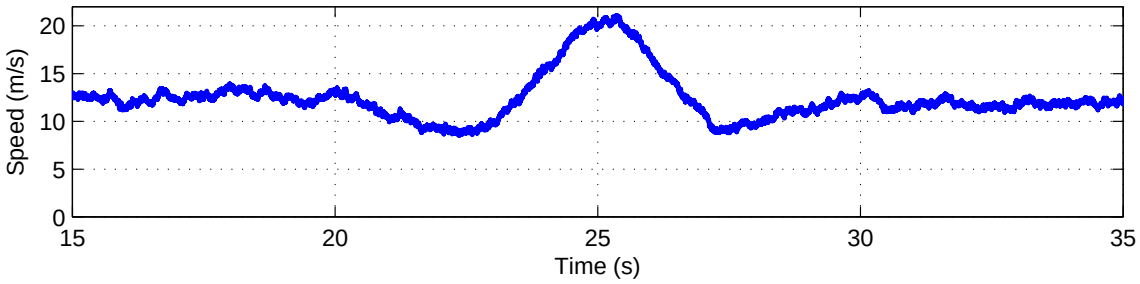


Figure 4.10: Wind gust, class IEC III A, intensity $8m/s$

The resulting tower top fore-aft movements for baseline, pitch control and flow control are shown in Figure 4.11. The movement before $21s$ corresponds to the turbine's response to the wind turbulence, whereas the between $21s$ and 29, it corresponds to the response to the gust, as well as wind turbulence.

It can be seen by eyeballing through the figure that the local peak-to-trough vibration of the tower around its moving-average position is reduced for both control cases over the baseline case – before, during and after the gust. The reduction is particularly noticeable in the graph between $21s$ and $22s$ as well as between $25s$ and $26s$. These time intervals correspond to reduction in the moving-time mean position, that is, when the tower moves forward.

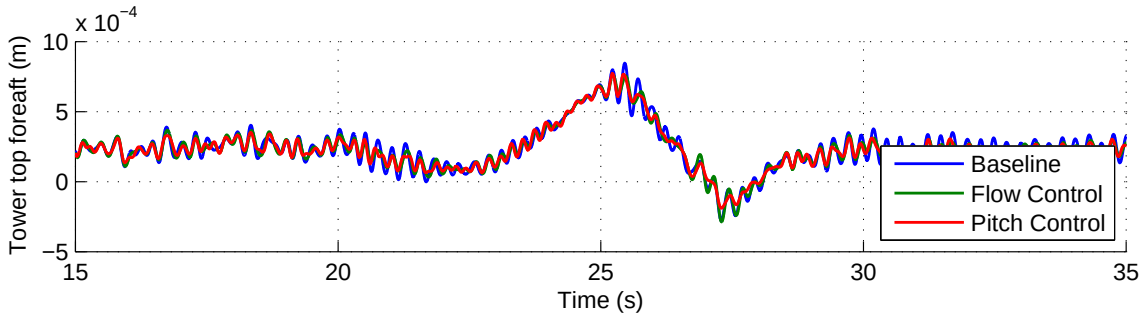


Figure 4.11: Tower top fore-aft movement in wind gust

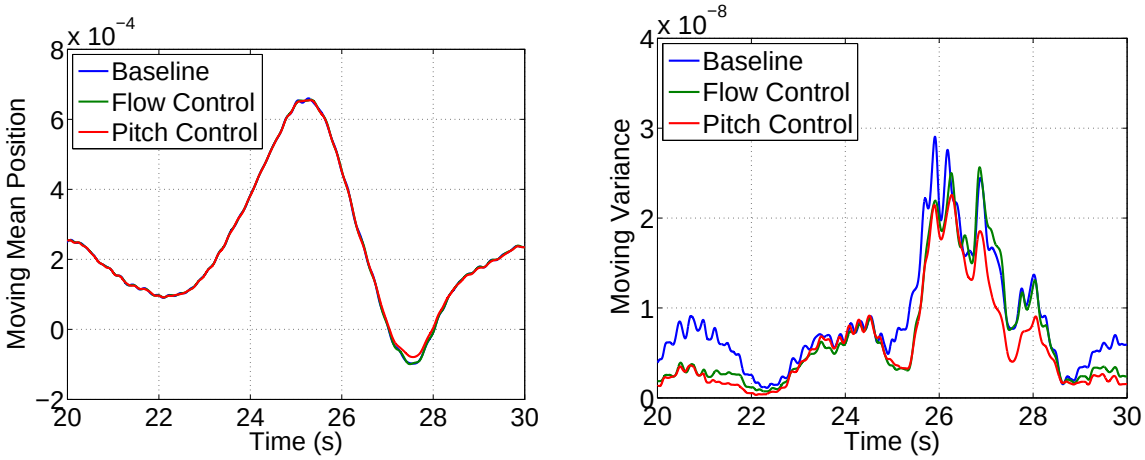


(a) Moving-average position

(b) Moving variance around moving-average position

Figure 4.12: Tower fore-aft movement mean position and variance

To quantify these results, moving-average tower-top position for $1s$ interval are presented in Figure 4.12(a) . The difference in the means of tower position all three cases – baseline, flow control and pitch control is not significant. However, this is not a deficiency of either of the control actuators, as they operate in actuation limits and frequencies to compensate for small-amplitude, medium-frequency $(2 - 10Hz)$ disturbances in the incoming wind as opposed to a large-amplitude, low-frequency $(\sim 0.1Hz)$ gust.

The moving-variances around the moving-average tower-top position is shown in 4.12(b). It is a measure of vibration of the tower top around the moving-average position. Prior to the gust, that is, between $20s$ and $21s$, the variance for both active control methods was significantly lower than the baseline case. During the gust, the variance for all three increases significantly, indicating higher vibration induced in the tower by the gust. Between $22s$ and $24s$, that is, the start of the gust, the variances for all three cases

are close to each other. After this initial phase of the gust, the variance for baseline is significantly higher than both the control cases. From after the peak to the end of the gust, that is, from $25s$ to $29s$, the variance for pitch control case remains lower than the baseline case. However, the variance for flow control case is similar to that of the baseline case. After the gust, that is, $29s$ onward, the variance for both control cases remains significantly lower than the baseline.

Thus, active control, as applied here, is not suited for mitigating ultimate loads. Hence, response to Extreme Operating Gust for 50 years ($EOG_{50\,years}$) was not simulated. However, the vibrations around the moving-mean tower position, which cause fatigue loads see a significant reduction in the control cases. The control cases, hence seem to be better suited for mitigation of fatigue loads, than for ultimate loads. A discussion on mitigation of fatigue loads for long term (20 years) operation of a turbine in turbulent winds is presented in the following section.

Before discussing long term simulations, it is worthwhile to look at the control efforts involved in dealing with the said gust, as, the maximum rate of change of error, $e$ seen by the controller is expected to be seen during the gust, and not in long term simulations for turbulent wind speeds. Figures 4.13(a) and 4.13(b) show the actuator outputs for the suction-based flow control actuator and the pitching-motors, respectively. The actuator outputs form the inputs to the plant in each of the control cases in simulation.

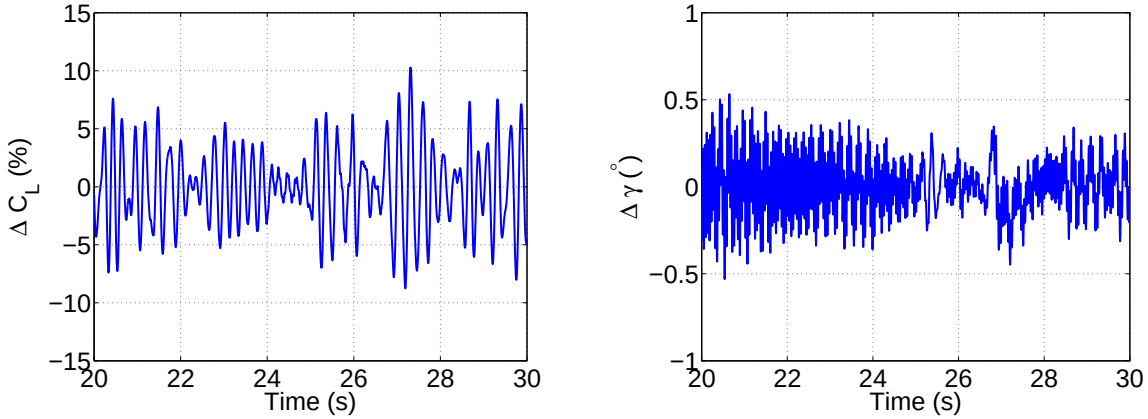


(a) Flow control actuator output

(b) Pitching-motor output

Figure 4.13: Actuator outputs to simulator

Physical limits on the magnitude corresponding to real life actuators, were imposed on the actuators models in simulations. These limits were ±10% change in $C_L$ and $C_D$,

and $\pm 1^{\circ}$ respectively for flow control and pitching actuators. As explained earlier in Section 4.3.3, the motor model was based on theoretical second-order dynamics for an electrical motor, and the dynamics of suction identified in Section 3.4 were incorporated into the model of the flow control actuator. These dynamics imposed the limits on the rate of change on the control effort demanded by the respective algorithms. The control effort demanded by the controller was given as input to the models of the actuators, which produced the respective outputs based on the incorporated models and the physical limits. Thus, these outputs, which act as inputs to the aero-elastic simulator for obtaining the desired results are meaningful, and close to realisable values in real life .

### 4.4.2 Long term response to turbulent winds

Table 4.4: Load mitigation calculations

| | |
|---|---|
| Turbine | SWRT (see Table 4.2) |
| Wind | |
| Generation | Turbsim [Jon09] |
| Bin mean speeds | $3m/s$, $5m/s$, ..., $19m/s$ |
| Class | IEC III A [Int08a] |
| Turbulence | 18% |
| Distribution | Weibull, $\alpha_w = 2$, $\beta_w = 7.5$ |
| Duration | 600s (each simulation) |
| Time step | 0.001s |
| Tower | |
| Steel | S355 |
| | Endurance Stress ($s_e$)= $250MPa$ |
| | $b$=-0.1 |
| Dimensions | $r_1$=$7cm$ |
| | $r_2$=$8cm$ |

In this section, long term effectiveness of load mitigation using active control is analysed by arriving at an estimate of 'Damage Equivalent' for the small wind turbine described in Section 4.3.2 over a 20 year usage.

**Methodology for arriving at damage equivalent**

To arrive at this estimate, first, wind speed distribution and its turbulence characteristics were chosen using Weibull distribution and IEC III A [Int08a] classification, respectively. (See Section 2.10). IEC III A specifies the mean wind speed as $7.5m/s$ (Weibull parameter $\beta_w$), with a turbulence of 18% and scaling factor (Weibull parameter $\alpha_w$) of 2. The resulting probability density function of wind speeds is shown in Figure 2.21(b). The meaningful wind speeds to analyse lie between $3m/s$ and $19m/s$ based on this distribution. Thus, turbulent wind profiles at mean speed $3m/s$, $5m/s$, ..., $19m/s$ and 18% turbulence were generated, which were given as inputs to the aero-elastic simulator for the three cases – baseline, flow control and pitch control. The time period for each of these simulations was $600s$, and time-step was $0.001s$.

The out-of-the-plane bending-moments (a standard output of the FAST simulator), $M_y$ at the tower base were recorded for each wind speed for all three cases. The resulting shear stresses on the structure was calculated as $M_y r_2/I_y$, where $I_y$ is the second moment of inertia, $\pi(r_2^4 - r_1^4)/4$, and $r_1$, $r_2$ the inner and outer radii of the tower, respectively. The resulting stress spectrum was reduced to cycle counts of reversal of stresses using ASTM's rain-flow count method for each wind speed (see Section 2.11). These cycle counts were divided into 13 bins based on the stress amplitude.

The cycle counts for each wind speed were combined together as a weighed average, with the weights calculated from Weibull probability distribution function for each of the wind speed to get an estimate of average distribution of expected stresses over $600s$. This was then multiplied by the time factor to extrapolate these estimates to use over 20 years.

Finally, the Basquin equation and Palmgren-Miner rule (see Section 2.11) were used to calculate the damage fractions for each of the 13 stress amplitude bins for operation over 20 years. The damage fractions were summed up to estimate the total damage equivalent for the three cases.

Following is a discussion of stress distribution at low, medium and high mean wind speeds, which details the stresses and cycles and their relevance to structural damage. This leads to the discussion on damage equivalents over 20 years operation.

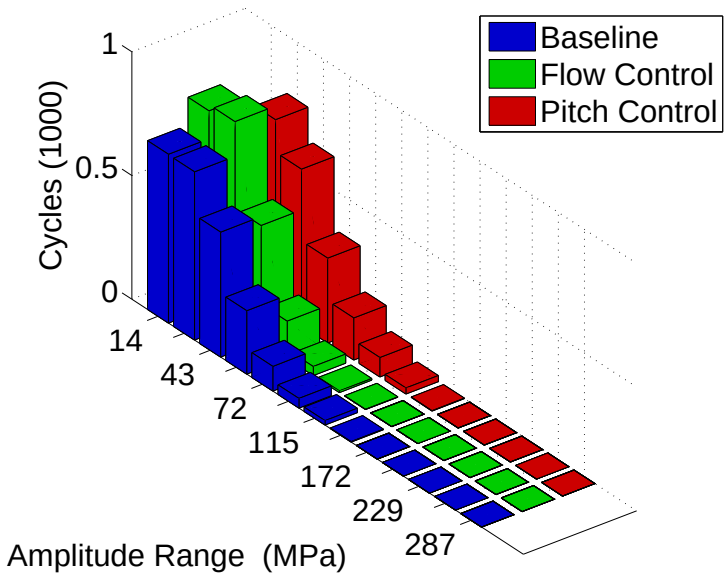


Figure 4.14: Stress cycles for wind speed $7m/s$

**Stress cycles at low, medium and high wind speeds**

**Low wind speed**

Figure 4.14 shows the estimated number of cycles for stress reversals in $600s$ at mean wind speed of $7m/s$. For the baseline case, the maximum number of cycles is seen in low stress-amplitude range. The number of cycles consistently decreased from $14MPa$ to $143MPa$. There were no cycles for stresses greater than $172MPa$. According to the fatigue theory, low-amplitude stress reversals do not damage the structure significantly. Theoretically, the structure will withstand an infinite number of cycles for such stresses.

For the flow control case, there was an increase in low-amplitude cycles over the baseline case. For the lowest bin, $14MPa - 29MPa$, the number of cycles increased from 682 to 795. However, from the third bin ($43MPa - 57MPa$) onward, the number of cycles reduced over the baseline case for all bins. For instance, in the $115MPa - 143MPa$ bin, the number of cycles reduced from 18 to 1, which is a significant reduction. Overall, a general trend of the graph shifting towards the left was observed.

For the pitch control case, the number of cycles increased for all bins. However, since the stresses for this wind speed do not cause structural damage, this is not detrimental to the use of pitch control, that is, if pitch control is able to reduce the number high amplitude cycles for higher wind speeds.

**Medium wind speed**

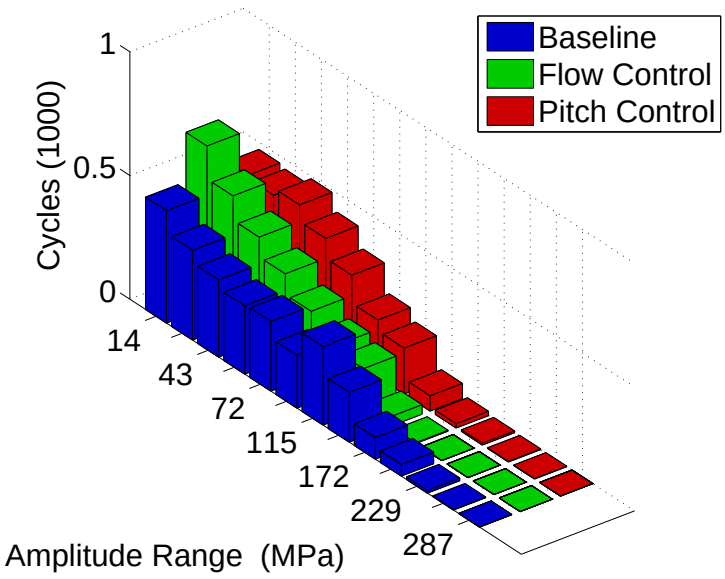


Figure 4.15: Stress cycles for wind speed $13m/s$

Figure 4.15 shows the estimated number of cycles for stress reversals in $600s$ at mean wind speed of $13m/s$. For all three cases, a higher number of large-amplitude cycles were observed as compared to those at wind speed $7m/s$. This is to be expected, as higher wind speed contains more energy, and is more turbulent than lower wind speed. For the baseline case, there is a general decrease in the number of cycles for higher amplitudes. However, the number of cycles in the bins $115MPa - 143MPa$ and $143MPa - 172MPa$ is much higher than that expected by this trend. This may be due to excitation of a natural frequency of the tower at higher wind speeds.

In the baseline case, all stress amplitudes were present – low ($< 115MPa$), medium ($115MPa - 201MPa$) and high ($> 201MPa$). Out of these, low amplitudes do not cause structural damage. Medium amplitude stress cycles too, do not cause significant structural damage. The high amplitude stress cycles contribute significantly to structural damage. Flow control has the maximum impact in this range. There were no stresses in the large amplitude range ($> 201MPa$), as compared to a total of 59.5 cycles in these four bins for the baseline case. Flow control is also effective in the medium amplitude range.The number of cycles for $143MPa - 172MPa$ bin were reduced from 201.5 in the baseline case to 38.5 with flow control.

Pitch control, was similarly effective in reducing the number of cycles in the high amplitude range. The total number of cycles in the 4 bins above $201MPa$ was 10.5, as

compared to 59.5 for the baseline case. The number of cycles also reduced for medium amplitude stress reversals. For instance, the number of cycles for $143MPa - 172MPa$ bin were reduced from 201.5 in the baseline case to 61.5 with pitch control.

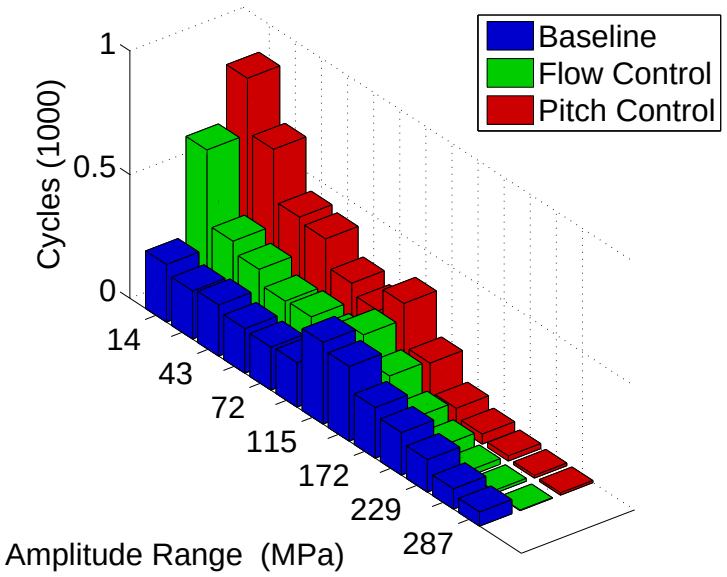


Figure 4.16: Stress cycles for wind speed $17m/s$

**High wind speed**

Figure 4.16 shows the estimated number of cycles for stress reversals in $600s$ at mean wind speed of $17m/s$. The number of large amplitude cycles increased further over the medium wind speed for all three cases, as was expected. The local peak in the bin $115MPa - 143MPa$ was seen in all three cases, indicating this to be a part of the structure response.

The baseline case had 172, 131.5, 82 and 57 cycles in the four bins above $201MPa$. These numbers are significantly higher than lower wind speeds. Such large number of cycles in high amplitude bins would cause serious structural damage over years. Flow control reduced these numbers to 55.5, 22.5, 11.5 and 2 respectively. The corresponding figures for pitch control were 40, 20.5, 10.5 and 8.5 respectively. Thus, both, flow control and pitch control were able to mitigate high-amplitude stresses. This is a significant achievement as the stresses in this range is responsible for maximum structural damage.

The number of cycles for medium amplitude stresses also decreased for both control cases. However, the number of low amplitude stresses increased significantly for both control cases. Thus, both control actuators were able to shift the graph towards the left,

that is, reduce the amplitude of the fore-aft movement of the tower.

**Compiled distribution of loads for weighed mean of wind speeds**

Appendix B shows the stress distribution for all simulated mean wind speeds, that is, $3m/s$, $5m/s$, ..., $19m/s$. The trends explained earlier can be visually seen in these graphs:

- With increase in the wind speed, high amplitude stress cycles increased for all three cases.
- Local peak was observed in the bin $115MPa - 143MPa$, which may be due to structural response of the tower.
- Both control cases were able to "push" the bars towards the left, that is, reduce high amplitude stresses, which are the root cause of fatigue damage.

A weighed mean of the number of cycles for each stress bin was calculated for these simulated wind speeds. The weights were arrived at using the Weibull distribution. Figure 4.17 shows the estimates of number of cycles for stress bins. The corresponding numbers are also given in Table 4.5.

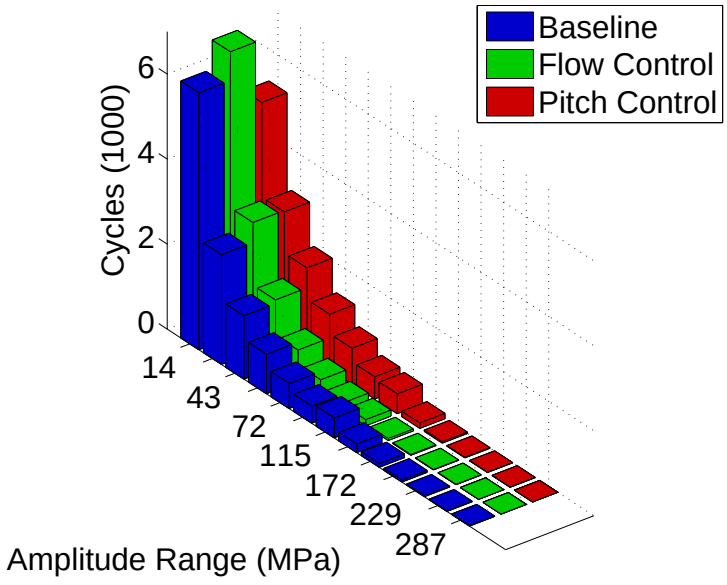


Figure 4.17: Predicted Hourly Stresses

**Damage equivalents**

Basquin equation and Palmgren-Miner rule was used to calculate the damage fractions for each cycle amplitude bin for operation over 20 years. The damage fractions were

Table 4.5: Predicted Hourly Stresses

| **Stress** ($MPa$) | **Baseline** | **Flow Control** | **Pitch Control** |
|---|---|---|---|
| $< 14$ | 6044 | 6726 | 5249 |
| 14 - 29 | 2582 | 3056 | 3019 |
| 29 - 43 | 1490 | 1579 | 2047 |
| 43 - 57 | 931 | 746 | 1302 |
| 57 - 72 | 589 | 391 | 849 |
| 72 - 86 | 405 | 195 | 524 |
| 86 - 115 | 471 | 142 | 467 |
| 115 - 143 | 199 | 44 | 127 |
| 143 - 172 | 85 | 15 | 30 |
| 172 - 201 | 45 | 5.9 | 12.1 |
| 201 - 229 | 18.6 | 2.6 | 5.8 |
| 229 - 258 | 10.2 | 1.0 | 2.1 |
| $> 258$ | 6.4 | 0.3 | 1.6 |

summed up to estimate the total damage equivalent for the three cases (shown in Figure 4.18). Theoretically, damage is said to have occurred for damage equivalent between 1.7 and 2.2.

The damage equivalent for the baseline case is 9.56. The tower would have suffered extensive damage much before 20 years. For pitch control, the damage equivalent was estimated to be 2.5. Thus, there is high propensity of the tower to have suffered permanent damage during 20 years operation. The damage equivalent for flow control case was 0.84. A turbine employing such a technique would have very low propensity of suffering structural damage in 20 years. Thus, flow control can help increase the lifetime of a small wind turbine. Conversely, lesser material can be used in the tower for a similar expected lifetime.

It is worth noting that both flow control and pitch control achieve fatigue mitigation, which is much superior than the baseline case. The actual benefits obtained using the two actuation techniques would depend upon a multitude of factors, including – power consumed, mode of application, control algorithm amongst others. While it may not be suitable to comment on superiority of one method over the other, this thesis established that both methods have similar order-of-magnitude benefits. While deciding applications, the mode of application of flow control and pitch control may be stand alone, or in tandem

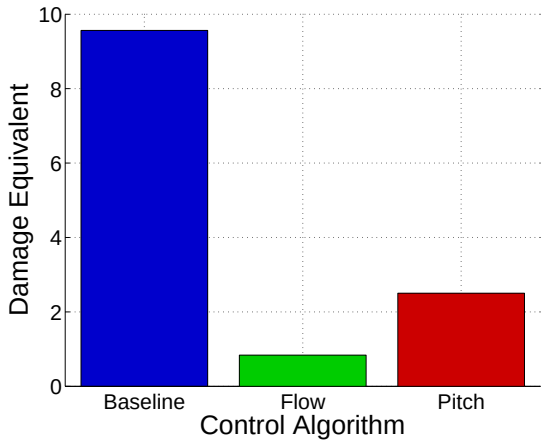


Figure 4.18: Predicted Damage Equivalent for 20 Years Operation

with each other. Such flow control may also be applied to large wind turbines close to the root of the blade, as this area operates in low $Re$ - typically, the range used in this thesis.

## 4.5 Summary

Two small wind turbine scenarios incorporating suction-based flow control were simulated, first for power increase and the second for load mitigation.

1. The aerodynamic power output of a small wind turbine increased on applying surface suction based flow control. Specifically, the power output increased from $764W$ to $1511W$ with an input of $106W$ of suction power.

2. The fatigue damage caused to turbine tower reduced significantly with the use of surface suction based active flow control. The damage equivalents for baseline (no control) case, pitch control case and flow control case were 9.56, 2.50 and 0.84 respectively.

# Chapter 5

# Conclusions and future work

## 5.1 Summary

In this thesis, active flow control via surface suction was proposed as a means to increase the power output and decrease fatigue damage for small wind turbines.

Boundary layer separation at low $Re$ was identified as a cause of the low aerodynamic efficiency of small wind turbines. Surface suction-based flow control was chosen as a means to control boundary layer separation over aerofoils. Consequently, the coefficients of lift and drag, $C_L$ and $C_D$ could be controlled by varying suction, which was quantified using the coefficient of momentum of suction ($C_\mu$). Wind tunnel tests were conducted in the $Re$ range $10^4$ - $10^5$, on two aerofoil profiles, NACA0012 and S814, to establish the steady-state relationships between $C_L$ and $C_D$, and $C_\mu$.

A wind turbine simulator employing steady Blade Element Momentum (BEM) theory and the relations between $C_L$, $C_D$ and $C_\mu$ from the wind tunnel experiments was used to predict the output of a turbine with blades employing suction-based flow-control. It was seen that such small wind turbines can realise Coefficient of Power ($C_P$) close to those typically seen in large wind turbines (Figure 5.1(a)).

Further, system-identification was used to find the dynamic model for surface suction-based flow-control. This model captured the limits of surface suction, that is, how fast flow control is able to change $C_L$ and $C_D$, and what is the nature of the transient response when suction ($C_\mu$) is applied. It was found that an over-damped second-order transfer function provided a good fit to the experimental data.

This dynamic model was incorporated into FAST as an add-on. A simple PD

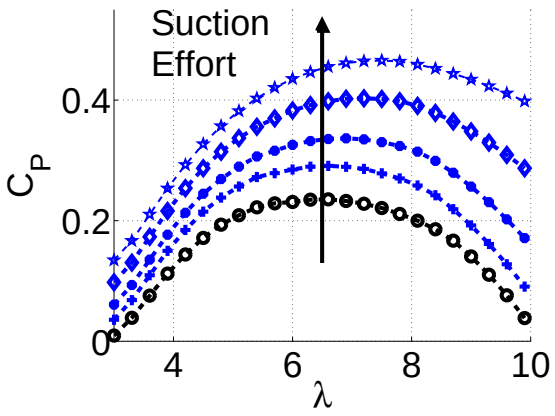


(a) $C_p$ versus suction effort

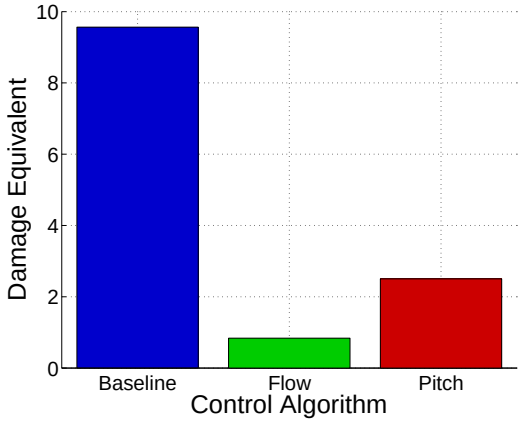


(b) Predicted damage equivalent for 20 years' operation

Figure 5.1: Benefits of surface suction for small wind turbines

(Proportional-Derivative) controller was designed to vary $C_\mu$ such that the fore-aft movement was reduced. Correspondingly, the fatigue loads on the tower reduced. This led to reduction of expected fatigue damage over 20 years' operation of the modelled turbine. The extent of load mitigation was found to be of the same order of magnitude as that using the conventional technique of pitch control (Figure 5.1(b)).

These results establish substantial promise for the use of surface suction for improving aerodynamic efficiency and improving fatigue life of structure of small wind turbines.

## 5.2 Conclusions

Surface suction-based flow control experiments over NACA0012 and S814 aerofoils at low $Re$ indicate that:

- $C_L$ and $C_D$ can be changed by 20% to 40% for varying angles of attack, by controlling the suction input, which is characterised by coefficient of momentum, $C_\mu$.
- The time-constant identified for the response of change in $C_L$ ($\Delta C_L$) and $C_D$ ($\Delta C_D$) on a step change in $C_\mu$ is close to $0.02\,s$.

Though these experiments were conducted for two aerofoil profiles, the change in $C_L$ and $C_D$, and the time constant are expected to be similar for majority of other aerofoil profiles employing surface suction-based flow-control at similar $Re$ numbers and $C_\mu$. This

is because, the underlying phenomena for the flow-control is mitigation of boundary layer separation using $C_\mu$, which affects most of the aerofoil profiles at low $Re$.

Small wind turbines employing surface suction-based flow-control over their blades are expected to produce more power, and last longer. More specifically:

- $C_P$ can be increased by up to 40%, by applying steady $C_\mu$ over the blades.
- Fatigue can be mitigated, and thus, $\sim$ 80% reduction in damage equivalent to structure can be achieved by applying close-loop controlled suction over the blades.

Since boundary layer separation control is expected to work on a vast variety of aerofoil profiles, and specifically on those used in small wind turbines, such technique should be applicable to majority of the existing and in-development small wind turbines. Further, since the root of the blades of large wind turbines operates in the $Re$ range explored in this thesis, fatigue mitigation via suction-based flow control can also be extended to these turbines.

## 5.3 Future Work

This thesis investigates the improvement in aerodynamic characteristics of aerofoils at low $Re$ by applying surface suction-based flow-control and the subsequent benefit of extending such a technique to small wind turbines. This analysis is a key initial step before further engineering challenges in implementation of such active flow-control in a wind turbine are addressed. The most important challenges to be solved for eventual employment of such a technique in small wind turbines are the development of:

- An efficient and robust mechanism for use in wind turbine blades. The mechanism would need to provide for suction in rotating blades and minimise the losses.
- Solutions to tackle dirt and ice accumulation on the suction slit.
- A robust sensor for measuring the feedback variable, that is, the tower top fore-aft movement.
- The mechanism will have to be easily maintainable with low service costs.

The blade area close to the root in large wind turbines operates in similar $Re$ regimes as small wind turbines. Load mitigation, as described in this thesis can be extended to large turbines by applying flow control to the blade area close to the root.

It was observed that suction based flow control helps in reducing turbulence in the wake along with increasing the efficiency of the aerofoils. Turbulence in the wake puts restrictions on how closely wind turbines can be placed in a wind farm. Reduced turbulence in the wake may lead to more compact wind farms.

# Appendix A

# Cost of Energy

Table A.1: Cost of energy estimates

| | **Large wind turbine** | **Small wind turbine** |
|---|---|---|
| Rated power | $1.5MW$ | $1kW$ |
| Cost per MW | INR $6 - 6.5Cr/MW$ | INR $7.5 - 8Cr/MW$ |
| Cost of turbine | INR $9 - 9.75Cr$ | INR $7.5 - 8Lk$ |
| Annual Interest Rate | 13%-16% | 13%-16% |
| Years of repayment | 20 | 20 |
| Monthly maintenance | 2% - 3% of cost | 2%-3% of cost |
| Capacity factor | 0.25-0.33 | 0.1-0.2 |
| Cost of energy | Rs 3.38 - $5.93/kWh$ | Rs. 7.73 - 19.93 $/kWh$ |

# Appendix B

# Stress cycles

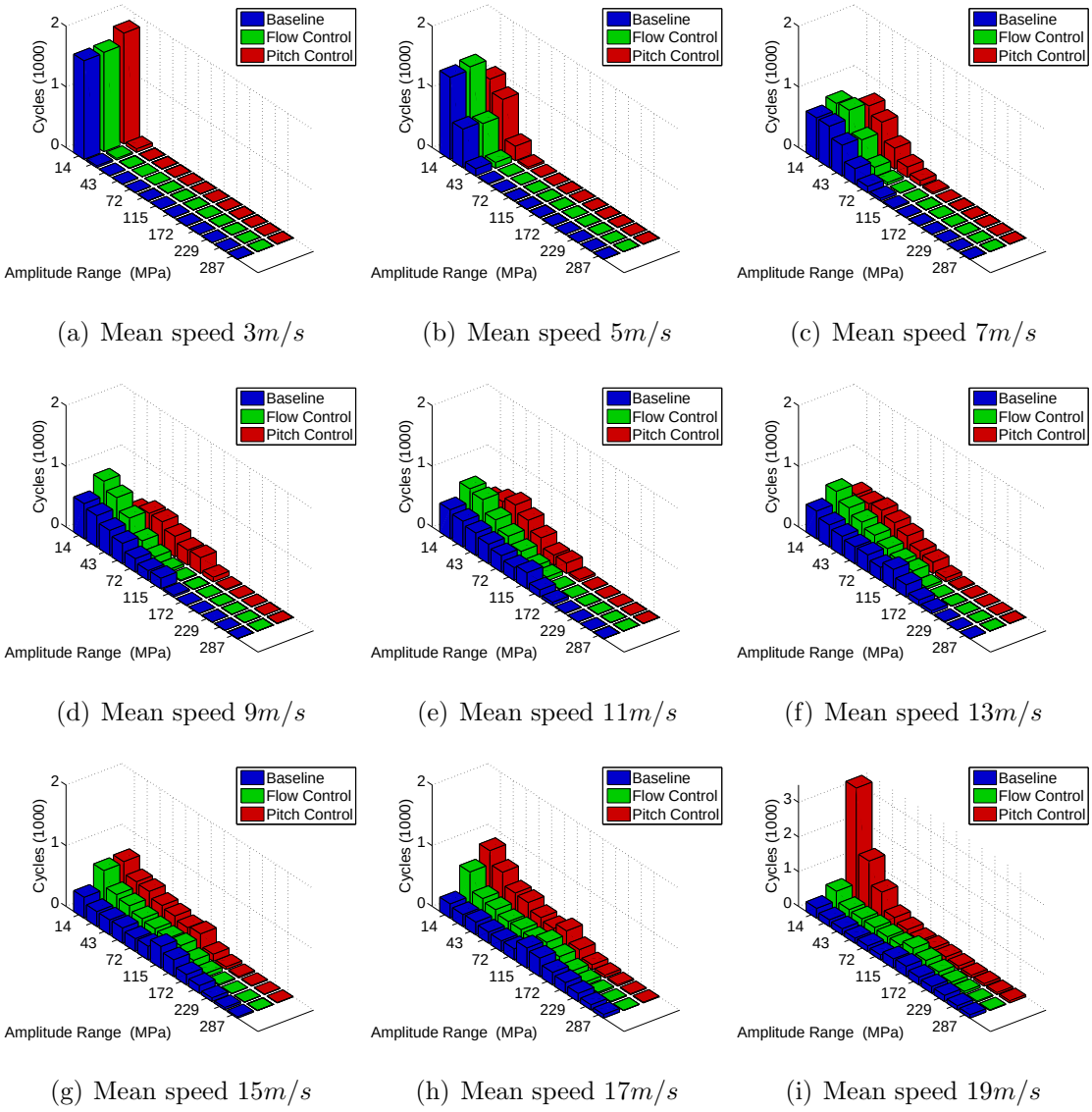


(a) Mean speed $3m/s$ (b) Mean speed $5m/s$ (c) Mean speed $7m/s$

(d) Mean speed $9m/s$ (e) Mean speed $11m/s$ (f) Mean speed $13m/s$

(g) Mean speed $15m/s$ (h) Mean speed $17m/s$ (i) Mean speed $19m/s$

Figure B.1: Rainflow count of bending moments for various wind speeds

# Bibliography


[Aer06] Airplane aerodynamics. http://www.free-online-private-pilot-ground-school.com/aerodynamics.html, 2006. Accessed : 2009-11-25.

[Ari04] Secil Ariduru. *Fatigue life calculation by rainflow cycle counting method*. PhD thesis, Middle East Technical University, 2004.

[AYTS12] MA Abdullah, AHM Yatim, CW Tan, and R Saidur. A review of maximum power point tracking algorithms for wind energy systems. *Renewable and Sustainable Energy Reviews*, 16(5):3220–3227, 2012.

[Bar96] Yaman Barlas. Formal aspects of model validity and validation in system dynamics. *System dynamics review*, 12(3):183–210, 1996.

[BDBM06] Fernando D Bianchi, Hernan De Battista, and Ricardo J Mantz. *Wind turbine control systems: principles, modelling and gain scheduling design*. Springer, 2006.

[Bet66] Albert Betz. *Introduction to the theory of flow machines*. Pergamon, 1966.

[Bos94] E A Bossanyi. Electrical aspects of variable speed operation of horizontal axis wind turbine generators. Number W/33/00221/REP. ETSU, Harwell, 1994.

[Bos00] EA Bossanyi. The design of closed loop controllers for wind turbines. *Wind energy*, 3(3):149–163, 2000.

[Bos05] EA Bossanyi. Further load reductions with individual pitch control. *Wind energy*, 8(4):481–485, 2005.

[Bra99] Albert L. Braslow. *A History of Suction-Type Laminar-Flow Control with Empahsis on Flight Research*. NASA History Division, 1999.

[BRP99] J.B. Barlow, W.H. Rae, and A. Pope. *Low-speed wind tunnel testing*. Aerospace engineering/mechanical engineering. Wiley, 1999.

[BSJB01] T. Burton, D. Sharpe, N. Jenkins, and E. Bossanyi. *Wind Energy Handbook*. John Wiley & Sons, 2001.

[Chu10] Kung-Ming Chung. Effect of normal blowing on compressible convex-corner flows. *Journal of Aircraft*, 47(4):1189–1196, 2010.

[CJST04] S Collisa, R D Joslinb, A Seifert, and V Theofilis. Issues in active flow control: theory, control, simulation, and experiment. *Progress in Aerospace Sciences*, 40:237–289, 2004.

[CM05] D Corbus and M Meadors. Small wind research technical report. *Golden, CO: National Renewable Energy Laboratory*, 2005.

[Col93] Jack A Collins. *Failure of materials in mechanical design: analysis, prediction, prevention*. John Wiley & Sons, 1993.

[DCFC09] Enrique Del Castillo and Alfonso Fernández-Canteli. *A unified statistical methodology for modeling fatigue damage*. Springer, 2009.

[Dha06] Sandeep Dhar. *Development and Validation of Small-scale Model to Predict Large Wind Turbine Behavior*. PhD thesis, Indian Institute of Technology, Bombay, 2006.

[DPW+10] Fiona Dunne, Lucy Pao, Alan D Wright, Bonnie Jonkman, and Neil Kelley. Combining standard feedback controllers with feedforward blade pitch control for load mitigation in wind turbines. In *Proc. 48th AIAA Aerospace Sciences Meeting, Orlando, FL, AIAA-2010-250*, 2010.

[DPW+11] Fiona Dunne, Lucy Y Pao, Alan D Wright, Bonnie Jonkman, and Neil Kelley. Adding feedforward blade pitch control to standard feedback controllers for load mitigation in wind turbines. *Mechatronics*, 21(4):682–690, 2011.

[(DU05] Wind Energy Group (DUT). Windsim, March 2005. http://tudelft.nl/en/research/knowledge-centres/duwind/windsim/.

[DV06] Rgis Duvigneau and Michel Visonneau. Simulation and optimization of stall control for an airfoil with a synthetic jet. *Aerospace Science and Technology*, 10(4):279 – 287, 2006.

[Eka04] John A. Ekaterinaris. Prediction of active flow control performance on airfoils and wings. *Aerospace Science and Technology*, 8:401–410, 2004.

[Epp99] Richard Eppler. Airfoils with boundary layer suction, design and off-design cases. *Aerospace Science and Technology*, 3(7):403 – 415, 1999.

[FK88] Milton E Franke and Lawrence Kudelka. System for boundary layer control through pulsed heating of a strip heater, November 22 1988. US Patent 4,786,020.

[FMG+08] Daniel Favier, Christian Maresca, Wolfgang Geissler, Marcellin Nsi Mba, and Patrick Sainton. Boundary-layer control by hydrophilic surfaces. *Journal of Aircraft*, 45(4):1334–1343, 2008.

[FSSQ13] Lauha Fried, Steve Sawyer, Shruti Shukla, and Liming Qiao. Global wind report: Annual market update 2012. *Report, Global Wind Energy Council (GWEC), Brussels, Belgium*, 2013.

[Gaz00] Robert F Gazdinzky. Vehicular boundary layer control system and method. Patent, 2000.

[GBHMV14] David Greenblatt, Amos Ben-Harav, and Hanns Mueller-Vahl. Dynamic stall control on a vertical-axis wind turbine using plasma actuators. *AIAA Journal*, pages 1–7, 2014.

[GC08] M Geyler and P Caselitz. Robust multivariable pitch control design for load reduction on large wind turbines. *Journal of solar energy engineering*, 130(3):031014, 2008.

[GeH07] Mohamed Gad-el Hak. *Flow control: passive, active, and reactive flow management*. Cambridge University Press, 2007.

[GO73] Nigel Gregory and CL O'reilly. *Low-speed aerodynamic characteristics of NACA 0012 aerofoil section, including the effects of upper-surface roughness simulating hoar frost*. HM Stationery Office, 1973.

[GPCSH06] David Greenblatt, Keith B. Paschal, Yao Chung-Sheng, and Jerome Harris. Experimental investigation of separation control part 2: Zero mass-flux oscillatory blowing. *AIAA Journal*, 44(12):2831–2845, 2006.

[GPY+06] David Greenblatt, Keith B. Paschal, Chung Sheng Yao, Jerome Harris, Norman W. Schaeffler, and Anthony E. Washburn. Experimental investigation of separation control part 1: Baseline and steady suction. *AIAA Journal*, 44(12):2820–2830, 2006.

[Gre10] David Greenblatt. Active control of leading-edge dynamic stall. *International Journal of Flow Control*, 2(1):21–38, 2010.

[GSBH12] David Greenblatt, Magen Schulman, and Amos Ben-Harav. Vertical axis wind turbine performance enhancement using plasma actuators. *Renewable Energy*, 37(1):345–354, 2012.

[HHLH04] L Huang, P G Huang, R P LeBeau, and T Hauser. Numerical study of blowing and suction control mechanism on naca0012 airfoil. *Journal of Aircraft*, 41(1), 2004.

[Int08a] International Electrotechnical Commission, International Electrotechnical Commission, 3, rue de Varemb, PO Box 131, CH-1211 Geneva 20, Switzerland Telephone: +41 22 919 02 11 Telefax: +41 22 919 03 00 E-mail: inmail@iec.ch Web: www.iec.ch. *International Standard IEC 61400-1*, 3 edition, 2005-08.

[Int08b] International Electrotechnical Commission, International Electrotechnical Commission, 3, rue de Varemb, PO Box 131, CH-1211 Geneva 20, Switzerland Telephone: +41 22 919 02 11 Telefax: +41 22 919 03 00 E-mail: inmail@iec.ch Web: www.iec.ch. *International Standard IEC 61400-2*, 3 edition, 2005-08.

[JAS07] Sharad K Jain, Pushpendra K Agarwal, and Vijay P Singh. *Hydrology and water resources of India-Volume 57 of Water science and technology library-Tributaries of Yamuna river*. Springer, 350pp, 2007.

[JBJ05] Jason M Jonkman and Marshall L Buhl Jr. Fast users guide. *Golden, CO: National Renewable Energy Laboratory*, 2005.

[Jon09] Bonnie J Jonkman. *TurbSim user's guide: Version 1.50*. National Renewable Energy Laboratory Colorado, 2009.

[JVDB08] Scott J Johnson, CP Van Dam, and Dale E Berg. Active load control techniques for wind turbines. *SAND2008-4809, Sandia National Laboratories, Albuquerque, NM*, 2008.

[KB04] Valdis Kibens and William W Bower. An overview of active flow control applications at the boeing company. *AIAA paper*, 2624:2004, 2004.

[KCC11] Dong-Ha Kim, Jo-Won Chang, and Joon Chung. Low-reynolds-number effect on aerodynamic characteristics of a naca 0012 airfoil. *Journal of Aircraft*, 48(4):1212–1215, 2011.

[Lac14] Gustav Victor Lachmann. *Boundary layer and flow control: its principles and application*. Elsevier, 2014.

[Lai97] EV Laitone. Wind tunnel tests of wings at reynolds numbers below 70 000. *Experiments in Fluids*, 23(5):405–409, 1997.

[Lal99] Christian Lalanne. *Mechanical Vibration & Shock, Fatigue Damage*, volume IV. Taylor and Francis Books, Inc., 1999.

[LDCH10] P Q Liu, H S Duan, J Z Chen, and Y W He. Numerical study of suction-blowing flow control technology for an airfoil. *Journal of Aircraft*, 47, 2010.

[Lju98] L. Ljung. *System Identification: Theory for the User*. Pearson Education, 1998.

[Loc24] C. N. H. Lock. Experiments to verify the independence of the elements of an airscrew blade. *ARCR R and M*, (953), 1924.

[LPW09] Jason H Laks, Lucy Y Pao, and Alan D Wright. Control of wind turbines: Past, present, and future. In *American Control Conference, 2009. ACC'09.*, pages 2096–2103. IEEE, 2009.

[Mae86] Lucio Maestrello. Active control of boundary layer transition and turbulence. Patent, 1986.

[MCSP98] Philippe Mouyon, Grégoire Casalis, Alain Séraudie, and Sylvain Prudhomme. Feedback control of the laminar-turbulent transition onset in a boundary layer by suction. *Experimental thermal and fluid science*, 16(1):22–31, 1998.

[MG11] Shravana Musunuri and HL Ginn. Comprehensive review of wind energy maximum power extraction algorithms. In *Power and Energy Society General Meeting, 2011 IEEE*, pages 1–8. IEEE, 2011.

[MH80] J H McMasters and M L Henderson. Low speed single element airfoil synthesis. *Technical Soaring*, 2:1–21, 1980.

[MO87] TJ Mueller and MM O'meara. Laminar separation bubble characteristics on an airfoil at low reynolds numbers. *AIAA journal*, 25(8), 1987.

[Mue00] Thomas J Mueller. Aerodynamic measurements at low reynolds numbers for fixed wing micro-air vehicles. Technical report, DTIC Document, 2000.

[Mue02] Thomas J. Mueller. *Fixed and flapping wing aerodynamics for micro air vehicle applications*. AIAA, 2002.

[NB94] Daniel M Nosenchuck and Garry L Brown. Electromagnetic device and method for boundary layer control, June 14 1994. US Patent 5,320,309.

[NY12] Holly C. Neatby and Serhiy Yarusevych. Towards reliable experimental drag measurements on an airfoil at low reynolds numbers. In *Proceedings of the 42nd Fluid Dynamics Conference and Exhibit*, Fluid Dynamics Conference and Exhibit. AIAA, June 2012.

[OY70] Katsuhiko Ogata and Yanjuan Yang. Modern control engineering. 1970.

[PAWLC11] Fernando Port-Agel, Yu-Ting Wu, Hao Lu, and Robert J. Conzemius. Large-eddy simulation of atmospheric boundary layer flow through wind turbines and wind farms. *Journal of Wind Engineering and Industrial Aerodynamics*, 99(4):154 – 168, 2011.

[PEB+00] Kjartan Pedersen, J Emblemsvag, Reid Bailey, Janet K Allen, and F Mistree. Validating design methods and research: the validation square. In *ASME Design Theory and Methodology Conference*, 2000.

[PK08] I. Cohen P. Kundu. *Fluid Mechanics*, chapter Dynamic Similarity, pages 279–294. Academic Press, 2008.

[PN98] Pradip G Parikh and Frank D Neumann. Aircraft boundary layer control system with discharge transpiration panel, June 30 1998. US Patent 5,772,156.

[PP02] Athanasios Papoulis and S Unnikrishna Pillai. *Probability, random variables, and stochastic processes*. Tata McGraw-Hill Education, 2002.

[PPM+10] P Pernod, V Preobrazhensky, A Merlen, O Ducloux, A Talbi, L Gimeno, R Viard, and N Tiercelin. Mems magneto-mechanical microvalves (mmms) for aerodynamic active flow control. *Journal of Magnetism and Magnetic Materials*, 322(9):1642–1646, 2010.

[RM08] Reni Raju and Rajat Mittal. Dynamics of airfoil separation control using zero-net mass-flux forcing. *AIAA JOURNAL*, 46(12):3103–3115, December 2008.

[Sau13] Walter J Saucier. *Principles of meteorological analysis*. Courier Dover Publications, 2013.

[SB06] Ali Kerem Saysel and Yaman Barlas. Model simplification and validation with indirect structure validity tests. *System Dynamics Review*, 22(3):241–262, 2006.

[Sch00] Hermann Schlichting. *Boundary-Layer Theory*, chapter Boundary-Layer Control (Suction/Blowing), pages 291–321. Springer, 2000.

[Sch09] J. U. Schlter. Lift enhancement at low reynolds numbers using pop-up feathers. In *39th AIAA Fluid Dynamics Conference*, 2009.

[SD05] Shashikanth Suryanarayanan and Amit Dixit. Control of large wind turbines: Review and suggested approach to multivariable design. In *Proc. of the American Control Conference*, pages 686–690, 2005.

[SG11] Binyamin Sasson and David Greenblatt. Effect of leading-edge slot blowing on a vertical axis wind turbine. *AIAA journal*, 49(9):1932–1942, 2011.

[SJL+08] Hua Shan, Li Jiang, Chaoqun Liu, Michael Love, and Brant Maines. Numerical study of passive and active flow separation control over a naca0012 airfoil. *Computers and Fluids*, 37:975–992, 2008.

[SNAG05] M H Shojaefard, A R Noorpoor, A Avanesians, and M Ghaffarpour. Numerical investigation of flow control by suction and injection on a subsonic airfoil. *American Journal of Applied Sciences*, 2(10):1474–1480, 2005.

[SP81] R. E. Sheldahl and P.C.Klimas. Aerodynamic characteristics of seven airfoil sections through 180 degrees angle of attack for use in aerodynamic analysis of vertical axis wind turbines. Technical report, Sandia National Laboratories, 1981.

[SSK+95] Anatoly I Savitsky, Lev N Schukin, Viktor G Karelin, Aleksandr M Mass, Rostislav M Pushkin, Anatoly P Shibanov, Ilya L Schukin, and Sergei V Fischenko. Method for control of the boundary layer on the aerodynamic surface of an aircraft, and the aircraft provided with the boundary layer control system, May 23 1995. US Patent 5,417,391.

[SSM01] K.E. Swalwell, J. Sheridan, and W.H. Melbourne. The effect of turbulence intensity on stall of the naca 0021 aerofoil. In *Procreedings of the 14th Australasian Fluid Mechanics Conference*, pages 941–944, 2001.

[ST95] D.M. Somers and J.L. Tangler. Wind-tunnel test of the s814 thick root airfoil. Technical report, National Renewable Energy Lab., Golden, CO (United States), 1995.

[Sta74] P.K. Stansby. The effects of end plates on the base pressure coefficient of a circular cylinder. *Aeronautical Journal*, 78:36–37, 1974.

[Sta01] E Stanewsky. Adaptive wing and flow control technology. *Progress in Aerospace Sciences*, 37(7):583–667, 2001.

[Sta05] ASTM Standard. E1049. standard practices for cycle counting in fatigue analysis, 2005.

[SY11] Arvin Shmilovich and Yoram Yadlin. Flow control techniques for transport aircraft. *AIAA journal*, 49(3):489–502, 2011.

[Szü80] E Szücs. Fundamental studies in engineering ii, similitude and modeling, 1980.

[TRCW10] Kunihiko Taira, Clarence W Rowley, Tim Colonius, and David R Williams. Lift enhancement for low-aspect-ratio wings with periodic excitation. *AIAA journal*, 48(8):1785–1790, 2010.

[TS+04] A Tuck, Julio Soria, et al. Active flow control over a naca 0015 airfoil using a znmf jet. In *15th Australasian fluid mechanics conference*, pages 13–17, 2004.

[Tur13] Turbulent Flow Instrumentation. *Dynamic Pressure Measurement System*, 2013.

[Wey01] Erik Weyer. System identification of an open water channel. *Control engineering practice*, 9(12):1289–1299, 2001.

[WF08] AD Wright and LJ Fingersh. Advanced control design for wind turbines, 2008.

[WGA02] Anthony E Washburn, S Althoff Gorton, and Scott G Anders. Snapshot of active flow control research at nasa langley. *AIAA paper*, 3155(1), 2002.

[Woo11] D. Wood. *Small Wind Turbines: Analysis, Design, and Application*. Green energy and technology. Springer, 2011.

[WPO95] Paul H. Wirsching, Thomas L. Paez, and Keith Ortiz. *Random Vibrations, Theory and Practice*. Wiley-Interscience, 1995.

[WTC+09] David R Williams, Gilead Tadmor, Tim Colonius, Wesley Kerstens, Vien Quach, and Seth Buntain. Lift response of a stalled wing to pulsatile disturbances. *AIAA journal*, 47(12):3031–3037, 2009.

[Wue61] W Wuest. Survey of calculation methods of laminar boundary layers with suction in incompressible flow. *Boundary layer and flow control*, 2:771–800, 1961.

[WW04] A.K. Wright and D.H. Wood. The starting and low wind speed behavior of a small horizontal axis wind turbine. *Journal of Wind Engineering and Industrial Aerodynamics*, 92:1265–1279, 2004.

[YB12] S. Yarusevych and M.S.H. Boutilier. Effects of end plates and blockage on low-reynolds-number flows over airfoils. *AIAA Journal*, 50(7):1547–1559, 2012.

[ZAY+11] Y. Zhou, Md. Mahbub Alam, H.X. Yang, H. Guo, and D.H. Wood. Fluid forces on a very low reynolds number airfoil and their prediction. *International Journal of Heat and Fluid Flow*, 32:329–339, 2011.

[ZZ10] Shanying Zhang and Shan Zhong. Experimental investigation of flow separation control using an array of synthetic jets. *AIAA journal*, 48(3):611–623, 2010.

# Appendix C

# Publications

- J.S. Chawla, S. Suryanarayanan, B. Puranik, J. Sheridan, B.G. Falzon, "Efficiency improvement study for small wind turbines through surface suction based flow control" *Sustainable Energy Technologies and Assessments, 2014.*
- J.S. Chawla, S. Suryanarayanan, J. Sheridan, B.G. Falzon, "Identification of dynamics of surface suction over an airfoil at low Reynolds numbers" *ASME 2013 International Mechanical Engineering Congress & Exposition, Nov 2013*